The Pennsylvania State University

The Graduate School

College of Engineering

MICROMECHANICAL ANALYSIS OF TRANSVERSE YOUNG'S MODULUS OF GLASS/CARBON HYBRID FIBER COMPOSITES

A Thesis in

Engineering Science and Mechanics

by

Ganesh Venkatesan

Submitted in Partial Fulfillment
of the Requirements
for the Degree of

Master of Science

August 2018

The thesis of Ganesh Venkatesan was reviewed and approved* by the following:

Charles E. Bakis
Distinguished Professor of Engineering Science and Mechanics
Thesis Advisor

Clifford J. Lissenden
Professor of Engineering Science and Mechanics

Michael C. Hillman
Assistant Professor of Civil and Environment Engineering

Judith Todd
Professor of Engineering Science and Mechanics
Head of the Department of Engineering Science and Mechanics

*Signatures are on file in the Graduate School

ABSTRACT

Hybrid fiber composites offer designers a means of tailoring the stress-strain behavior of lightweight materials used in high performance structures. While much experimental and analytical work has been done to characterize the behavior of hybrid composites in the direction parallel to the fibers, relatively little information is available on the direction transverse to the fibers. The objective of the current investigation is to evaluate several modeling approaches for the transverse properties of hybrid glass/carbon fiber composites based on comparisons with experimental data and investigate the load sharing mechanisms among different constituents in hybrid fiber composites under transverse stress. The experimental data include the transverse elastic properties and Poisson's ratio of unidirectional composites with all-glass, all-carbon, and three different mix ratios of glass/carbon. Included in the models are a finite element approach and closed-form micromechanical models with and without empirically determined fitting parameters. The finite element approach was used to evaluate the effects of voids in the matrix and allowed the transverse properties of carbon fibers to be backed out using experimental data. The finite element approach with voids modelled as empty cylinders can accurately simulate the experimentally measured modulus and Poisson's ratio. Of the two semi-empirical closed form models evaluated, the "modified iso-stress model" fit the transverse modulus data best, followed by the "modified Halpin-Tsai model". In order to investigate the load sharing mechanisms among different constituents in all-glass, all-carbon and hybrid composites stress partitioning, strain partitioning and energy partitioning parameters were analyzed. This analysis revealed that the fibers do not carry the same load when the proportions of glass-to-fiber ratio is varied. Also, in a composite where equal proportion of carbon fibers and glass fibers are mixed, the carbon fibers

undergo larger deformation than in any composite under transverse loading. This can be due to the presence of relatively stiff glass fibers adjacent on both sides. To gain more insights, the stress level, strain level, and energy level in each constituents were compared. The stress and strain level in the matrix could be modeled as springs in parallel and series, respectively, when the glass-to-carbon ratio was increased.

TABLE OF CONTENTS

LIST OF FIGURES

LIST OF TABLES

ACKNOWLEDGEMENTS

I would like to thank Dr. Charles E. Bakis for his continuous guidance and support throughout my graduate studies at Penn State. His persistence towards excellence and critical thinking helped me throughout my research. I would like to thank Mr. Max Ripepi for making the composites and measuring the transverse modulus and constituent contents. I thank Mr. Rudy Haluza for preparing the composite specimens for microscopy. Also the assistance of Mr. Jeffrey Kim with the experiments for measuring Poisson's ratio is appreciated. This research was supported by the Composites Manufacturing Technology Center at Penn State and the Department of Engineering Science and Mechanics at Penn State.

NOMENCLATURE

a_x, a_y, a_z: length of the RUC in x, y and z direction

$\bar{C}_{ij}$: reduced effective stiffness matrix

C_{11}, C_{22}, C_{33}: Components of stiffness matrix

dV: differential volume in the composite

E_g: Young's modulus of the isotropic glass fibers

E_m: Young's modulus of the isotropic matrix

$E_{1m}^{eff}, E_{2m}^{eff}$: effective Young's moduli of matrix with cylindrical voids in longitudinal direction and transverse direction, respectively

E_1, E_{1c}, E_{1f}: longitudinal Young's modulus of the composite, representative fibers and carbon fibers, respectively

E_2, E_{2c}, E_{2f} : transverse Young's moduli of the composite, representative fibers and carbon fibers, respectively

f_i: experimental value corresponding to iG_m: shear modulus of the isotropic matrix

G_{12m}^{eff}: effective shear modulus of the matrix in the longitudinal direction

K_{23m}^{eff}: effective plane strain bulk modulus of the matrix in the 2-3 plane

l, b, h : length, width and height of the beam specimens

L : outer load span

n : number of samples

P : total applied load

u_1, u_2, u_3: elemental displacements in 1, 2 and 3 direction, respectively

R^2: coefficient of determination

R_c, R_g, R_v : radius of carbon fibers, glass fibers and voids in RUC

$S_{11}, S_{22}, S_{33}, S_{12}, S_{13}, S_{23}$: Components of compliance matrix

v_{vm}: volume fraction of void in the matrix (not the entire composite)

v_v, v_c, v_g, v_m: volume fractions of void, carbon fibers, glass fibers and matrix, respectively, in the composite

V, V_c, V_g, V_m, V_v: volumes of the entire composite, carbon fibers, glass fibers, matrix and voids, respectively

x, y, z: Cartesian coordinates

y_i: value of sample i

$\bar{y}$: average value of samples y_i

$\bar{\Delta}$: thermodynamic constraint parameter

$\bar{\varepsilon}_{11}, \bar{\varepsilon}_{22}, \bar{\varepsilon}_{33}$: average strains in the composite in 1, 2 and 3 directions

$\bar{\varepsilon}_{22c}, \bar{\varepsilon}_{22g}, \bar{\varepsilon}_{22m}$: volumetric averages of strains in carbon fibers, glass fibers and matrix respectively

$\varepsilon_{22}, \varepsilon_{33}$: elemental strains in the composite in the 2- and 3-directions, respectively

$\eta_{\sigma c}, \eta_{\sigma g}$: stress partitioning parameters for carbon and glass fibers, respectively, for transverse normal stress

$\eta_{\varepsilon c}, \eta_{\varepsilon_g}$: strain partitioning parameters for carbon and glass fibers, respectively, for transverse normal strain

$\eta_{\psi c}, \eta_{\psi g}$: strain energy density partitioning parameters for carbon and glass fibers, respectively

ξ: Halpin-Tsai semi-empirical parameter for transverse normal stress

ν_{12c}, ν_{23c} : Poisson's ratios of carbon fibers in the longitudinal and transverse directions, respectively

ν_{12f} : Poisson's ratios of representative fibers in the longitudinal direction

ν_{12}, ν_{13}: longitudinal major Poisson's ratios of the composite

ν_{23}, ν_{32}: transverse Poisson's ratios of the composite

ν_{21}, ν_{31}: longitudinal minor Poisson's ratios of the composite

ν_g: Poisson's ratio of the isotropic glass fibers

$\nu_{12m}^{eff}, \nu_{23m}^{eff}$: effective Poisson's ratios of the matrix in the longitudinal and transverse planes, respectively

ρ : density of representative fibers

$\bar{\sigma}_{11}, \bar{\sigma}_{22}, \bar{\sigma}_{33}$: average normal stresses in the composite in 1, 2 and 3 direction.

$\bar{\sigma}_{22c}, \bar{\sigma}_{22g}, \bar{\sigma}_{22m}$: volumetric averages of stresses in carbon fibers, glass fibers and matrix, respectively, in the in-plane transverse direction

σ_{ii}: elemental axial stresses in the composite in *i* direction (i=1, 2, 3)

$\sigma_{22c}, \sigma_{22g}, \sigma_{22m}$: elemental stresses in carbon fibers, glass fibers and matrix, respectively, in the in-plane transverse direction

$\bar{\psi}_{22c}, \bar{\psi}_{22g}, \bar{\psi}_{22m}$: volumetric averages of strain energy density in carbon fibers, glass fibers and matrix

$\bar{\psi}$ **:** volumetric average of strain energy density of the composite

Chapter 1

INTRODUCTION

Laminated fiber reinforced polymer composites find widespread use in aerospace, mechanical, and civil engineering on account of their high strength/weight and stiffness/weight ratios along with their tailorable mechanical properties attainable by variation of fiber orientation. Another useful method of tailoring the mechanical behavior of composites is to combine two or more fiber types into a common matrix material, thereby creating "hybrid fiber composites" as shown in. The incorporation of multiple fiber types into the composite can balance the properties and cost of one type of fiber against the others. For example, it is known that carbon fibers have high longitudinal modulus, low longitudinal rupture strain, low transverse modulus, low mass density, and high cost in comparison to glass fibers (Daniel and Ishai, 2006). By combining both carbon and glass fibers, a balance in modulus, strain at failure and cost can be achieved. As a consequence, hybrid composites provide cost effective design solutions. Hybridization can also be used to improve the out-of-plane impact resistance and adjust the coefficient of thermal expansion of laminates (Short and Summerscales, 1980) and to model a pseudo-ductile failure mode in unidirectional composites under longitudinal (fiber direction) loading (Bakis et al., 2001).

Composite flywheels have been used as energy storing devices primarily in the automotive, satellite and electrical utility sectors (Genta, 1985). Ross (2013) showed that composite flywheels have higher specific energy and specific power than chemical batteries. Arvin and Bakis (2006) presented that minimizing residual stresses in rings can simplify a rotor design by reducing the number of rings required to maximize the specific energy. Therefore, flywheels can be an excellent

design substitute for chemical batteries. Nonetheless, there are limitations relating to the maximum strength which makes them susceptible to energy storage applications. Based on classical kinetic energy equation, stress distribution due to centrifugal field varies quadratically with angular velocity. Solving the field equations for stress by tailoring the hoop modulus of hoop-wound rims can optimize the performance of flywheels. Utilizing high strength composites for this application can be also favorable choice. However, these materials are inherently anisotropic, particularly if unidirectional composites are used, the low strength in the transverse direction constrain them for this application. By using a hybrid with a tailored hoop modulus that increases with increasing radius, the outer regions of the flywheel confine the inner regions and reduce the magnitude of tensile radial stress that otherwise would reduce the speed of the rotor. If a hybrid composite with stiffer reinforcements is used in order to increase the strength in weaker directions, the maximum strength of the material can be improved. S-glass is a cheaper material and has high specific strength, however, it has low Young's modulus and fatigue strength. Although Kevlar has high fatigue strength and Young's modulus than glass, it has low longitudinal compressive strength and it is susceptible to degradation from sunlight and moisture. Carbon fibers have higher longitudinal modulus and superior bonding strength than Kevlar. However, carbon fibers are anisotropic and the transverse modulus is lower than glass, as shown in Table 1. For utilizing these materials in various applications, it is important to know the Young's modulus of elasticity transverse to the fibers, E_2.

Table 1 . Elastic properties of various fibers used in composites, Daniel and Ishai (2006).

Fiber Type	Longitudinal Young's modulus of the fibers, E_1 (GPa)[1]	Transverse Young's modulus of the fibers, E_2 (GPa)[1]	Longitudinal Poisson's ratio of the fibers, ν_{12}[1]	Longitudinal Tensile Strength of fibers, F_{1T}(MPa)[1]	Density of the fibers, ρ (g/cm^3) [1]
E-Glass	73	73	0.23	3450	2.54
S-Glass	86	86	0.23	4500	2.49
AS4D Carbon	235	15	0.20	3700	1.81
Kevlar 49	131	7	0.33	3800	1.45

[1]Daniel and Ishai (2006)

Experimental data on the longitudinal modulus of elasticity of unidirectional hybrid composites is abundant in the literature (Bunsell and Harris, 1974; Kretsis, 1987; Short and Summerscales, 1980; Bakis et al. 2001; Jalalvand et al. 2015). The experimental longitudinal modulus agrees well with simple predictive micromechanical models such as volumetric averaging of the constituent moduli (rule of mixtures). While a few micromechanical models have been developed and validated for the transverse properties of non-hybrid fiber composites, very little data is available in the literature and, correspondingly, little is known about the accuracy of micromechanical models for simulating the transverse properties of hybrid fiber composites.

Halpin and Tsai provided an analytical model based on the "self-consistent micromechanics method" to predict E_2 non-hybrid fiber composites (Halpin and Kardos, 1976). Based on this work Bannerjee and Sankar (2012) developed a modified Halpin-Tsai model (MHTM) to include a second set of fibers, and determined the fitting parameter based on reference values provided by two-dimensional (2D) finite element analysis (FEA) predictions of E_2 of carbon/glass hybrids. However, they did not assess their predictions with experimental data.

A number of investigators (e.g., Sun and Vaidya, 1996; Gusev et al., 2000; Wongsto and Li, 2005; Barbero, 2013) used FEA to predict all five independent properties of unidirectional fiber composites with isotropic and orthotropic fibers but only Banerjee and Sankar (2012) examined unidirectional hybrid fiber composites with FEA. Invariably, all the papers using FEA neglected the presence of voids, which can be important for transverse properties. These and other investigations also used estimated transverse properties of carbon fibers or else backed out E_2 of carbon fibers from experimental data assuming no voids (Sun and Vaidya, 1996; King et al., 1992; Gipple and Hoyns, 1994; Grimes et al., 1980; Cairns and Adams, 1981).

The iso-stress model (ISM) (Daniel and Ishai, 2006) and doubly periodic model (DPM) (Van Fo Fy, 1969) have also been used to simulate E_2 of hybrid composites. The ISM is known to produce a lower bound estimate of modulus (Hashin and Shtrickman, 1963). DPM has been developed only for isotropic phases, which excludes carbon and other orthotropic fibers.

Tarnopol'skii et al. (1991) developed an anisotropic matrix model for E_2 of hybrid composites, where one set of fibers forms an intermediate composite according to the principles of minimum potential energy theory. The intermediate composite properties are used as the properties of an anisotropic matrix which can be reinforced by second set of fibers. This model includes orthotropic constituents, but like ISM it is also a lower bound estimate of E_2 (Christensen, 1979).

Ha et al. (2012) proposed a so-called modified iso-stress model (MISM) to predict E_2 of hybrid composites with isotropic or orthotropic constituents. The MISM includes stress partitioning parameters (SPPs), which are defined as the ratio of transverse stresses in the fiber to transverse stress in the matrix. Ha et al. (2012) determined the SPPs by best-fitting the model to experimental data for all-carbon and all-glass composites and used the SPPs to predict E_2 of carbon/glass hybrids without experimental validation.

None of the previous investigations concerned with the transverse properties of hybrid composites validated predictions with experimental data from hybrids. Recently, Bakis and Ripepi (2013) reported E_2 data for a family of glass and carbon hybrids ranging from 100% carbon (C100) to 100% glass (G100). The transverse moduli of the five composites—named C100, C75G25, C50G50, C25G75, and G100 according the volume percent of each fiber—were modeled using the ISM, MISM, and MHTM. Good results were obtained by the fitted models (MISM and MHTM), although ISM under-predicted E_2 as expected. The effects of voids on the inputted elastic

properties of the matrix were not considered and an estimated value was used for the transverse modulus of carbon fiber, E_{2c}. The longitudinal modulus of unidirectional composites, E_1, can be predicted accurately using the volumetric rule of mixtures (ROM) because (a) the iso-strain assumption inherent in the ROM is quite realistic for longitudinal behavior, (b) the fiber's longitudinal modulus can be readily measured, and (c) the effects of voids on the matrix modulus are relatively unimportant. However, to-date no effort have been made to model E_2 and ν_{23} with consideration given to matrix voids, including the transverse properties of carbon fiber, E_{2c} and ν_{23c}, which have been back-calculated with the same consideration given to matrix voids. Therefore, the objectives of the current investigation are to re-analyze the transverse modulus glass, carbon, and glass/carbon hybrid data by Bakis and Ripepi (2013), taking into account voids in the matrix and using values of E_{2c} and ν_{23c} that are consistent with the data. Also, the transverse stress and strain distributions in the matrix and the uniaxially aligned glass and/or carbon fibers under transverse loading conditions are calculated and discussed.

The remainder of the thesis is organized as follows. In Chapter 2, the micromechanical modeling approaches for the transverse Young's modulus of hybrid composites are presented. First, the finite element models and the boundary conditions pertinent to fiber packing arrangement and, the void modelling techniques are evaluated. Next, the governing equations utilized to develop the ISM, MISM and MHTM are analyzed.

In Chapter 3, the measurement of the elastic properties and volume fraction of the constituent material properties are discussed. The transverse moduli used in the current investigation came from Ripepi (2013), while the transverse Poisson's ratios were measured as part of the current investigation. The transverse Poisson's ratio of the composite are required for backing out the carbon fiber's transverse modulus and Poisson's ratio using FEA.

In Chapter 4, the results of experimentally measured transverse Poisson's ratio are presented. Next, the preliminary finite element models for fiber packing arrangement and void modeling techniques are assessed. Based on this information, the transverse elastic properties of carbon fiber properties are obtained from the carbon/epoxy composite properties using an inverse method. Mesh convergence studies are conducted to get the right mesh size that satisfactorily balances the accuracy of the solution and computing resources. Subsequently the transverse elastic properties of the hybrids obtained from FEA and the analytical models are reported. Stress partitioning parameters, strain partitioning parameters and energy partitioning parameters from the FE models of the composites are analyzed. Finally in Chapter 5, conclusions from the investigation are reported.

Chapter 2

MICROMECHANICAL MODELING APPROACH FOR TRANSVERSE YOUNG'S MODULUS

The transverse Young's modulus is modeled utilizing closed form models such as ISM, closed form models with semi-empirical parameters such as MISM and MHTM and finite element models. The voids in the composite are modeled both implicitly, by homogenizing the matrix using micromechanical equations and, explicitly by placing circular cylindrical holes in the matrix, whereas the closed-form models use only the homogenized matrix properties.

Finite element analysis (FEA)

Repeating unit cell (RUC)

Typically, numerical methods used to analyze the properties of the heterogeneous materials are developed based on concept of representative volume element (RVE) or repeating unit cell (RUC) as shown in Figure 1, Figure 2 and Figure 3. The RVE characterizes the heterogeneous material based on a statistically homogeneous microstructure whereas the RUC characterizes periodic heterogeneous material. These both concepts are based on different heterogeneous micro-structure and require different boundary conditions for micromechanical analysis of smallest sub-volume whose response is indistinguishable from that of a material at large scale level. Particularly the RVE enforces homogeneous traction or displacement boundary condition for micromechanical analysis, and RUC is based on periodic boundary conditions (Drago and Pindera, 2006).

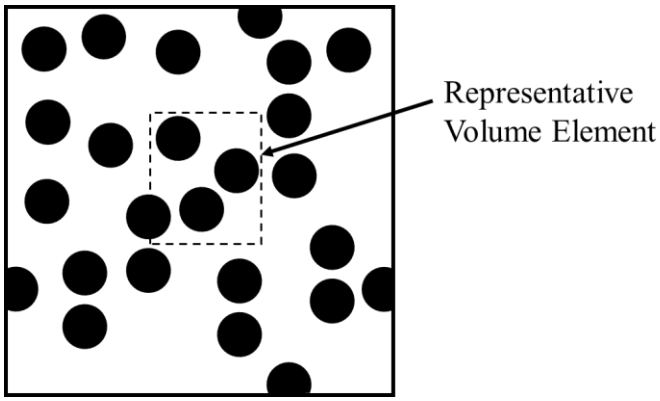

Figure 1. Representative volume element of a heterogeneous system with random array of fibers

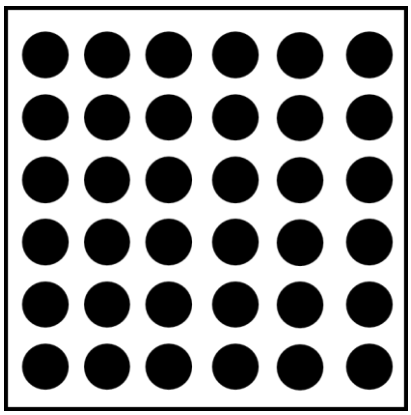

Figure 2. Repeating unit cell of a heterogeneous system with square array of fibers

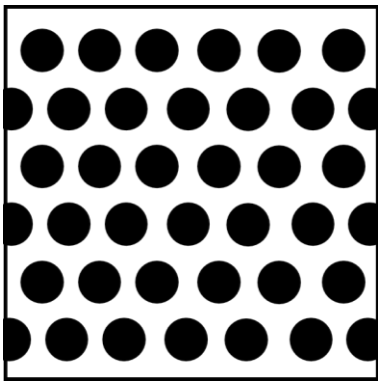

Figure 3. Repeating unit cell of a heterogeneous system with hexagonal array of fibers

The elastic properties of an RVE of heterogeneous material can be obtained from homogenization theory or standard mechanics. In homogenization theory, the material response is

modeled based on partial differential equations with rapidly oscillating coefficients. There are two major assumptions made in homogenization theory. First, the displacement field varies on multiple scales of the RVE and second, the microstructure is spatially periodic. In the asymptotic homogenization method, the displacements are asymptotically expanded as the sum of the average displacements of the RVE and oscillations in the displacements due to the chosen RVE size. In the standard mechanics approach, the RVE is subjected to uniform traction or uniform displacement boundary conditions. These boundary conditions are chosen so as produce an average strain or average stress within a homogeneous material of the same RVE size. Hollister and Kikuchi (1992) showed that prediction of stiffness by the standard mechanics approach using RVEs with an increasing number of unit cells converged to the homogenization prediction obtained with an RVE consisting of one unit cell. This is because the stiffness of the RVE from standard mechanics approach is dependent on the RVE size due to St. Venant's effect associated with the applied displacement or traction boundary condition. However, Drago and Pindera (2006) showed that the prediction of stiffness by the standard mechanics approach will not vary with an increasing number of unit cells if the microstructure of the composite is represented using an RUC with periodic boundary conditions. Since each RUC is indistinguishable from the next, the response of the entire array under macroscopically uniform loading is identical to the response of an arbitrary RUC under the same loading. Also, using the standard mechanics approach and representing the microstructure of the composite as an RUC with periodic boundary conditions is useful to understand the interactions among the constituents of the composites. Hence, the standard mechanics approach with periodic boundary conditions is adopted in the current investigation.

Usually, unidirectional composite materials are approximated by an RVE of periodic arrays of circular fibers arranged in square or hexagonal arrays (Sun and Vaidya, 1995). This

microstructure can be represented by a single fiber-matrix RUC adaptable to analysis by the finite element method. In any of the square and hexagonal packing systems, there exists many geometric symmetries. Due to these geometric symmetries, the application of homogeneous traction or displacement boundary conditions along with the geometric symmetry constraints on an RVE of square or hexagonal packing systems, is equivalent to the periodic boundary conditions enforced on an RUC with the same fiber arrangements. However, in unidirectional hybrid composites, the geometric symmetries no longer exist because the unit cell includes fibers with different material properties and diameters. The analysis of multi-fiber-matrix system cannot be restricted to the concept of RVE because some stress components show symmetric characteristics while others are asymmetric (Li, 2000). Therefore, the hybrid models are developed based on the concept of RUC.

Adams and Doner (1967) provided finite difference elasticity solutions for the transverse modulus of a glass/epoxy composite system using the RUC approach. Two important variables, filament cross section (circular and elliptical) and filament volume content (v_g = 0.2 to 0.75) were investigated. They showed that the prediction of transverse stiffness from the finite difference model was in good agreement with experimental data for a square array of circular fibers.

Gusev et al. (1999) measured the elastic constants of an E-glass fiber/913 epoxy resin composite with a fiber volume content of 54 % and compared the results to FEA predictions. They used periodic boundary conditions on RVE of hexagonal, square and random fiber arrays and found that the fiber packing arrangement had significant influence on the predicted transverse Young's modulus. They showed that hexagonal and random arrays under-predict E_2 by 11.7 % and 6.4 %, respectively, while the square array over-predicts with 6.4 % difference. However, without considering the void volume fraction, they conclude that random array predicts the elastic properties most accurately.

Sun and Vaidya (1995) used hexagonal and square arrays to predict the transverse Young's modulus of AS4/3501-6 composite with a fiber volume content of 60%. In order to evaluate the elastic properties of the arrays, they used homogeneous strain boundary conditions on the square and hexagonal RUCs. They showed that the hexagonal and square models both under-predict the experimentally measured transverse Young's modulus by 6.8% and 10.7% respectively. It appears that square model is always stiffer than hexagonal model even when the voids are not considered. Also, the properties of the carbon fibers used for the finite element models were obtained from a questionable source. In the current investigation, the best array for modeling transverse properties is determined by comparing experimental data with FEA results, for hexagonal and square arrays.

Transverse elastic properties of composite

In the current investigation, finite element models were developed using C3D8 mesh elements in ABAQUS 6.14 (Dassault Systèmes Americas Corp., Waltham, MA). C3D8 mesh elements are three dimensional continuum, 8-node linear bricks with 2×2×2 integration points. The C3D8 mesh element is defined with the isoparametric coordinate system with μ, τ and ζ as the axes, Figure 4. The shape functions used to interpolate discrete nodal quantities across the element are given by equations (1-(8). The node numbering scheme follows the convention as shown in Figure 4 and the integration points are numbered according to Figure 5.

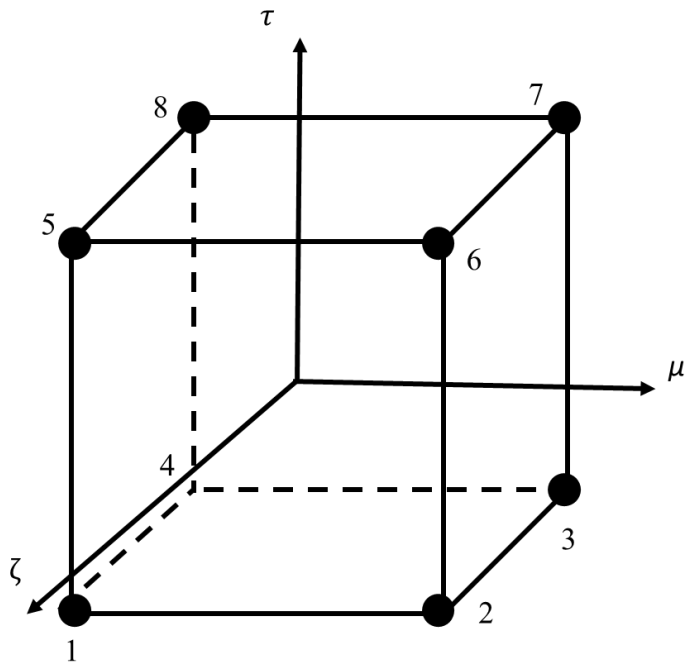

Figure 4. C3D8, three dimensional, 8-node linear brick element.

$$N_1 = \frac{1}{8}(1-\tau)(1-\mu)(1+\zeta) \quad (1)$$

$$N_2 = \frac{1}{8}(1-\tau)(1+\mu)(1+\zeta) \quad (2)$$

$$N_3 = \frac{1}{8}(1-\tau)(1+\mu)(1-\zeta) \quad (3)$$

$$N_4 = \frac{1}{8}(1-\tau)(1-\mu)(1-\zeta) \quad (4)$$

$$N_5 = \frac{1}{8}(1+\tau)(1-\mu)(1+\zeta) \quad (5)$$

$$N_6 = \frac{1}{8}(1+\tau)(1+\mu)(1+\zeta) \quad (6)$$

$$N_7 = \frac{1}{8}(1+\tau)(1+\mu)(1-\zeta) \quad (7)$$

$$N_8 = \frac{1}{8}(1+\tau)(1-\mu)(1-\zeta) \tag{8}$$

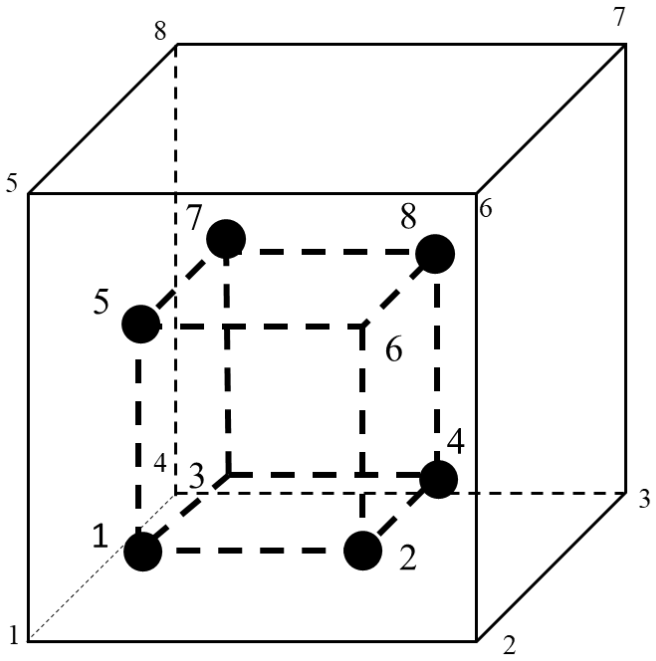

Figure 5. 2x2x2 integration points in the linear brick element

In general, composites with parallel fibers reinforcing a matrix exhibit transverse isotropy at the meso-scale (lamina level). The hexagonal RUC shown in Figure 3 exhibits hexagonal isotropy, thus it predicts the same modulus in any direction in the 2-3 plane. However, the square RUC in Figure 2 has only tetragonal isotropy in the 2-3 plane, meaning that the 2- and 3-direction moduli are the same as each other, but different than the moduli in other directions in the 2-3 plane. The reduced effective stiffness matrix, C_{ij}, which relates the volume averaged normal stresses and normal strains, is given by equation (9),

$$\begin{Bmatrix} \bar{\sigma}_{11} \\ \bar{\sigma}_{22} \\ \bar{\sigma}_{33} \end{Bmatrix} = \begin{bmatrix} \bar{C}_{11} & \bar{C}_{12} & \bar{C}_{13} \\ \bar{C}_{21} & \bar{C}_{22} & \bar{C}_{23} \\ \bar{C}_{31} & \bar{C}_{32} & \bar{C}_{33} \end{bmatrix} \begin{Bmatrix} \bar{\varepsilon}_{11} \\ \bar{\varepsilon}_{22} \\ \bar{\varepsilon}_{33} \end{Bmatrix} \quad (9)$$

where,

1-axis is aligned with the fiber direction.

$\bar{\sigma}_{11}, \bar{\sigma}_{22}, \bar{\sigma}_{33}$: average stresses in the composite in 1, 2 and 3 directions

$\bar{\varepsilon}_{11}, \bar{\varepsilon}_{22}, \bar{\varepsilon}_{33}$: average strains in the composite in 1, 2 and 3 directions

If the components of the elastic stiffness matrix are known, the four transverse elastic properties of the composite can be obtained from the reduced effective compliance matrix,$\bar{S}$, as shown in equation (10),

$$[\bar{C}]^{-1} = \bar{S}_{ij} = \begin{bmatrix} \frac{1}{E_1} & \frac{-\nu_{21}}{E_2} & \frac{-\nu_{31}}{E_3} \\ \frac{-\nu_{12}}{E_1} & \frac{1}{E_2} & \frac{-\nu_{32}}{E_3} \\ \frac{-\nu_{13}}{E_1} & \frac{-\nu_{23}}{E_2} & \frac{1}{E_3} \end{bmatrix} \quad (10)$$

where,

E_1: longitudinal Young's modulus of the composite

E_2: transverse Young's modulus of the composite

ν_{12}, ν_{13}: longitudinal major Poisson's ratios of the composite

ν_{23}, ν_{32}: transverse Poisson's ratios of the composite

ν_{21}, ν_{31}: longitudinal minor Poisson's ratios of the composite

In order to evaluate the reduced stiffness tensor, $\bar{C}_{ij}$, the RUC is subjected to uniaxial average strains, $\bar{\varepsilon}_{ii}$, on the RUC in the 1-, 2-, and 3-directions in sequence, Figure 6. The three components of normal strains $\bar{\varepsilon}_{ii}$ are applied on the RUC by enforcing the periodic boundary conditions given in Table 2. The constraint equations for the enforcing periodicity are automated using HOMTOOLs, a toolbox for ABAQUS developed by Lejeunes and Bourgeosis (2011).

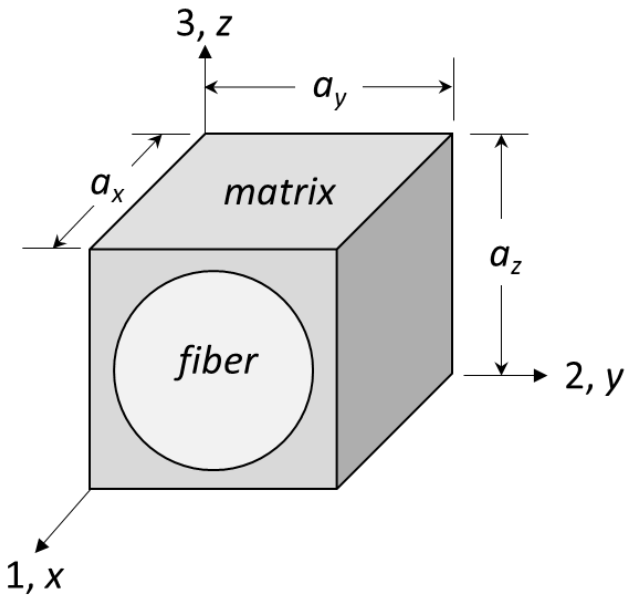

Figure 6. Composite material with fibers oriented in longitudinal or 1-direction.

Table 2. Periodic boundary conditions for determining the effective Young's moduli and Poisson's ratios of the RUC by applying uniaxial average strains in the 1-, 2-, and 3-directions.

1-direction	$u_1(a_x, y, z) - u_1(0, y, z) = a_x\bar{\varepsilon}_{11}$ for $0 \le y \le a_y$, $0 \le z \le a_z$
	$u_2(x, a_y, z) - u_2(x, 0, z) = 0$ for $0 \le x \le a_x$, $0 \le z \le a_z$
	$u_3(x, y, a_z) - u_3(x, y, 0) = 0$ for $0 \le x \le a_x$, $0 \le y \le a_y$
2-direction	$u_1(a_x, y, z) - u_1(0, y, z) = 0$ for $0 \le y \le a_y$, $0 \le z \le a_z$
	$u_2(x, a_y, z) - u_2(x, 0, z) = a_y\bar{\varepsilon}_{22}$ for $0 \le x \le a_x$, $0 \le z \le a_z$
	$u_3(x, y, a_z) - u_3(x, y, 0) = 0$ for $0 \le x \le a_x$, $0 \le y \le a_y$
3-direction	$u_1(a_x, y, z) - u_1(0, y, z) = 0$ for $0 \le y \le a_y$, $0 \le z \le a_z$
	$u_2(x, a_y, z) - u_2(x, 0, z) = 0$ for $0 \le x \le a_x$, $0 \le z \le a_z$
	$u_3(x, y, a_z) - u_3(x, y, 0) = a_z\bar{\varepsilon}_{33}$ for $0 \le x \le a_x$, $0 \le y \le a_y$

The terms in the above table represent,

u_1, u_2, u_3: elemental displacements in 1, 2 and 3 directions

a_x, a_y, a_z: length of the RUC in *x*, *y* and *z* directions

x, y, z: Cartesian coordinates

Thus, the components of $\bar{C}_{ij}$ are determined by solving three elastic models of the RUC subjected to the periodic boundary conditions in Table 2, where only one component of the strain, $\bar{\varepsilon}_{ii}$, is different from zero for each of the six problems (Barbero (2013)). By choosing a unit value of applied strain, it is possible to compute the stress field, $\bar{\sigma}_{ii}$, whose volume average gives the components of $\bar{C}_{ij}$ one column at a time, given by (11),

$$\bar{C}_{ij} = \bar{\sigma}_{ii} = \frac{1}{V}\int_0^V \sigma_{ii} dV \text{ (no summation implied) with } \bar{\varepsilon}_{ii} = 1 \tag{11}$$

where,

σ_{ii}: elemental axial stresses

V: volume of the entire RUC, including voids

The integral in (11) is evaluated at each mesh element in finite element method. To expedite the calculation, the average stresses and volume over the entire RUC are computed using automated Python scripts. Example scripts are provided in Appendix A.

Determination of stress partitioning parameters (SPPs)

Stresses in the fiber and matrix are unequal under transverse loading. Characterizing these stresses in the constituent materials can give a physical understanding of the composite behavior. The stress partitioning parameter (SPP) is defined as the ratio of the volume-averaged 2-direction stress in a particular type of fiber to the volume-averaged 2-direction stress in the matrix when a uniaxial 2-direction stress is applied to the RUC with appropriate periodic boundary conditions. The SPPs for glass and carbon fibers are given by equations (12) and (13), respectively,

$$\eta_{\sigma g} = \frac{\frac{1}{V_g}\int \sigma_{22g}(x,y,z)dV_g}{\frac{1}{V_m+V_v}\int \sigma_{22m}(x,y,z)dV_{m+v}} \tag{12}$$

$$\eta_{\sigma c} = \frac{\frac{1}{V_c}\int \sigma_{22c}(x,y,z)dV_c}{\frac{1}{V_m+V_v}\int \sigma_{22m}(x,y,z)dV_{m+v}} \tag{13}$$

where,

$\eta_{\sigma g}, \eta_{\sigma c}$: stress partitioning parameters for glass and carbon fibers, respectively, for transverse normal stress

$\sigma_{22g}, \sigma_{22c}, \sigma_{22m}$: 2-direction stresses in glass and carbon fibers and in the matrix, respectively

V_g, V_c, V_m, V_v: volume of glass, carbon, matrix and voids, respectively

The matrix volume in the denominator of the denominator in equations (12) and (13) includes solid matrix material and empty void space, regardless whether the voids are modeled implicitly or explicitly.

The periodic boundary conditions for determining the stress partitioning parameters when $\bar{\sigma}_{22}$ is applied to the RUC are given in equation (14),

$$\begin{aligned} u_1(a_x, y, z) - u_1(0, y, z) &= -a_x \nu_{21} \bar{\varepsilon}_{22} \text{ for } 0 \le y \le a_y,\ 0 \le z \le a_z \\ u_2(x, a_y, z) - u_2(x, 0, z) &= a_y \bar{\varepsilon}_{22} \text{ for } 0 \le x \le a_x,\ 0 \le z \le a_z \\ u_3(x, y, a_z) - u_3(x, y, 0) &= -a_z \nu_{23} \bar{\varepsilon}_{22} \text{ for } 0 \le x \le a_x,\ 0 \le y \le a_y \end{aligned} \tag{14}$$

where, $\bar{\varepsilon}_{22}$ is taken as unity and ν_{21} and ν_{23} are the Poisson's ratios of the composite from equation (10).

Explicit modeling of voids

The shape of voids can have significant influence on the elastic properties of fiber composites. Goldsmith et al. (2013) modeled the voids in woven ceramic matrix composites as cuboids using FEA. They varied the aspect ratio (ratio of length to height), the number of voids, and the position of voids and predicted the transverse stiffness of the voidy matrix. However, this work was done to gain only a preliminary insight into the variability in void size and distribution

in woven ceramic matrix composites, as compared to unidirectional composites. Moreover, no experimental data for validation were provided for comparisons.

Talreja and Huang (2005) used FEA and Eshelby's equivalent inclusion theory to study the effect of void geometry and distribution on the elastic properties of carbon/epoxy composites with a fiber volume content of 40 %. They modeled the voids as prolate ellipsoids, flattened in the through-thickness direction.

In the current investigation, voids are explicitly modeled as infinitely long cylindrical holes based on their approximate shapes as seen in photomicrographs of the materials (Figure 7 and Figure 8)**.** The images were taken by Mr. Rudy Haluza and the polishing procedures are explained in Appendix B.

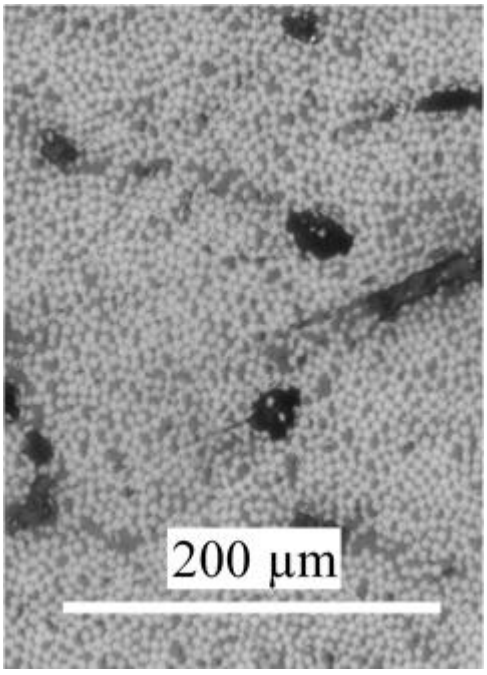

Figure 7. Photomicrograph of a polished plane of a unidirectional ASD4 carbon/epoxy composite (C100) perpendicular to the fibers. The darkest regions are voids.

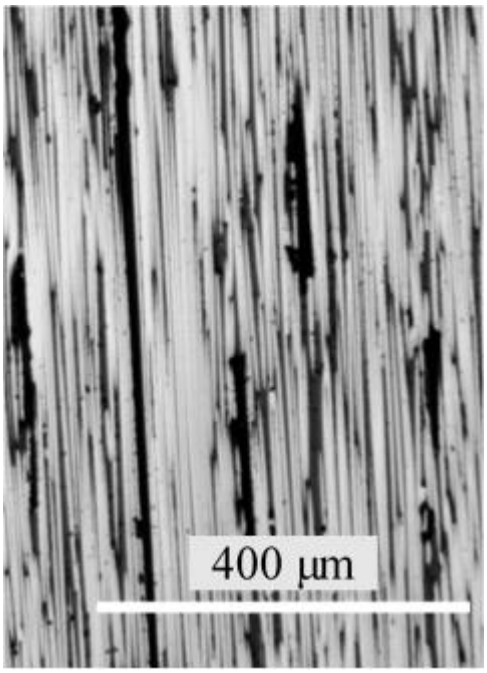

Figure 8. Photomicrograph of a polished plane of a unidirectional ASD4 carbon/epoxy composite (C100) nearly parallel to the fibers. The darkest regions are voids.

Implicit modeling of voids

For the implicit model of voids, the effective hexagonally transversely isotropic elastic properties of the matrix material containing an array of parallel cylindrical voids of a known volume fraction within the matrix volume, v_{vm}, are calculated using the "generalized self-consistent method" (GSCM) by Christensen (1993), as shown in equations (15)-(21),

$$\frac{E_{1m}^{eff}}{E_m} = 1 - v_{vm} \tag{15}$$

$$\nu_{12m}^{eff} = \nu_m \tag{16}$$

$$\frac{K_{23m}^{eff}}{G_m} = \frac{1 - v_{vm}}{1 - 2\nu_m + v_{vm}} \tag{17}$$

$$\frac{G_{12m}^{eff}}{G_m} = \frac{1 - v_{vm}}{1 + v_{vm}} \tag{18}$$

$$\frac{E_{2m}^{eff}}{E_m} = \frac{v_{vm}(1 - 2v_{vm} - {v_{vm}}^2) + \sqrt{[(1 + v_{vm} + {v_{vm}}^2 + {v_{vm}}^3)^2 - 12{v_{vm}}^2]}}{1 + 5v_{vm} + 2{v_{vm}}^2} \tag{19}$$

$$G_{23m}^{eff} = \frac{-K_{23m}^{eff}}{1 + 4K_{23m}^{eff}\left(\frac{\left(\nu_{12m}^{eff}\right)^2}{E_1} - \frac{1}{E_2}\right)} \tag{20}$$

$$\nu_{23m}^{eff} = 1 - \frac{E_{2m}^{eff}}{2G_{23m}^{eff}} \tag{21}$$

where,

$E_{1m}^{eff}, E_{2m}^{eff}$: effective Young's moduli of matrix with cylindrical voids in longitudinal direction

G_m: shear modulus of the isotropic matrix

G_{12m}^{eff}: effective shear modulus of the matrix in the longitudinal direction

K_{23m}^{eff}: effective plane strain bulk modulus of the matrix in the 2-3 plane

v_{vm}: volume fraction of void in the matrix (not the entire composite)

v_m: volume fraction of matrix in the composite

ν_m: Poisson's ratio of the isotropic matrix

$\nu_{12m}^{eff}, \nu_{23m}^{eff}$: effective Poisson's ratios of the matrix in the longitudinal and transverse planes, respectively

Transverse elastic properties of carbon fiber

Carbon fibers are commonly assumed to have transversely isotropic elastic properties (Daniel and Ishai, 2006). Although the elastic modulus and sometimes the Poisson's ratio of carbon fibers in the longitudinal direction are available, the modulus and Poisson's ratio in the transverse plane have not been directly measured, even though they are of high importance for modeling the transverse elastic properties of fiber composites. This information can be obtained either from nano-indentation techniques or by backing out from the experimental data (volume fraction and elastic properties) by utilizing FEA.

Huson et al. (2014) used instrumented indentation testing to obtain the modulus of IM7, P25, and Panex 35 carbon fibers. The modulus was obtained by analyzing the unloading region of the load-displacement curves using unmodified Olive-Pharr (O_P) methodology. However, this methodology is derived for a flat isotropic half-plane and cannot be used to model heterogeneous materials like carbon fibers.

Maurin et al. (2008) measured the transverse modulus of three high modulus (M40, M46 and K63712) carbon fibers using nano-indentation measurements and compared it to moduli back-calculated by applying micromechanical modelling to experimental measurements on unidirectional composites. They report that the micromechanics-derived moduli were similar to but tended to underestimate the directly measured nano-indentation values. This may result from using simplified assumptions such as the unmodified O-P equations.

One of the primary assumptions of the standard Oliver-Pharr theory is that the fiber is flat, semi-infinite half space. Cole et al. (2016) modified the O-P equations by accounting for curvature of tested single fibers and structural compliance due to sample geometry (as opposed to material

compliance). Although they modified the O-P equations for fibers that are not semi-infinite half spaces, the assumption of isotropy in the fibers is still there.

In general, though attempts have been made to measure the transverse modulus of carbon fiber using nano-indentation techniques, the models used to extract the transverse fiber modulus from the indentor's load-displacement behavior are based on isotropic target materials, which raises questions about the validity of the results for carbon fibers. In the current investigation, the carbon fiber properties are back calculated utilizing FEA based on the knowledge of the fiber volume content and matrix elastic properties (e.g., Maurin et al., 2008; Miyagawa et al., 2016). Although, unlike the previous investigations, an effort is made to include the effects of matrix voids on the back-calculated carbon properties.

Closed form micromechanical models

Iso-stress model

Iso-stress model provides a lower bound estimate for elastic properties in the transverse direction. In this method, the composite system is subjected to uniform stress in the direction perpendicular to fiber and, to a first approximation, the fibers and the matrix have the same homogeneous uniaxial stress in the transverse direction yet different strains (Hashin and Shtrickman, 1963). The expression for the transverse modulus is given by equation (22).

$$\frac{1}{E_2} = \frac{(v_m + v_v)}{E_{2m}^{eff}} + \frac{v_g}{E_g} + \frac{v_c}{E_{2c}} \tag{22}$$

where,

v_v, v_c, v_g, v_m: volume fractions of void, carbon fibers, glass fibers and matrix, respectively, in the composite

Banerjee and Sankar (2012) used a similar expression in their work on carbon/glass hybrids, although they used the modulus of the fully dense matrix, E_m, rather than the effective transverse modulus of the matrix including voids, E_{2m}^{eff}, because voids were not considered in their investigation.

Modified iso-stress model

The modified iso-strain model (MISM) for the transverse modulus of carbon/glass hybrids is shown in equations (23)-(25).

$$\frac{1}{E_2} = \left(\frac{(v_m + v_v)}{E_{2m}^{eff}} + \frac{\eta_g v_g}{E_g} + \frac{\eta_c v_c}{E_{2c}}\right) / \left(v_m + v_v + \eta_g v_g \ + \eta_c v_c \ \right) \tag{23}$$

$$\eta_g = \frac{\bar{\sigma}_{22g}}{\bar{\sigma}_{22m}} \tag{24}$$

$$\eta_c = \frac{\bar{\sigma}_{22c}}{\bar{\sigma}_{22m}} \tag{25}$$

Ha et al. (2012) used the MISM equations with the modulus of fully dense matrix, E_m, without including the effect of voids. They determined the stress partitioning parameters for carbon and glass (η_c and η_g, respectively), based on undisclosed experimental data from all-carbon and all-glass composites. As well, their source for the carbon fiber's transverse modulus was not disclosed. The values of η_c and η_g found by Ha et al. were 1.48 and 3.78, respectively.

Modified Halpin-Tsai model

The modified Halpin-Tsai model (MHTM) for the transverse modulus of carbon/glass hybrids is given in equations (26)-(28).

$$\frac{E_2}{E_{2m}^{eff}} = \frac{1 + \xi(\beta_g v_g + \beta_c v_c)}{1 - (\beta_g v_g + \beta_c v_c)} \tag{26}$$

$$\beta_g = \frac{\frac{E_g}{E_{2m}^{eff}} - 1}{\frac{E_g}{E_{2m}^{eff}} + \xi} \tag{27}$$

$$\beta_c = \frac{\frac{E_{2c}}{E_{2m}^{eff}} - 1}{\frac{E_{2c}}{E_{2m}^{eff}} + \xi} \tag{28}$$

where,

ξ: Halpin-Tsai semi-empirical parameter for transverse normal stress

Banerjee and Sankar (2012) determined the fitting parameter, ξ, based on FEA predictions of E_2, assuming a void-free matrix (i.e. $E_{2m}^{eff} = E_m$) and carbon fiber transverse modulus of uncertain provenance. The RUC used for their FEA consisted of 50 fibers carbon and glass fibers with combined volume fraction of 60% distributed randomly in the matrix. They found that ξ=1.14 gave the best fit to the virtual data. The MHTM model cannot explicitly account for voids. The only way to include voids is by adjusting the transverse modulus of matrix. Results of this analysis along with the modified Halpin-Tsai model are tabulated in Table 3.

Table 3. Results of FEA and modified Halpin-Tsai equation for glass/carbon hybrid composite (Banerjee and Sankar, 2012)

Composite	V_c (%)	V_g (%)	FEA, E_2 (GPa)	Modified Halpin-Tsai, E_2 (GPa)	Difference[1] (%)
Carbon/Epoxy	60	0	8.77	8.59	2.1
Carbon and Glass Epoxy Hybrids	54	6	9.05	8.88	1.9
	42	18	9.66	9.52	1.5
	30	30	10.33	10.22	1.1
	18	42	11.05	11	0.5
	6	54	11.82	11.86	-0.3
Glass/Epoxy	0	60	12.21	12.33	-1.0

$Difference(\%) = \frac{{E_2}^{FEA} - {E_2}^{MHTM}}{{E_2}^{FEA}} \cdot 100\ \%$

Chapter 3

SPECIMEN PREPARATION AND TESTING

Ripepi (2013) manufactured carbon and glass hybrid fiber composites in-house using a wet filament winding process. Also, he measured the transverse Young's modulus of the composite in flexure and the volume fractions of the constituents using a resin digestion method. All these findings were used in the current analytical and finite element investigations.

Specimen preparation

Hybon 2022 low-boron E-glass fibers of 1100 g/km tex from PPG (Pittsburgh, PA, USA), AS4D-GP-12K carbon fibers of 765 g/km tex from Hexcel (Stamford, CT, USA), and Epon 862/Epikure W epoxy (Momentive, Columbus, OH, USA) were used to wind the rings. The selected fiber tex values provide roughly similar cross-sectional fiber areas. The isotropic E-glass fiber is assumed to have an elastic modulus (E_g) of 80.0 GPa and a Poisson's ratio (ν_g) of 0.26 based on personal communication with the manufacturer. For the carbon fiber, the longitudinal modulus (E_{1c}) and Poisson's ratio (ν_{12c}) are assumed to be 245 GPa and 0.2, respectively, based on data provided by the manufacturer (Hexcel, 2013). Nominal proportions of fibers of 100% carbon (C100), 75% carbon/25% glass (C75/G25), 50% carbon/50% glass (C50/G50), 25% carbon/75% glass (C25G75), and 100% glass (G100) were obtained by pulling various combinations of tows through the resin bath and onto the mandrel at once, resulting in ring cross-sections as shown in Figure 9 (a-e) for the five types of composites. For example, the C75G25 ring

was made by winding three tows of carbon and one tow of glass side-by-side on the mandrel. Additional details about the manufacturing procedures are available in Ripepi (2013).

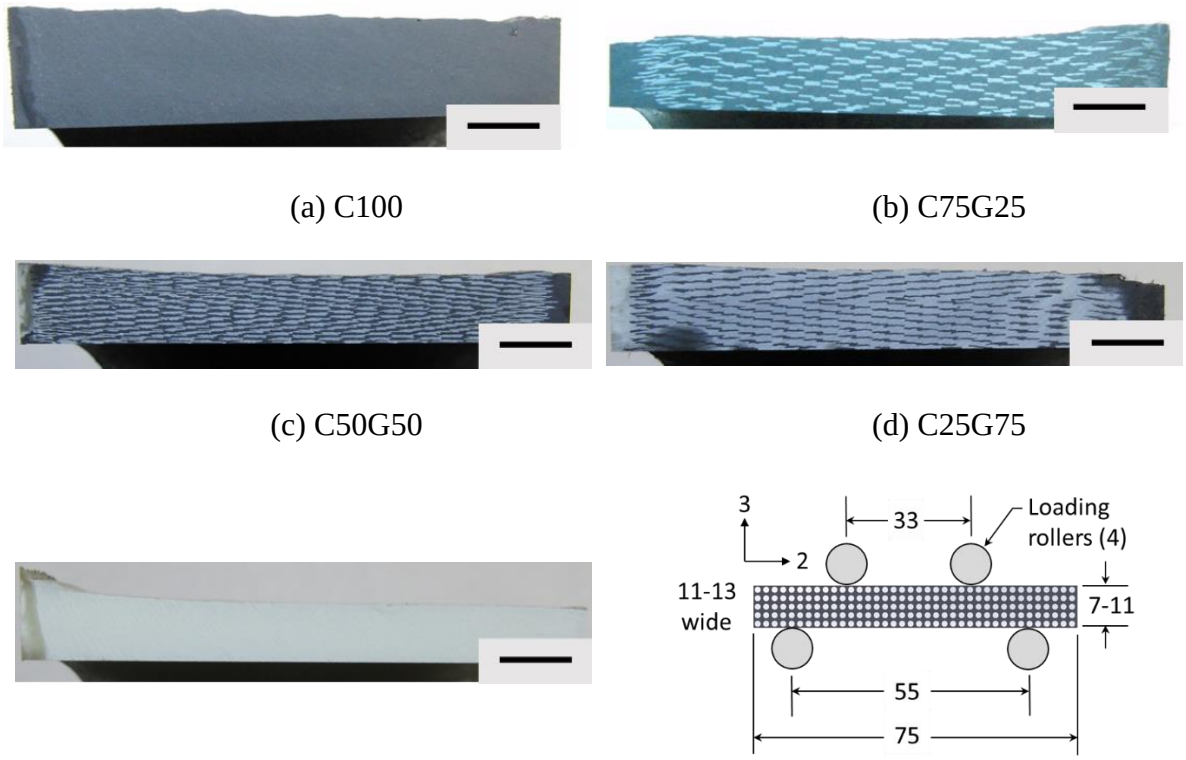

(a) C100 (b) C75G25

(c) C50G50 (d) C25G75

(e) G100 (f) Beam test geometry (mm)

Figure 9. Photographs of axially-cut cross sections of as-wound composite rings before machining (a-e) and 4-point-loaded beam geometry for measurement of transverse modulus (f). Scale marker in photographs is 10 mm (Ripepi, 2013).

For three-dimensional (3D) finite element analysis, it is important to know the transverse Poisson's ratio, ν_{23}, of the composite and this data is not reported by Rippepi. Therefore, in the present investigation additional beam specimens were cut from the filament wound rings and tested using biaxial strain gages. They were prepared by grinding procedures similar to those followed by Ripepi (2013).

One specimen from each of the five hybrid rings were extracted using a Felker 41-AR table saw with a water-cooled, diamond-edged cutting wheel. The specimens were ground until a constant cross section was achieved using a Norton General Purpose 100 Fine Grit, 6-in. dia., 0.5-inch wide, Alundum grinding wheel, in the Composites Manufacturing Technology Center at Penn State University-UP. In order to prevent damage in the specimen due to excessive heating, water cooling applied to the surface being ground. The top and bottom surfaces of each specimen were ground until planar parallel surfaces was achieved. After the grinding procedure was complete, the specimens were placed in a convection oven for 3 hours that was maintained at 155 °F temp. This assured that the specimens were dry and prepared for testing. The average beam dimensions of each specimen used for Poisson's ratio, ν_{23}, measurement are shown in Table 4.

Table 4. Average beam dimensions of the composites used for measurement of the transverse Poisson's ratio, ν_{23}.

	Length, *l* (mm)	Width, *b* (mm)	Height, *h* (mm)
C100	74.4	13.2	9.3
C75G25	75.2	6.6	11.4
C50G50	75.2	6.9	9.6
C25G75	75.2	8.4	8.6
G100	74.4	6.2	15.5

Testing methods

Transverse modulus measurements by Ripepi (2013)

The E_2 measurements used for comparison with models in the present investigation were obtained by Ripepi (2013) using four-point-loaded beams. Between six and 13 specimens of each

type were tested. Strain in the longitudinal direction of the beam was measured using a 9.5-mm clip-on extensometer. To calculate E_2, Ripepi used a chord modulus measurement between two strains corresponding to roughly 25% and 50% of ultimate. For Ripepi's composite specimens, the fibers were oriented perpendicular to the long axis of the beam, in the horizontal plane (Figure 9 (f)). Ripepi showed in preliminary testing that the modulus of G100 was the same in tension and compression. Therefore, all of his E_2 results are based on tensile strain measurements. However, Ripepi had an error in his load cell calibration, resulting in all his moduli being 5% low. This error has been corrected in the current investigation.

Transverse Poisson's ratio measurements

For the transverse Poisson's ratio measurements obtained in the present investigation (ν_{23}), one composite beam of each type was tested with the fibers oriented transverse to the longitudinal direction of the beam, in the vertical plane (Figure 10). The tests were performed on a servo-hydraulic load frame with a 13.34 kN load cell (Figure 11 and Figure 12). The displacement rate of the actuator was set to 1.27 mm/minute. Initially the strains in 2 and 3 direction in C100 and G100 beam were tested with FCA-1-11-1LT biaxial strain gage procured from Tokyo Sokki Kenkyujo Co., Ltd. The strain gages were attached to the tensile side of the beam. The gage length of this strain gage is 1 mm. In order to check if the gage length influenced the Poisson's ratio measurement, a FCA-2-11-3L biaxial strain gage procured from Tokyo Sokki Kenkyujo Co., Ltd was used to record the biaxial strains in G100 beam. The gage length of this strain gage is 2 mm and the transverse sensitivity is 0.2%. For the subsequent testing of the hybrids, the FCA-2-11-3L biaxial strain gage were used because it had better transverse sensitivity (0.1%). Reference values

of the transverse Young's modulus, E_2, were calculated from these tests only for a rough check of the corrected E_2 data by Ripepi (2013). These strain-gage-based values of E_2 were not used as the basis of comparison with models in the current in this investigation. Certain specimens were repeatedly tested up to three times with the single biaxial strain gages located on the tension side and three more times with the gages on the compression side. This was done to check for repeatability as well as differences in the strains measured in tension and compression. However, rigorous calculation of different tensile and compressive moduli (as in Ripepi, 2013) was not done. Load and strain data were recorded using a National Instruments SCB-68 data acquisition board. The flexural loading set up is shown in Figure 11 and Figure 12.

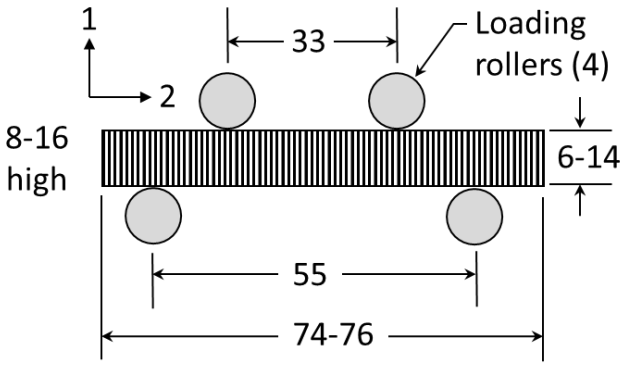

Figure 10. Four-point-loaded beam geometry for measurement of transverse Poisson's ratio, ν_{23}.

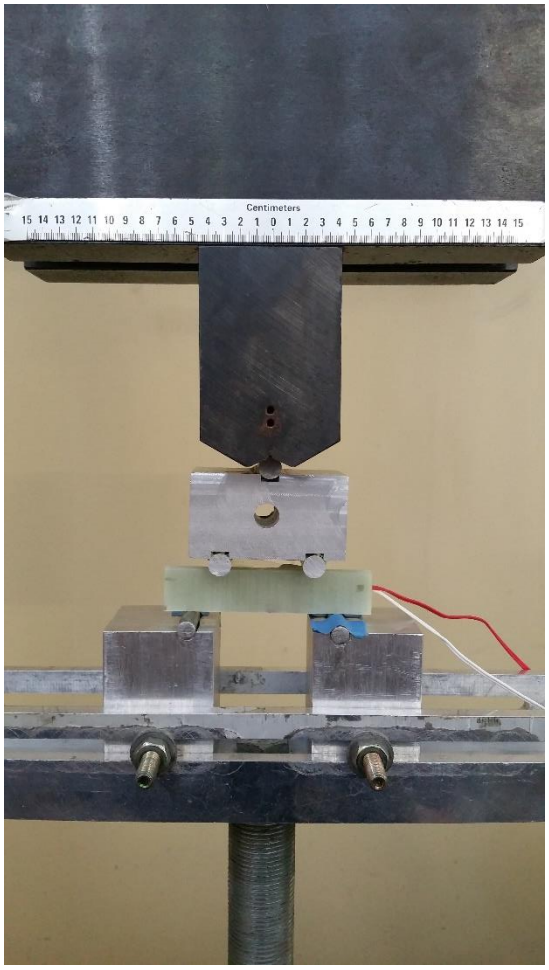

Figure 11. Flexure test setup of G100 specimen with load frame and, biaxial strain gage attached to the tension side of the beam.

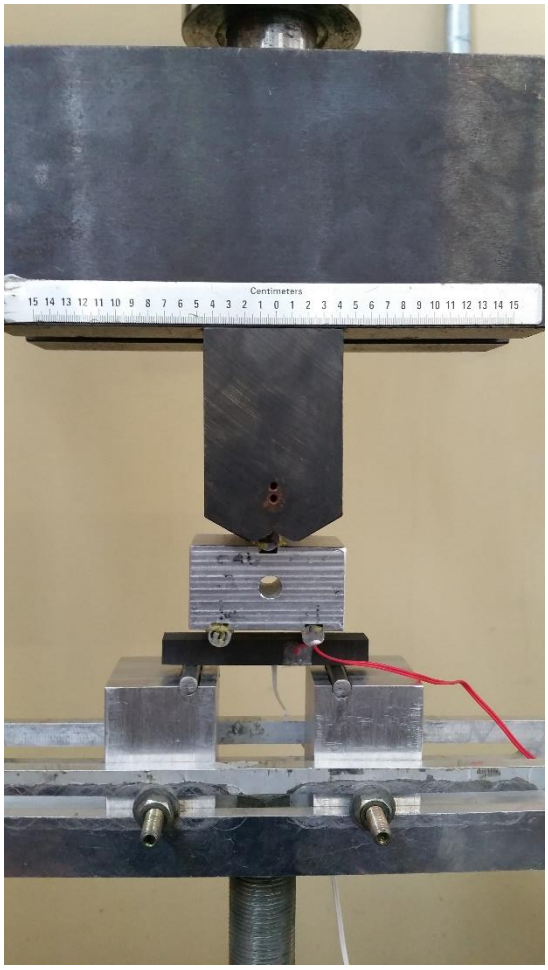

Figure 12. Flexure test setup of C100 specimen with load frame and, biaxial strain gage attached to the tension side of the beam.

The modulus was calculated using classical Euler-Bernoulli beam theory, based on a linear regression of the stress-strain data. For a 4-point-loaded beam with an outer span L, inner span $3L/5$, and shear span $L/5$, the flexural stress is given by

$$\sigma_{22} = \frac{3PL}{5bh^2} \tag{29}$$

where,

P: total applied load

L: outer load span

b: width of the beam

h: height of the beam

With the stress in the beam with equation (29) and the strains from the biaxial strain gage, the transverse modulus and transverse Poisson's ratio were determined from equations (30) and (31), respectively,

$$E_2 = \frac{\sigma_{22}}{\varepsilon_{22}} \tag{30}$$

$$\nu_{23} = -\frac{\varepsilon_{33}}{\varepsilon_{22}} \tag{31}$$

where,

ε_{22} and ε_{33} : strains in the 2- and 3-directions, respectively

An FE analysis of a G100 beam specimen was carried out to verify that the experimentally measured strains would reflect the actual properties of the material. The results of this analysis, detailed in Appendix D, indicate that the selected beam geometry provides an accurate measure of the modulus and Poisson's ratio of the material.

Carbon, glass, matrix, and void volume fractions of the composites were measured and reported by Ripepi (2013) using acid digestion (ASTM D3171-09, 2009). Carbon and glass volume fractions were individually calculated from the total fiber mass using the known tex values and mass densities for the two kinds of fiber.

Chapter 4

RESULTS

Transverse Poisson's ratio measurements

Mean volume fractions from three replicates of each material from the acid digestion tests by Ripepi (2013) are reported in Table 7. The volume fraction of voids in the matrix, v_{vm}, found by dividing v_v by v_m, is used when calculating effective matrix properties according to the GSCM discussed earlier. The stress-strain curves of the transverse Poisson's ratio measurements obtained from the biaxial gages attached on the tensile and compressive side are presented in Appendix C. The results from the Tensile side test and compressive side test of G100 beam showed that there was no influence of the gage length on the Poisson's ratio measurement.

Ripepi calculated and confirmed that measuring the elastic properties of the material by attaching the strain gages on the tensile side of the beam is an accurate test method. Therefore, the average Poisson's ratio results (Table 5) obtained from the biaxial strain measurements on the tensile side of the beam are used in the closed-form models and the finite element validation. Although the transverse Young's modulus from the biaxial strain gage measurement was not used in the present investigation, the values obtained from the strain gage measurements on the tensile side of the beam are compared to the corrected data by Ripepi (2013), in Table 6.

Table 5. Experimental transverse Poisson's ratio, ν_{23}, of composite beams from current investigation.

	Transverse Poisson's Ratio ν_{23}
C100	0.49
C75G25	0.41
C50G50	0.42
C25G75	0.42
G100	0.32
Neat Resin	0.38[1]

[1]Henry (2015)

Table 6. Experimental modulus of elasticity of beams from current investigation and Ripepi (2013).

	Modulus	
	E_2 (GPa) from current investigation	E_2 (GPa)* (corrected values from Ripepi, 2013)
C100	10.6	11.5±0.31
C75G25	14.6	13.7±0.67
C50G50	17.3	17.8±0.53
C25G75	21.8	19.9±0.51
G100	30.8	29.0±1.80
Neat Resin	-	3.07±0.15

*Mean±std. dev.

Table 7. Constituent volume fractions from Ripepi (2013).

	v_c	v_g	v_m	v_v	v_{vm}
C100	0.688	0.000	0.275	0.037	0.14
C75G25	0.536	0.176	0.263	0.025	0.095
C50G50	0.352	0.346	0.289	0.013	0.045
C25G75	0.176	0.518	0.274	0.032	0.120
G100	0.000	0.761	0.219	0.020	0.091

The E_2 of the specimens increases monotonically with higher proportions of glass fiber in the composite. This is attributed to the inclusion of glass fibers in the hybrids which have higher fiber modulus, E_{2g}= 80 GPa, than carbon fibers, E_{2c}= 25.3 GPa. The ν_{23} of the all-glass composite is lower than all-carbon and the hybrids. The reason for the low Poisson's ratio of the all-glass

material may be due to a lower glass fiber transverse Poisson's ratio, ν_{23g}= 0.26 compared to carbon fibers, ν_{23c}= 0.85. The transverse modulus and transverse Poisson's ratio of carbon are determined in the "Transverse elastic properties of AS4D carbon fibers" subsection later in this chapter.

The Poisson's ratio of the epoxy resin was not measured in the present investigation. Rather, the value of 0.38±0.14 obtained by Henry et al. (2015) using tensile tests on the same resin system was used.

FEA of hybrid composites

RUC fiber packing array

The fiber packing array used for the majority of the modeling was selected based on a preliminary model of the G100 composite without consideration of voids. Accordingly, the fiber and matrix volume fractions were set to 0.761 and 0.239, respectively. Square and hexagonal packing arrays were considered (Figure 13 (a) and (b)) using the dimensions shown in Table 8. Considering hexagonal symmetry, the hexagonal array predicts the same modulus in any direction in the 2-3 plane. The square array has only tetragonal symmetry in the 2-3 plane. Thus, modulus for the square array was evaluated along the direction of minimum inter-fiber distance (Figure 13 (b)) as well as along the direction of maximum inter-fiber distance (Figure 13(c)). The isotropic properties of the fully dense matrix material used for this part of the investigation are reported in Table 5 and Table 6. The modulus was calculated along the 2-axis in each RUC. In order to validate the periodicity boundary conditions used to model the E_2 and ν_{23}, the periodicity boundary

conditions in Table 2 were prescribed to a square RUC developed by Sun and Vaidya (1995) for a carbon epoxy (AS4/3501-6) composite with fiber volume fraction of 0.6. The given material properties were taken as the input properties of the validation RUC and the transverse elastic properties were computed. The computed values presented in Appendix E showed that the periodicity conditions used in the present analysis are correct. Based on these results the periodicity conditions were used to model subsequent finite element models of all-carbon, all-glass and hybrid composites.

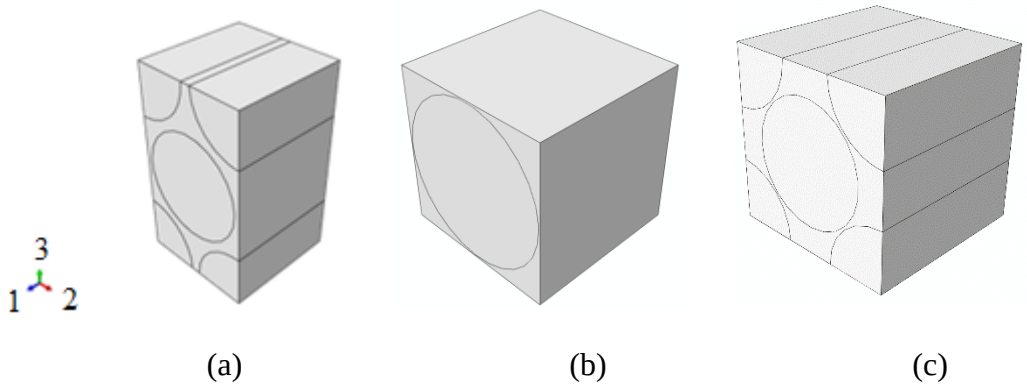

(a) (b) (c)

Figure 13. RUCs for different fiber packing arrays and modulus directions: (a) hexagonal; (b) square, minimum inter-fiber distance; (c) square, maximum inter-fiber distance. Modulus was calculated along the 2-axis in each RUC.

Table 8. Dimensions of RUC of hexagonal; square array, minimum inter-fiber distance and square array, maximum inter-fiber distance.

Property	Hexagonal array	Square array, minimum inter-fiber distance	Square array, maximum inter-fiber distance
Length, a_x (μm)	18.2	17.3	17.27
Breadth, a_y (μm)	32.2	17.3	24.4
Height, a_x (μm)	18.2	17.3	24.4
Glass fiber radius, R_g (μm)	8.5	8.5	8.5

The periodicity boundary conditions were enforced on the square and hexagonal RUCs, and the results of the study are shown in Table 9. These results reveal significant under-predictions of the transverse modulus, relative to the experimental reference value, for the hexagonal array and the square array along the maximum inter-fiber distance. These results are coherent with the results obtained by Gusev et al. (1999) and, Sun and Vaidya (1995). The modulus for the square array along the minimum inter-fiber distance is slightly higher than the experiment, which might be expected considering that voids were ignored in this particular analysis. The transverse Poisson's ratio was not predicted very well by any of the three models. As with the present results, Foye (1966) also found that a square array under-predicted ν_{23} of a glass/epoxy composite at comparable fiber volume fractions. Since modeling of the transverse modulus is given greater importance than transverse Poisson's ratio in the overall investigation, the model in Figure 13 (b) was selected for use in the remainder of the investigation.

Table 9. Predictions of E_2 and ν_{23} of the G100 composite based on different fiber packing arrays, neglecting voids.

	E_2 (GPa) (Difference[1])	ν_{23} (Difference[1])
Experimental	29.0	0.32
Hexagonal array	20.4 (-42.2)	0.38 (18.7)
Square array (min. fiber distance)	31.6 (9.0)	0.24 (-25.0)
Square array (max. fiber distance)	19.1 (-34.1)	0.51 (59.4)

[1] $Difference = \frac{FEA-Exp}{Exp} \cdot 100\ \%$

Modeling approach for voids

Three different approaches for modeling the effect of voids on transverse properties were compared using the G100 composite as a case study. In each case, uniaxial stress in the 2-direction

is imposed on the model. Approach 1, shown in Figure 14 (a), homogenizes the voids in the matrix according to the GSCM discussed earlier, with the fraction of voids in the composite, v_v, taken as 0.02 and the fraction of voids in the matrix, v_{vm}, taken as 0.091 according to Table 7. The effective matrix properties for the G100 composite according to the GSCM are given in Table 11.

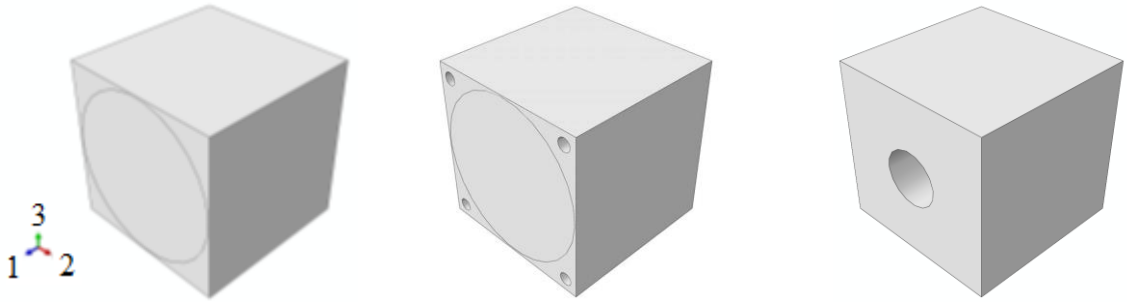

(a) (b) (c)

Figure 14. RUCs including the effects of voids: (a) Approach 1, fiber and homogenized effective matrix; (b) Approach 2, fiber, matrix, and discrete voids; (c) Approach 3 (first step), determination of effective matrix properties from FEA of matrix with discrete voids.

Table 10. Matrix properties from GSCM used for various preliminary empirical and finite element models.

Model	E_{1m}^{eff} (GPa)	E_{2m}^{eff} (GPa)	ν_{12m}^{eff}	ν_{23m}^{eff}	G_{12m}^{eff} (GPa)	K_{23m}^{eff} (GPa)
C100	2.66	2.07	0.38	0.385	0.88	2.65
C75G25	2.78	2.33	0.38	0.385	0.95	3.11
C50G50	2.79	2.35	0.38	0.385	0.96	3.16
C25G75	2.71	2.18	0.38	0.384	0.91	2.84
G100	2.79	2.35	0.38	0.384	0.96	3.15

Approach 2 assumes one discrete cylindrical void in each of the four corners of the RUC, midway between the fiber and the corner, as shown in Figure 14 (b). Void fractions v_v and v_{vm} have the same values as in Approach 1, and the matrix is modelled as fully dense, isotropic resin as indicated in Table 5 and Table 6. Four smaller holes with their centroids at the mid-position

between the fibers and the corner were also modelled as a variant of Approach 2, but were found to give the same results as one hole in each corner and the model and the results are discussed in Appendix F.

Approach 3 is essentially a check on Approach 1 in that FEA, rather than GSCM, is used to determine the effective properties of the matrix with cylindrical voids Figure 14 (c) shows the RUC for the first step of this approach, where a single cylindrical void is modelled in fully dense, isotropic matrix with properties as given in Table 5 and Table 6. Periodicity conditions in Table 2 were applied to RUC in order to obtain all the constitutive properties an RUC of an isotropic matrix with single cylindrical void. The next step applies the resulting effective matrix properties to the same RUC configuration as was used in Approach 1 (Figure 14 (a)) to determine the transverse properties of the composite.

The transverse properties of G100 resulting from the three void modeling approaches are summarized in Table 11. Approaches 1 and 3, which homogenize the matrix with cylindrical voids according to GSCM and FEA, respectively, both predict E_2 values considerably less than the experimental E_2. FEA therefore confirms the GSCM model for the effective matrix properties. Approach 2 with discrete voids in the corners of the RUC over-predicts E_2 by only 1.5 GPa (~5%). It is believed that Approaches 1 and 3 under-estimate E_2 because the matrix material in the critical region along the shortest path between adjacent fibers is excessively softened due to homogenization. The contour plot of 2-direction stress in Figure 15 and Figure 17 show that the 2-direction elemental stresses in the region where adjacent fibers nearly touch each other in Approach 1 are lower than in Approach 2. Also, the contour plot of 2-direction displacements in Figure 16 and Figure 18 show that the 2-direction elemental displacements in the region where adjacent fibers nearly tough each other between the fibers and matrix in the 2-direction in

Approach 1 are relatively higher than in Approach 2, respectively. This conformed that the critical region between along the shortest path between adjacent fibers is excessively softened. Approach 2 was chosen for subsequent modeling since it predicts E_2 closest to the experimental data.

Table 11. Predictions of E_2 and ν_{23} of the G100 composite based on different approaches for modeling voids.

	E_2 (GPa) (Difference[1])	ν_{23} (Difference[1])
Experimental	29.0	0.32
Approach 1	25.1 (-13.4)	0.22 (-31.2)
Approach 2	30.5 (5.2)	0.20 (-37.5)
Approach 3	25.3 (-12.8)	0.21 (-34.4)

[1] $Difference(\%) = \frac{FEA-Exp}{Exp} \cdot 100\ \%$

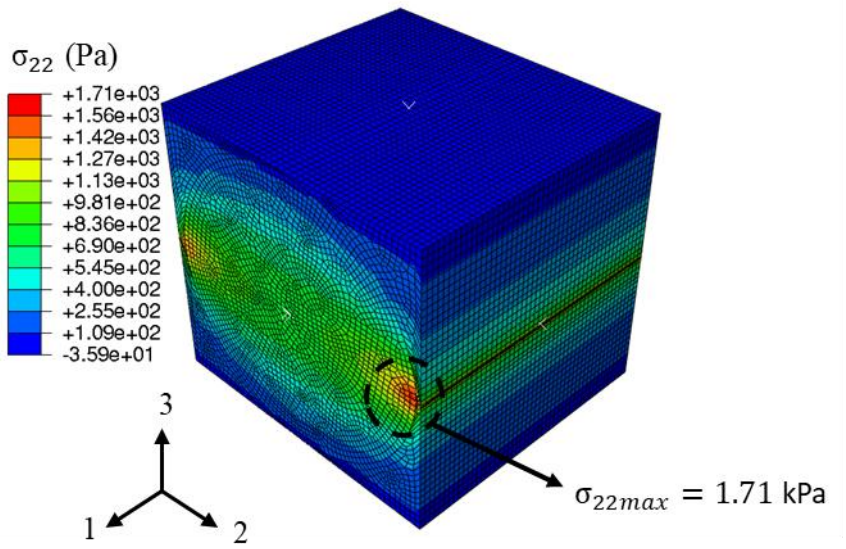

Figure 15. Contour of 2-direction stress for void modeling Approach 1—fiber and homogenized effective matrix ($\bar{\sigma}_{22}$ = 500 Pa)

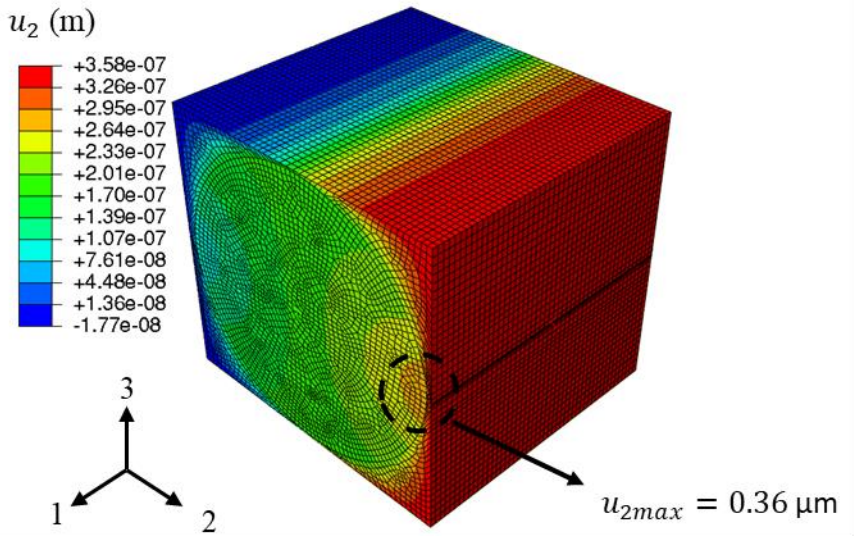

Figure 16. Contour of 2-direction displacement for void modeling Approach1—fiber and homogenized effective matrix ($\bar{\sigma}_{22}$ = 500 Pa)

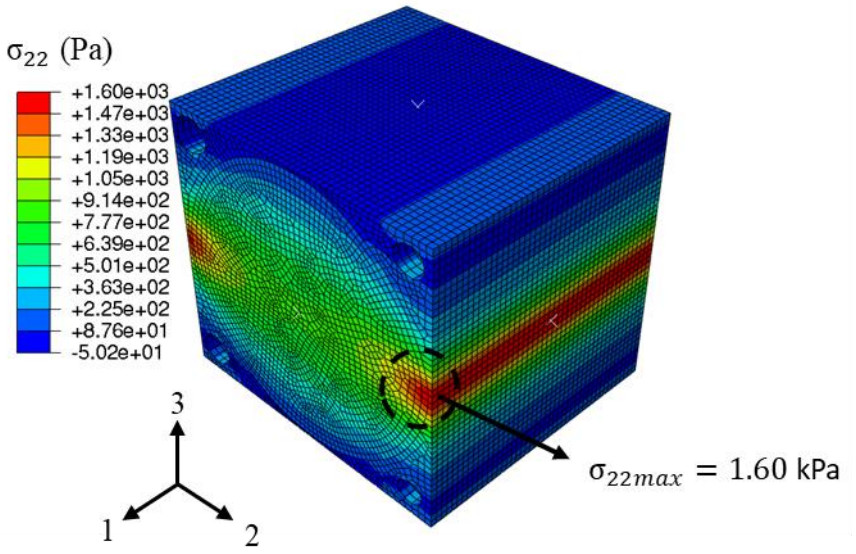

Figure 17. Contour of 2-direction stress for void modeling Approach 2—fiber, matrix, and discrete voids ($\bar{\sigma}_{22}$ = 500 Pa)

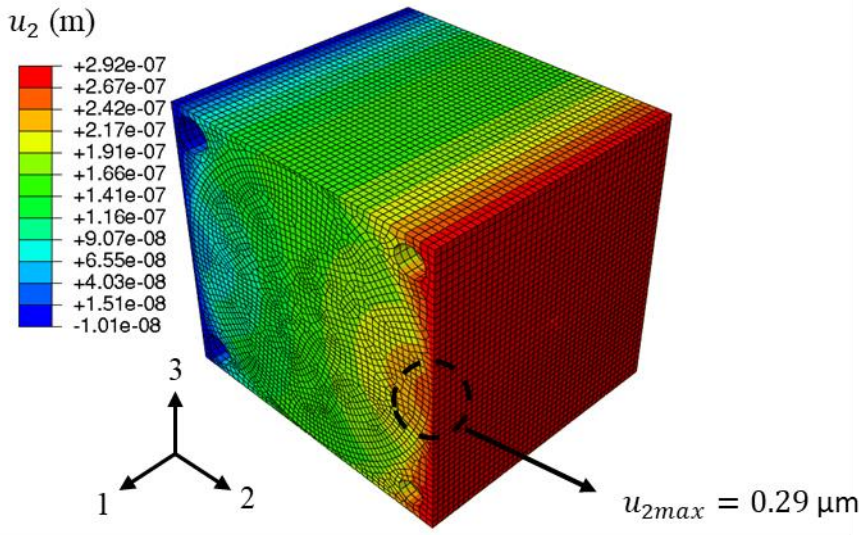

Figure 18. Contour of 2-direction displacement for Approach 2, fiber, matrix, and discrete voids ($\bar{\sigma}_{22}$ = 500 Pa)

Transverse elastic properties of ASD4 carbon fibers

Measuring the transverse elastic properties of carbon fibers is practically impossible, however, these properties can be backed out using the experimental data for C100 (Table 5 and Table 6) and the validated FEA approach. It was shown earlier that modeling discrete voids in the corners of the RUC (Figure 14 (b)) gave the best agreement with G100 experimental data, hence this same modeling approach was taken for backing out the transverse elastic properties of AS4D fibers based on consideration of the C100 experimental data, with the constituent volume fractions as listed in Table 7 and matrix properties listed in Table 5 and Table 6.

The transverse Poisson's ratio (ν_{23c}) and transverse Young's modulus (E_{2c}) of AS4D fiber were systematically varied from 0.5 to 0.9 and 24.3 GPa to 25.5 GPa, respectively while ν_{23} and E_2 of the composite were determined by FEA. From Figure 19, we can observe that ν_{23c} varies linearly with ν_{23} and does not vary significantly with E_{2c}. Subsequently the measured value of ν_{23}

of 0.49 for C100 was substituted into the equation in Figure 19, and the corresponding best value of ν_{23c} was found to be 0.85. Using this value of ν_{23c} and the measured E_2 of 11.5 GPa, the best value of E_{2c} was found to be 25.3 GPa from the equation in Figure 20. The entire data set of E_{2c} and ν_{23} for the parametric study are given in Appendix G.

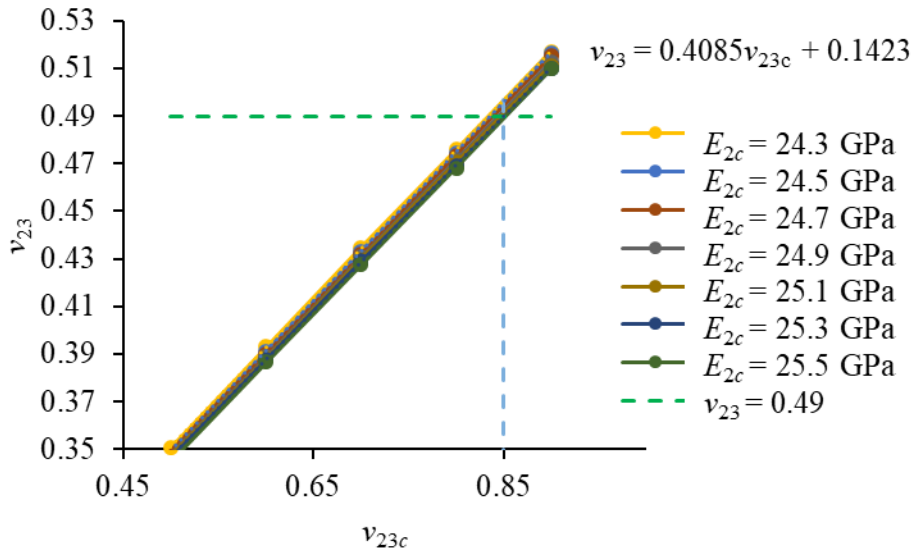

Figure 19. Backed-out transverse Poisson's ratio of carbon fiber as a function of the transverse Poisson's ratio of the C100 composite and the transverse Young's modulus of AS4D fiber.

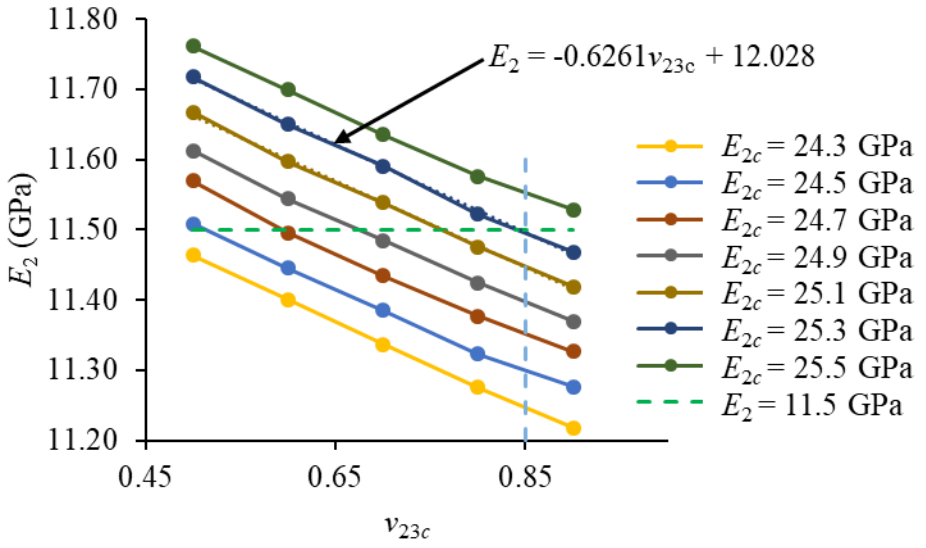

Figure 20. Backed-out transverse Young's modulus of AS4D fiber as a function of the transverse Young's modulus of the C100 composite and transverse Poisson's ratio of AS4D fiber.

Sun and Vaidya (1996), King et al. (1992), Gipple and Hoyns (1994), Cairns and Adams (1981) and Grimes et al. (1980), back-calculated values of v_{23c} = 0.25 for standard-modulus carbon fibers using FEA and experimental data; however, their analyses did not consider void content. The AS4D fiber properties obtained in the present investigation, summarized in Table 12, satisfy all the thermodynamic constraints for positive-definite stress-strain relationships (Jones, 1975), as detailed in Appendix H. Therefore, we can proceed with confidence to analyze hybrid composites with these material properties.

Table 12. Table of elastic properties of AS4D fiber.

	E_{1c} (GPa)	E_{2c} (GPa)	v_{12c}	v_{23c}
Elastic constants	245	25.3	0.2	0.85

Convergence

A convergence study was conducted by varying the model mesh size and observing the transverse Young's modulus,E_2, and transverse Poisson's ratio,ν_{23}, of the G100 and C100 materials for signs of convergence. Table 13 and Table 14 summarize the results of the mesh sensitivity study for G100 and C100 composites, respectively, including explicit voids. Percent change is computed using the difference between results of the current and previous (coarser) mesh divided by results of previous mesh.

Table 13. FE mesh sensitivity analysis for G100 composite.

Number of elements	E_2 (GPa)	Change (%)	ν_{23}	Change (%)
21,975	30.71	-	0.21	-
35,640	30.72	0.03	0.21	0.00
57,330	31.12	1.28	0.22	4.54
69,502	30.48	-2.10	0.20	-10.0
99,502	31.83	4.24	0.25	20.0
113,940	30.46	-4.50	0.20	-25.0
148,127	30.45	-0.03	0.20	0.00
190,620	30.45	0.00	0.20	0.00
233,392	30.44	-0.03	0.20	0.00
286,998	30.44	0.00	0.20	0.00
322,240	30.43	-0.03	0.20	0.00

Table 14. FE mesh sensitivity analysis for C100 composite.

Number of elements	E_2 (GPa)	Change (%)	ν_{23}	Change (%)
13,083	11.63	-	0.50	-
23,946	11.56	-0.61	0.50	0.00
39,494	11.53	-0.26	0.49	-2.04
48,411	11.53	0.00	0.49	0.00
61,488	11.53	0.00	0.49	0.00
78,640	11.51	-0.17	0.49	0.00
114,480	11.50	-0.08	0.49	0.00
133,488	11.50	0.00	0.49	0.00
171,288	11.50	0.00	0.49	0.00
197,670	11.49	-0.09	0.49	0.00
272,548	11.49	0.00	0.49	0.00
323,310	11.49	0.00	0.49	0.00

The results do not appear to be converging in the classical sense for G100 from 21,975 to 99,502 elements because of the discontinuous material properties in the model, which give rise to singularities in some stress components at the material interfaces. It can be seen that E_2, for example, oscillates within this region. Since the changes between the solutions are not large after this region, 148,127 and 171,288 elements for G100 and C100 models, respectively, were selected and the resulting "converged" transverse properties are compared with the experimental data in Table 13 and Table 14. The C100 results are in perfect agreement because of the way the AS4D transverse properties were back-calculated using the experimental data for E_2 and ν_{23}. No such "fitting" procedure was done for the G100 model, however, and the model and data modulus still agree within 5%. The converged mesh densities were used subsequently to model hybrid composites.

Table 15. Comparison of transverse properties of C100 and G100 from experiments and FEA using converged meshes.

	Experimental E_2 (GPa)	Experimental ν_{23}	FEA E_2 (GPa) (Difference[1])	FEA ν_{23} (Difference[1])
C100	11.5	0.49	11.5 (0.0)	0.49 (0.0)
G100	29.0	0.32	30.5 (5.2)	0.20 (-37.5)

[1] $Difference(\%) = \frac{FEA-Exp}{Exp} \cdot 100\ \%$

Transverse elastic properties of hybrid composites

Three hybrid models were constructed with varying compositions of carbon and glass fibers (C25G75 – 25% carbon and 75% glass, C50G50 – 50% carbon and 50% glass, C75G25 – 75% carbon and 25% glass) based on the constituent volume fractions from Table 7. The RUC of each hybrid model is illustrated in Figure 21 (a)-(d). The radius of glass fiber was taken to be 8.5 μm (PPG, Pittsburgh, PA, USA). The carbon fiber radius and, the dimensions of the square RUC in 2- and 3-direction were computed according to the constituent volume fraction data in Table 7. In the hybrid RUCs, the length in the 1-direction was one-fourth of the length in 2- and 3-direction in order to reduce computational cost (Table 16). Each fiber was positioned in the RUC in such a way that its centroidal axis coincides with the centroidal axis of each quadrant in the RUC. These RUCs are approximations of the actual microstructure of the hybrids shown in Figure 9. Periodicity conditions presented in Table 2 were applied onto the hybrid RUCs. The contour plots of stresses and displacements of C75G25 RUC can be found in Appendix I.

Although the C50G50 model was constructed based on the material constituent data, careful attention should be given to the positioning of the glass and carbon fibers in the composite micro-structure. In order to investigate if the fiber positioning has any influence on the finite

element modeling of C50G50, RUCs with fibers (a) arranged symmetric and (b) arranged anti-symmetric about a plane that is rotated +/-45 degrees about the 1-axis through the center of the RUC and the voids positioned at the mid-point between the fiber and corner, were developed. These models are shown in Figure 21 (b) and (c). Applying periodic boundary conditions on these models revealed that only the symmetric C50G50 model preserved the same Young's modulus in the 2- and 3-directions. Moreover, the stress partitioning parameters, η_c and η_g, defined as ratio of stresses in fibers to matrix retained the same value when load is applied in either transverse direction. Therefore, this model is chosen to simulate the C50G50 composite. The details of this analysis are reported in Appendix J.

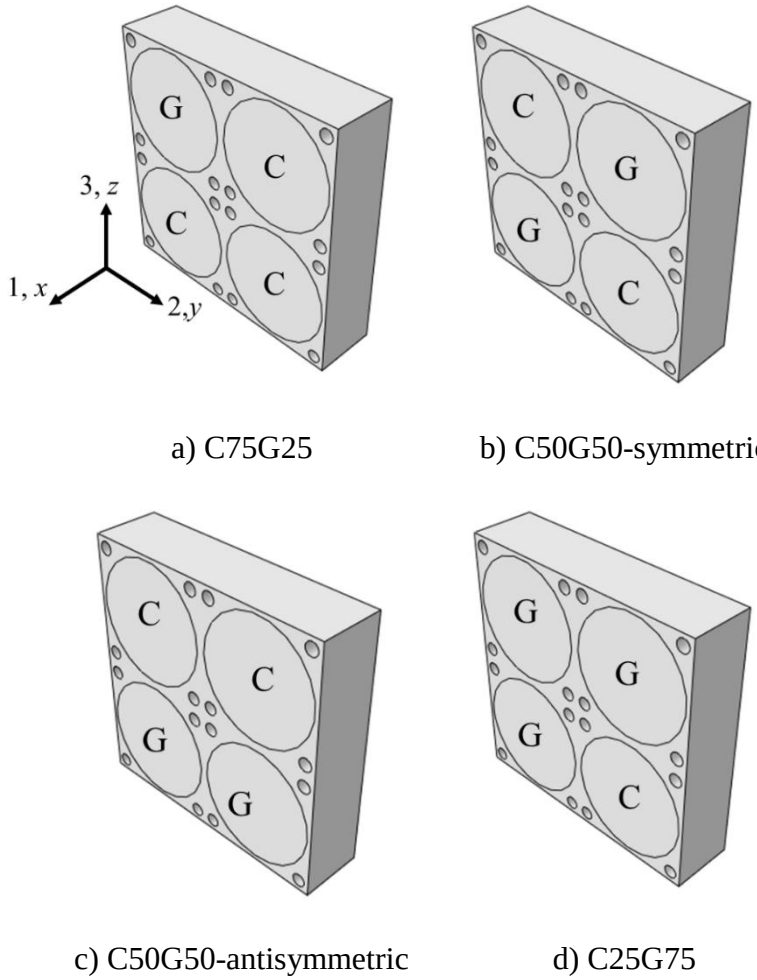

a) C75G25 b) C50G50-symmetric

c) C50G50-antisymmetric d) C25G75

Figure 21. RUC with various for various hybrids (C = carbon fiber; G = glass fiber)

Table 16. Dimensions of hybrid RUCs used for FEA.

Property	C75G25	C50G50[1]	C25G75
Length, a_x (μm)	9.0	9.05	9.05
Breadth, a_y (μm)	36.0	36.2	36.2
Height, a_z (μm)	36.0	36.2	36.2
Carbon fiber radius, R_c (μm)	8.5	8.5	8.58
Glass fiber radius, R_g (μm)	8.6	8.6	8.5
Void radius, R_v (μm)	0.8	0.58	0.92

[1]both symmetric and anti-symmetric RUCs have the same dimensions

E_2 and ν_{23} are computed using the boundary conditions in Table 2 and compared with available experimental data (Table 5 and Table 6, Figure 22). The correlation between experimental data and models was measured with the coefficient of determination (Wikipedia, 2013), R^2, given by (28-31),

$$\bar{y} = \frac{1}{n}\sum_{i=1}^{n} y_i \tag{28}$$

$$SS_{res} = \sum_{i=1}^{n} (y_i - f_i)^2 \tag{29}$$

$$SS_{tot} = \sum_{i=1}^{n} (y_i - \bar{y})^2 \tag{30}$$

$$R^2 = 1 - \frac{SS_{res}}{SS_{tot}} \tag{31}$$

where,

n: number of samples

y_i: value of sample i

$\bar{y}$: average value of samples y_i

f_i: experimental value corresponding to i

In general, good agreement is observed between the FE model and experimental transverse Young's modulus with a maximum difference of -11.2% (C50G50) and R^2 = 0.95. The transverse stiffness of all-glass composite was clearly greater than all-carbon and the hybrid composites. The

transverse Poisson's ratio has R^2 = 0.89. The ν_{23} of G100 RUC under-predicts the experimental ν_{23} by 37.5%. This is because the square array was chosen as the preliminary finite element model based on the agreement between the transverse Young's modulus obtained from FEA and experiment. Foye (1966) also found that a square array under-predicted ν_{23} of a glass/epoxy composite at comparable fiber volume fractions.

Table 17. Comparison between experimental and FEA transverse properties for all composites.

	Experimental		FEA	
	E_2 (GPa)	ν_{23}	E_2 (GPa) (Difference[1])	ν_{23} (Difference[1])
C100	11.5	0.49	11.5 (0.0)	0.49 (0.0)
C75G25	13.7	0.41	14.2 (3.7)	0.46 (12.2)
C50G50	17.8	0.43	15.8 (-11.2)	0.44 (2.3)
C25G75	19.9	0.42	18.1 (-9.1)	0.28 (-33.3)
G100	29	0.32	30.45 (5.0)	0.2 (-37.5)
R^2	-	-	0.948	0.89

[1] $Difference(\%) = \frac{FEA-Exp}{Exp} \cdot 100\ \%$

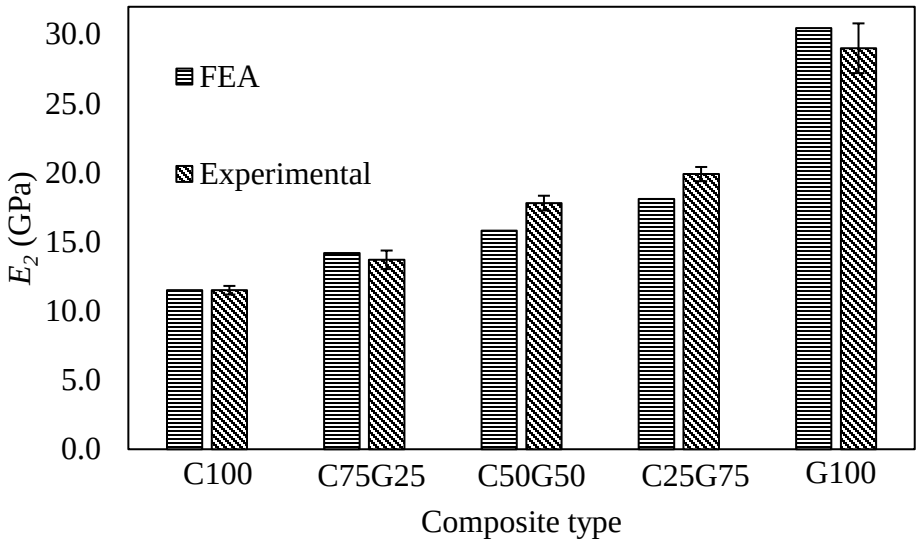

Figure 22. Comparison of transverse Young's modulus from FEA and corrected experimental values from Ripepi (2013). Error bars represent one standard deviation.

Stress partitioning parameters

Stress partitioning parameters ($\eta_{\sigma c}$ and $\eta_{\sigma g}$) (SPPs) can be used as an index to understand the behavior or materials. In order to validate the finite element modeling for SPPs, the volume average of stresses in the 1-direction and 3-direction were computed. These stresses have a zero magnitude since the boundary conditions for this case since it simulates a uniaxial tensile loading. Therefore the volume average of the lateral stresses are zero. This validation is given in detail in Appendix K.

For the composites manufactured by Ripepi (2013), $\eta_{\sigma g}$ is greater than η_c for G100, C25G75 and C75G25 models (Table 18). For the first two models, the volume fraction of the stiffer fibers (glass), is higher than the softer fibers (carbon). Therefore, most of the load is carried by the glass fibers. In C50G50 model, $\eta_{\sigma g}$ lower than any other hybrid model because the void

volume fraction (v_v = 0.013) is the lowest and the volume fraction of matrix (v_m = 0.289) is highest, of all the hybrid models. Therefore the matrix is stiffer and also more stress is distributed to the matrix than in other models.

Table 18. Stress partitioning parameters of the manufactured composites, obtained by FEA

	Stress partitioning parameters	
Model	$\eta_{\sigma c}$	$\eta_{\sigma g}$
C100	1.84	-
C75G25	1.61	1.80
C50G50	1.70	1.67
C25G75	1.69	2.03
G100	-	3.15

Load sharing mechanism among constituents in hybrid composites

In an effort to further to understand the load sharing mechanism by the fibers in composites with variable ratios of carbon and glass fibers, without the complications of slightly variable overall fiber, matrix, and void contents as seen in the manufactured materials, a series of FE models were evaluated using a fixed overall fiber volume fraction of 0.7 and no voids. Otherwise, the matrix properties are listed in Table 5 and Table 6; the carbon fiber properties are in Table 12; and the glass fiber is taken to have an elastic modulus (E_g) of 80.0 GPa and a Poisson's ratio (v_g) of 0.26. The synthesized RUCs were analyzed for (a) stress partitioning parameters (b) strain partitioning parameters (EPP) and (c) strain energy density partitioning parameters (SEDPP). Respectively, these RUCs were subjected to (a) the same uniaxial unit stress in the 2-direction, (b) different uniaxial stresses in the 2-direction so that all materials have a unit strain in the 2-direction

and (c) different uniaxial stresses in the 2-direction so that a unit of work is applied to the RUC for all materials.

The SPP was computed in the usual way as presented in equations (12) and (13). However, EPP was computed by taking the ratio of volume average of 2-direction strain in the fiber to the volume average of 2-direction strain in the matrix. Similarly SEDPP was computed by taking the volume average of 2-direction strain energy density in the fiber to the volume average of 2-direction strain energy density in the matrix.

To compute the SPP and EPP, periodicity conditions presented in equation (14) were applied on to the RUC by taking $\bar{\varepsilon}_{22}$ as unity. In order to simulate the SEDPP, the same periodicity conditions in equation (14) were applied on to the RUC and the value of $\bar{\varepsilon}_{22}$ can be obtained by first considering the volumetric average of strain energy density, $\bar{\psi}$, for uniaxial stress in the 2-direction,

$$\bar{\psi} = \frac{1}{2}\bar{\sigma}_{22}\bar{\varepsilon}_{22} \tag{32}$$

which can be expressed in terms of the 2-drection modulus and strain as,

$$\bar{\psi} = \frac{1}{2}E_2(\bar{\varepsilon}_{22})^2 \tag{33}$$

For a unit value for $\bar{\psi}$, the expression for $\bar{\varepsilon}_{22}$ is then

$$\bar{\varepsilon}_{22} = \sqrt{2/E_2} \tag{34}$$

The SPPs, EPPs ($\eta_{\varepsilon c}$ and $\eta_{\varepsilon g}$) and SEDPPs ($\eta_{\psi c}$ and $\eta_{\psi g}$) computed from FEA are presented in Table 19. The SPPs results show that $\eta_{\sigma c}$ is nearly the same in the C100, C75G25, C25G75 and G100 models. In C50G50 model, $\eta_{\sigma c}$ is equal to $\eta_{\sigma g}$. $\eta_{\sigma g}$ is the highest for G100

composite and lowest in C25G75 model. The $\eta_{\varepsilon c}$ in C50G50 model is the highest. This can be due to the excessive deformation in carbon fibers when overly stiff glass fibers are placed adjacent to the carbon fibers. Similarly, $\eta_{\psi c}$ in C50G50 model is the highest.

In order to compare the stress state of each constituent in the all-carbon, all-glass and hybrid RUCs, the volume average of 2-direction stresses in the constituents were normalized with respect to the volume average of 2-direction stress of the entire RUC, Table 20. The strain-state and energy-state in each of the constituents are presented in Table 21 and Table 22, respectively. The results in Table 20 show that the 2-direction stresses in the matrix decrease when the glass-to-carbon fiber ratio in the composite is increased. This behavior is similar to springs attached in parallel. When stiffer springs are progressively added to a system the overall stress in the softer spring progressively decreases. The results in Table 22 show that the 2-direction strains in matrix increase when glass-to-carbon fiber ratio in the composite is increased. This behavior can be modeled as springs attached in series. The deformation in the softer spring is more when stiffer springs are progressively added to the system. In C50G50 model the stress levels (Table 21) in carbon and glass fibers are the same, but the strains in carbon fibers are 3.3 times higher than glass fibers (Table 22). This is because the transverse modulus in the glass fiber, E_{2g} = 80 GPa, is 3.2 times higher than the transverse modulus of carbon fibers, E_{2c} = 25.3 GPa. The results from Table 22 show that the strain energy density in matrix is always greater than carbon fibers followed by glass fibers for any combination of glass-to-carbon fiber ratio.

Table 19. Stress partitioning (SPP) vs. strain partitioning (EPP) vs. strain energy density parameter (SEDPP) for synthesized composites with an overall fiber volume fraction of 0.7 and no voids.

	Carbon SPP, $\eta_{\sigma c}$	Glass SPP, $\eta_{\sigma g}$	Carbon EPP, $\eta_{\varepsilon c}$	Glass EPP, $\eta_{\varepsilon g}$	Carbon SEDPP, $\eta_{\psi c}$	Glass SEDPP, $\eta_{\psi g}$
C100	1.81	-	0.33	-	0.57	-
C75G25	1.82	2.17	0.33	0.12	0.53	0.24
C50G50	1.99	1.98	0.38	0.11	0.67	0.19
C75G25	1.79	2.05	0.31	0.20	0.41	0.30
G100	-	2.33	-	0.14	-	0.25

Table 20. Volume-averaged transverse stresses in the constituents under uniaxial transverse stress, normalized by the transverse stress, for synthesized composites with an overall fiber volume fraction of 0.7 and no voids.

	$\bar{\sigma}_{22c}$	$\bar{\sigma}_{22g}$	$\bar{\sigma}_{22m}$
C100	1.16	-	0.64
C75G25	1.11	1.33	0.61
C50G50	1.18	1.17	0.59
C25G75	0.99	1.13	0.55
G100	-	1.20	0.51

Table 21. Volume-averaged transverse strains in the constituents under unit transverse strain, for synthesized composites with an overall fiber volume fraction of 0.7 and no voids.

	$\bar{\varepsilon}_{22c}$	$\bar{\varepsilon}_{22g}$	$\bar{\varepsilon}_{22m}$
C100	0.62	-	1.88
C75G25	0.67	0.25	2.02
C50G50	0.80	0.24	2.12
C25G75	0.74	0.46	2.34
G100	-	0.36	2.50

Table 22. Strain energy density in the constituents under unit work, for synthesized composites with an overall fiber volume fraction of 0.7 and no voids.

	Volume averaged strain energy density in carbon fiber	Volume averaged strain energy density in glass fiber	Volume averaged strain energy density in matrix
	$\bar{\psi}_{22c}$	$\bar{\psi}_{22g}$	$\bar{\psi}_{22m}$
C100	0.82	-	1.44
C75G25	0.86	0.39	1.62
C50G50	1.13	0.31	1.67
C25G75	0.81	0.59	1.99
G100	-	0.53	2.11

Analysis of closed-form micromechanical models

Iso-stress model

The results for the ISM are shown in Table 23 and Figure 23, with a best coefficient of determination (R^2) of -3.239. The properties of the matrix are obtained from Table 5 and Table 6. No curve fitting was done in this case and the negative value for R^2implies a bad estimate for elastic properties.

Table 23. Comparison between experimental and ISM E_2, of hybrid models.

	Experimental	ISM
	E_2 (GPa)	E_2 (GPa) (Difference[1])
C100	11.5	5.6 (-51.2)
C75G25	13.7	6.8 (-50.4)
C50G50	17.8	6.8 (-61.7)
C25G75	19.9	6.5 (-67.3)
G100	29	9.0 (-69.0)
R^2	-	-3.239

[1] $Difference(\%) = \frac{ISM-Exp}{Exp} \cdot 100\ \%$

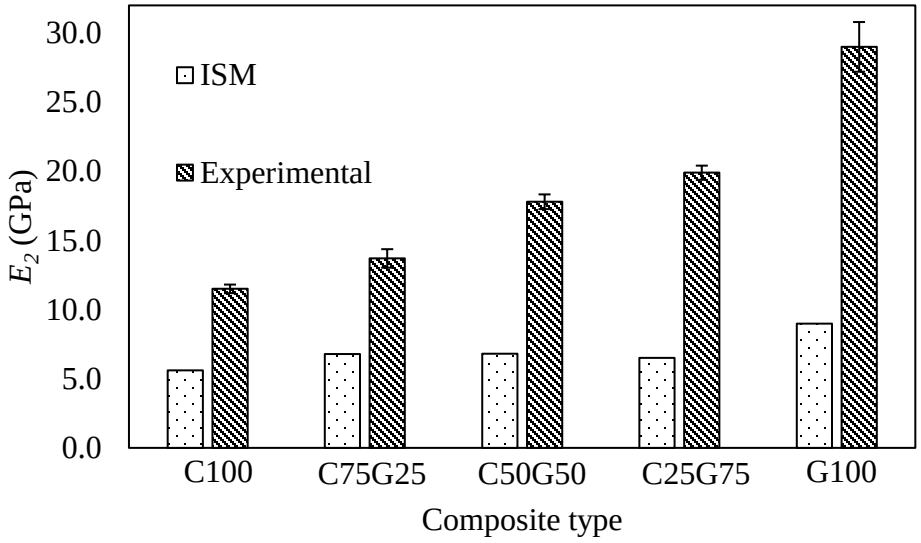

Figure 23. Transverse Young's modulus calculated from ISM and measured in experiments. Error bars represent one standard deviation.

Modified iso-stress model

Figure 24 shows all possible combinations of $\eta_{\sigma c}$ and $\eta_{\sigma g}$ for R^2 and the predicted E_2 by MISM are shown in Table 25. The properties of the matrix are obtained from Table 10.

Initially $\eta_{\sigma c}$ was set to 3.79 for C100 and $\eta_{\sigma g}$ was set to 5.59 for G100 and the overall coefficient of determination (R^2) for all the five materials was computed to be 0.97. After adjusting the $\eta_{\sigma c}$ to 3.4 and $\eta_{\sigma g}$ to 5.7, based on the data search from the surface plot, these values gave a better R^2—that is, 0.985.

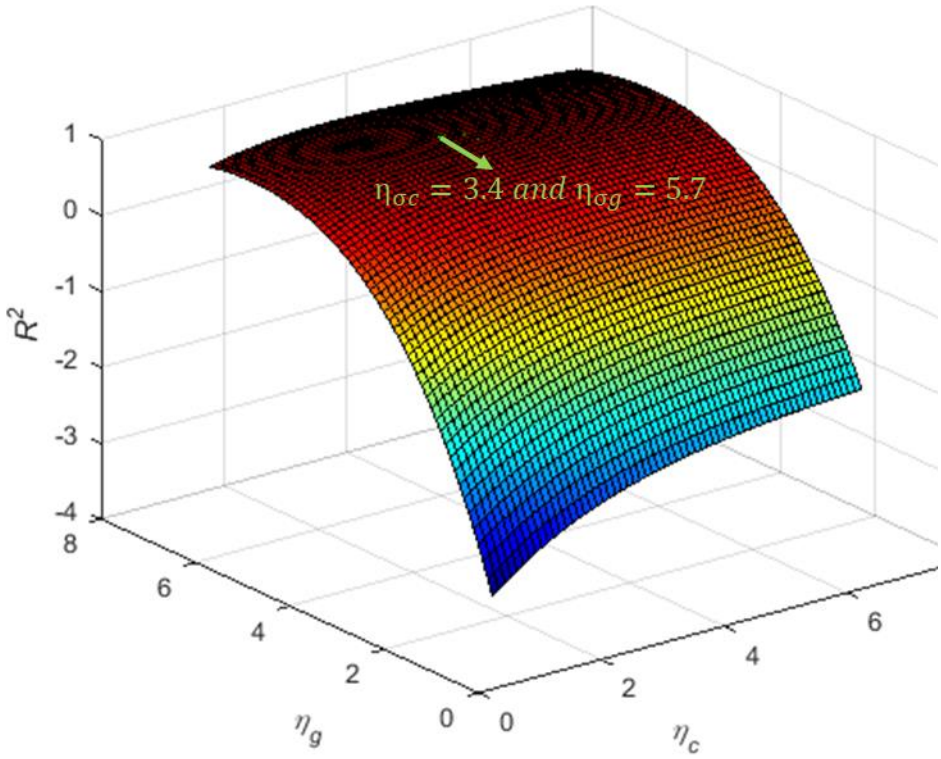

Figure 24. Surface plot for R^2 based on MISM with $\eta_{\sigma c}$ and $\eta_{\sigma g}$ as parameters.

Table 24. Comparison between experimental and MISM E_2, of hybrid models.

	Experimental	MISM
	E_2 (GPa)	E_2 (GPa) (Difference[1])
C100	11.5	10.9 (-5.3)
C75G25	13.7	14.9 (9.0)
C50G50	17.8	17.3 (-2.7)
C25G75	19.9	19.2 (-3.5)
G100	29	29.4 (1.2)
R^2	-	0.985

[1] $Difference(\%) = \frac{MISM-Exp}{Exp} \cdot 100\ \%$

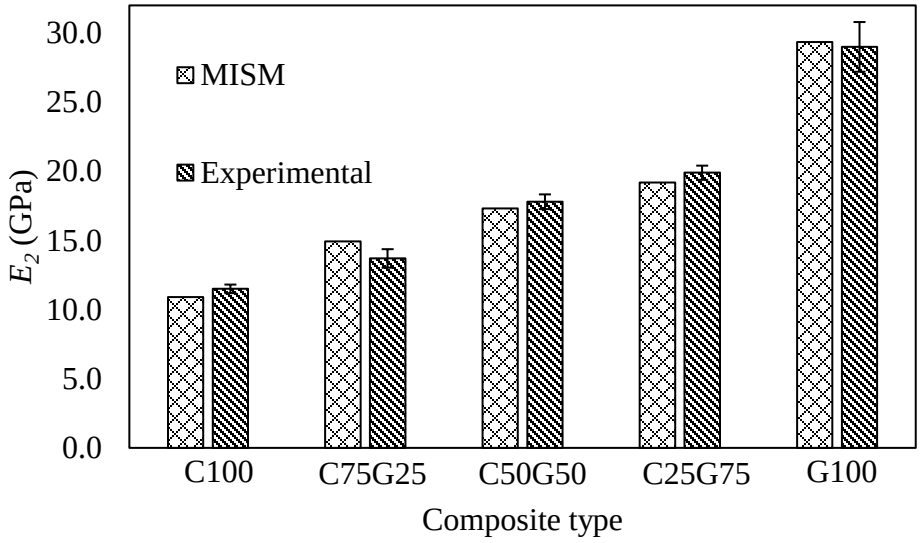

Figure 25. Transverse Young's modulus calculated from MISM and measured in experiments. Error bars represent one standard deviation.

The SPP from MISM are higher than the values from FEA ($\eta_{\sigma c}$ = 1.8 and $\eta_{\sigma g}$ = 3.2). This discrepancy is hypothesized to be due to the use relatively soft effective matrix properties to account for voids implicitly in the MISM, thus leading to higher SPPs required to

match the experimental E_2 values. To test this hypothesis, the FEA of G100 composite was re-run with effective matrix properties as given in Table 10**;** and the stress partitioning parameters were computed according to the equations in (12) and (13). The E_2 and $\eta_{\sigma g}$ computed from this case were 25.1 GPa and 2.96 respectively. This confirmed that MISM requires higher SPP to match the experimental E_2 values.

Modified Halpin-Tsai model

Table 25, Figure 26 and Figure 27 show the results of MHTM by substituting the matrix properties from Table 10; and fiber modulus into equations (26)-(28). Considering all 5 materials, the R^2 is 0.97, and the best-fit value of ξ is 5.5. This value for ξ is higher than the value obtained by Banerjee and Sankar (2012) (ξ = 1.14) since the matrix is softened by voids.

Table 25. Comparison between experimental and MHTM E_2, of hybrid models.

	Experimental	MHSM
	E_2 (GPa)	E_2 (GPa) (Difference[1])
C100	11.5	12.5 (8.3)
C75G25	13.7	15.8 (15.1)
C50G50	17.8	17.7 (0.8)
C25G75	19.9	19.3 (-2.9)
G100	29	29.0 (-0.1)
R^2	-	0.970

[1] $Difference(\%) = \frac{MHTM-Exp}{Exp} \cdot 100\ \%$

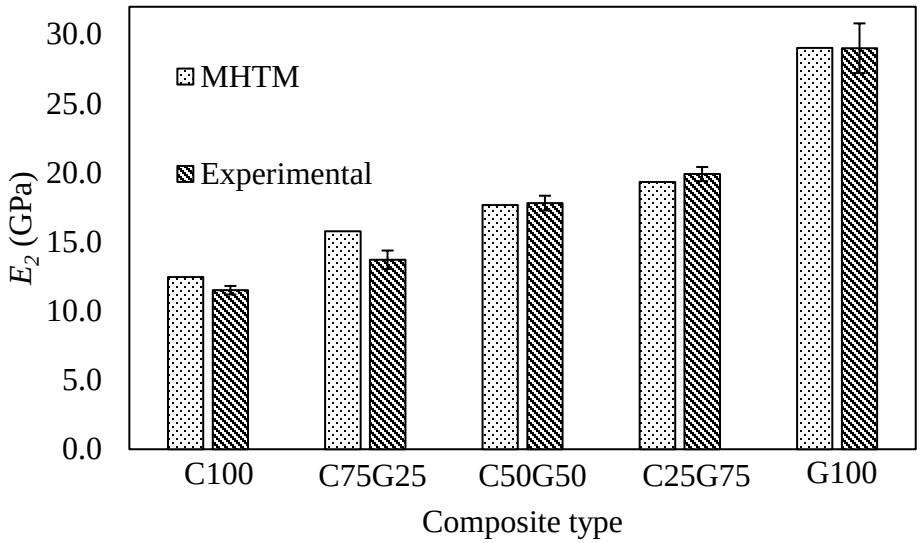

Figure 26. Transverse Young's modulus calculated from MHTM and measured in experiments. Error bars represent one standard deviation.

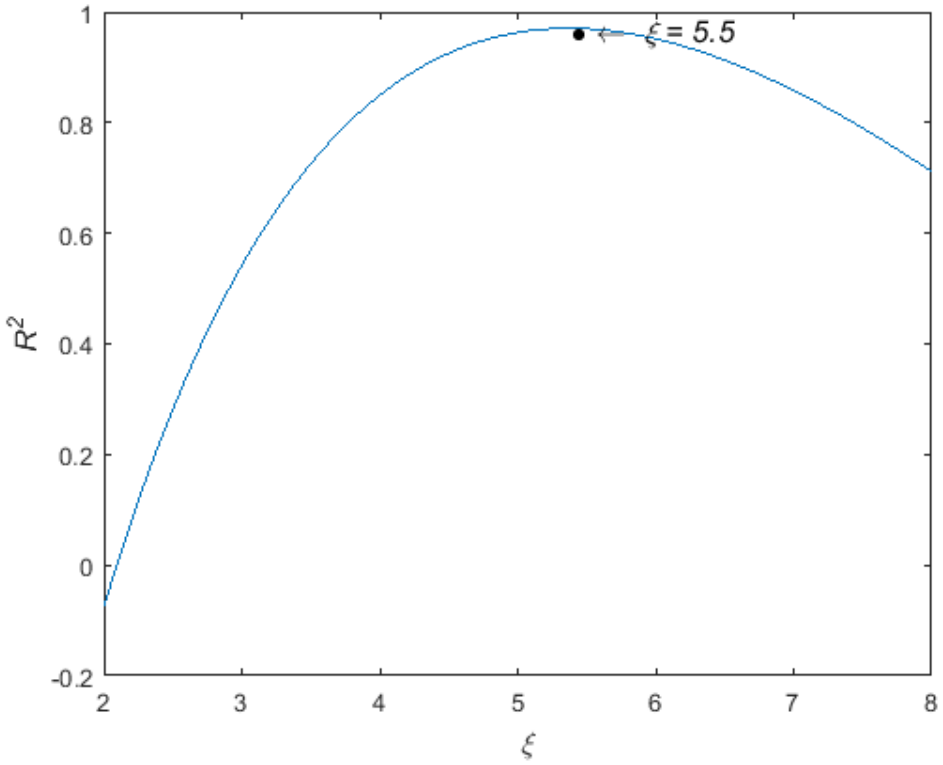

Figure 27. Coefficient of determination (R^2) as a function of ξ based on MHTM

Summary of micromechanical models

In general, an RUC model with square packing array where the fibers are positioned in minimum inter-fiber distance and voids modeled as discrete holes for all-carbon, all-glass and hybrid models have good estimates of E_2 in comparison to experimental data, Figure 28. The coefficient of determination,R^2, is equal to 0.95. Also ν_{23} of the hybrids were computed and compared with the experimental data in Table 26. The comparison showed that the ν_{23} was predicted progressively worse in composite with progressively higher proportions of glass fiber. This is due to the fact that the best FE fiber packing array was not selected to match ν_{23}. On the other hand, since the carbon fiber transverse modulus and Poisson's ratio were back-calculated to match the experimental properties of C100, the predictions of properties of composite with progressively higher proportions of carbon fiber were generally better.

Three closed-form models were used to model E_2 of all-carbon, all-glass and hybrid composites. Out of the three models, ISM has poorly predicts the transverse modulus with R^2 = -3.239. MISM has the best prediction of E_2 with R^2 = 0.985. MHTM has the next best prediction with R^2 = 0.97.

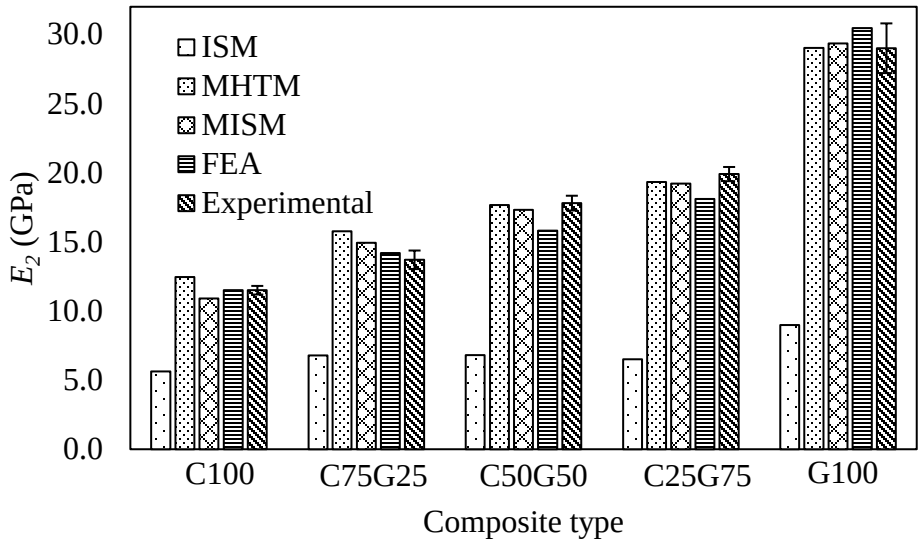

Figure 28. Transverse Young's modulus calculated from FEA, MISM, ISM, MHTM and measured in experiments. Error bars for the experimental results represent one standard deviation.

Table 26. Comparison between experimental, empirical and FEA properties of hybrid models

	Experimental		FEA		ISM	MISM	MHTM
	E_2, GPa	ν_{23}	E_2, GPa (% Difference)*	ν_{23} (% Difference)*	E_2, GPa (% Difference)*	E_2, GPa (% Difference)*	E_2, GPa (% Difference)*
C100	11.5	0.49	11.5 (0.0)	0.49 (0.0)	5.6 (-51.2)	10.9 (-5.3)	12.5 (8.3)
C75G25	13.7	0.41	14.2 (3.7)	0.46 (12.2)	6.8 (-50.4)	14.9 (9.0)	15.8 (15.1)
C50G50	17.8	0.43	15.8 (-11.2)	0.44 (2.3)	6.8 (-61.7)	17.3 (-2.7)	17.7 (0.8)
C25G75	19.9	0.42	18.1 (-9.1)	0.28 (-33.3)	6.5 (-67.3)	19.2 (-3.5)	19.3 (-2.9)
G100	29	0.32	30.45 (5.0)	0.2 (-37.5)	9.0 (-69.0)	29.4 (1.2)	29.0 (-0.1)
R^2	-		0.948	0.89	-3.239	0.985	0.970

*% Difference $= \frac{\text{Predicted}-\text{Exp}}{\text{Exp}} \cdot 100\ \%$

Chapter 5

CONCLUSIONS

In this study, the transverse Young's modulus of hybrid composites reinforced with glass and carbon fibers are simulated by applying micromechanics. The five hybrid composites that were evaluated are 100% carbon (C100), 75% carbon and 25% glass (C75G25), 50% carbon and 50% glass (C50G50), 25% carbon and 75% glass (C25G75), and 100% glass (G100). In this process, the effect of voids on composite properties were simulated explicitly as regularly spaced, discrete cylindrical holes in the matrix, and implicitly using micromechanical equations to obtain the effective (homogenized) properties of the void-containing matrix.

From the finite element analysis (FEA), it was observed that a square array of packing arrangement with voids dispersed as circular cylinders in the matrix showed good correspondence with experimental data for transverse modulus of the all-glass fiber composite. Validation of this model allowed the back-calculation of the transverse Young's modulus and transverse Poisson's ratio of AS4D carbon fiber. This exercise also allowed for the determination of best way to model voids in fiber composites—i.e., discretely rather than homogenized. When the matrix is homogenized using "generalized self-consistent model" GSCM, there is too much softening in the critical tight space between the fibers. Therefore, transverse stresses are carried more in the fibers than in the matrix. With the material properties and the best void modeling technique in hand, the transverse properties and the stress partitioning parameters (SPP) ($\eta_{\sigma g}$ and $\eta_{\sigma c}$) of the hybrid glass/carbon composites were obtained. It was observed that $\eta_{\sigma g}$ is greater than $\eta_{\sigma c}$ for G100, C25G75 and C75G25

models. This is due to the fact that the volume fraction of the stiffer fibers (glass), is higher than the softer fibers (carbon). Therefore, most of the load is carried by the glass fibers. However, in C50G50 model, the SPPs are nearly equal. In order to further investigate the load sharing mechanisms in hybrid composites under transverse loads, a series of FE models with fiber volume fraction equal to 0.7 and no voids were evaluated for the stress partitioning parameters, strain partitioning parameters ($\eta_{\varepsilon c}\ and\ \eta_{\varepsilon g}$) and strain energy density partitioning parameters ($\eta_{\psi c}\ and\ \eta_{\psi g}$). The SPPs results show that $\eta_{\sigma c}$ is nearly the same in the C100, C75G25, C25G75 and G100 models. It was observed that $\eta_{\varepsilon c}$ in C50G50 model is the highest. This could be attributed to extreme deformation in carbon fibers when relatively stiff glass fibers are placed adjacent to the carbon fiber. To obtain further insights on the load sharing mechanisms of all-carbon, all-glass and hybrid composites under transverse loads, the stress, strain and energy in each constituents were analyzed. The analysis revealed that the transverse stress in the matrix decreases when the glass-to-carbon fiber ratio increases, which is similar to springs attached in series. However the transverse strain in the matrix increases when glass-to-carbon fiber ratio increases. This behavior is very similar to springs attached in parallel.

In the FE simulation of a square array of circular fibers, careful attention should be given to the direction in which the transverse modulus is measured. Depending on the angle at which uniaxial stress is applied in the transverse plane, the measured transverse modulus can vary. When the stress is along a direction with a larger amount of matrix between adjacent fibers, the modulus is less than it is along a direction with less matrix between the fibers.

Mathematically, the modified iso-stress model (MISM) model has the best correspondence with a coefficient of determination, R^2 = 0.985. The stress partitioning

estimates (SPP) from this model ($\eta_{\sigma c}$ = 3.4 and $\eta_{\sigma g}$ = 5.7) are higher than the values obtained by Ha et al. (2012) ($\eta_{\sigma c}$ =1.48 and $\eta_{\sigma g}$= 3.78), however, voids were apparently not addressed by Ha et al. As a consequence, the matrix used by Ha et al. is stiffer and the matrix carries a larger proportion of the transverse stress. The SPP values from MISM were also greater than the SPPs from FEA in the current investigation ($\eta_{\sigma c}$ = 1.84 for C100 and $\eta_{\sigma g}$= 3.15 for G100). This discrepancy to be due to the use of relatively soft effective matrix properties to account for voids implicitly in the MISM., thus requiring higher SPPs required to match the experimental transverse Young's modulus values.

The best-fit value of ξ in the modified Halpin-Tsai model (MHTM) is 5.5 (R^2 = 0.97), which is much greater than the best-fit value obtained by Banerjee and Sankar (2012) (ξ = 1.14). Though, the transverse properties of carbon fiber was obtained from an unknown source. They used a hexagonal array of carbon/glass fibers with a combined fiber volume fraction of 60%, this array type predicts a lower E_2 for hybrid composites. Also, since they did not consider the void content in the matrix, their model predicts a lower best-fit value of ξ.

The iso-stress model (ISM), which has no fitting parameters, consistently and significantly under-predicted the experiments and did not show agreement with even the non-hybrid composites. This result can be expected because the iso-stress assumption provides a lower bound on stiffness according to micromechanics theory.

REFERENCES

Adams, D. F. and Doner, D. R. 1967 "Transverse normal loading of a unidirectional composite," *Journal of Composite Materials*, 1, 152-164.

Arvin, A.C., and Bakis, C.E., 2006. "Optimal design of press-fitted filament wound composite flywheel rotors," *Composite Structures*, 72:47-57.

ASTM D3171-09, Standard Test Methods for Constituent Content of Composite Materials, ASTM International, West Conshohocken, PA, 2009

Banerjee, S., and Sankar, B., 2012. "Mechanical Properties of Hybrid Composites Using Finite Element Method Based Micromechanics," *Proc. 27th Annual Technical Conference of the American Society for Composites*, DEStech, Lancaster, PA.

Bakis, C.E., Nanni, A., Terosky, J.A., and Koehler, S.W., 2001. "Self-monitoring, pseudo-ductile, hybrid FRP reinforced rods for concrete applications," *Composites Science and Technology*, 61:815-823.

Bakis, C.E, Ripepi, M. J., 2015. "Transverse Mechanical Properties of Unidirectional Hybrid Fiber Composites." Proc. *30th Technical Conference for American Society for Composites*, DEStech, Lancaster, PA.

Barbero, E.J., 2013. *Finite Element Analysis of Composite Materials using Abaqus.* Boca Raton: CRC Press, Taylor & Francis Group.

Beyle, A., Cocke, D.L., and Green A., 2014. "Models for Analysis of the Effective Properties of Hybrid Composites," *Proceedings of the American Society for Composites: Twenty-Ninth Technical Conference*, La Jolla, California, CD-ROM—20 pp.

Bunsell, A., and Harris, B., 1974. “Hybrid Carbon and Glass Fibre Composites,” *Composites*, 5(4):157-164.

Cairns, D.S., and Adams, D.F., 1981. “Moisture and Thermal Expansion of Composite Materials,” Interim Report, University of Wyoming, Laramie, Wyoming.

Christensen, R. M., 1993.”Effective Properties of Composite Materials Containing Voids,” *Proceedings: Mathematical and Physical Sciences*, 440(1909):461-473.

Cole, D.P., Gardea, F., Henry, C.T., and Haynes, R., 2016. “Damage Precursors in Individual Microfibers,” *Proceedings of the ASME 2016 Conference on Smart Materials: Adaptive Structures and Intelligent Systems,* New York: American Society of Mechanical Engineers.

Daniel, I., and Ishai, O. 2006. *Engineering Mechanics of Composite Materials*. New York: Oxford University Press.

Daniel, I.M., and Lee, J.W. 1990. “Progressive Transverse Cracking of Crossply Composite Laminates,” *Journal of Composite Materials,* 24:1225-1243.

Drago, A., and Pindera, M.J., 2007. “Micro-macromechanical Analysis of Heterogeneous Materials: Macroscopically Homogeneous vs Periodic Microstructures,” *Composites Science and Technology*, 67:1243-1263.

Eric, W., 2017. “Carbon and Glass Fiber Reinforcement Combine in Hybrid Long Fiber Thermoplastic Composites to Bridge Price and Performance Gap,” *Reinforced Plastics,* 61(1)

Foye, R.L., 1996. “An Evaluation of Various Engineering Estimates of the Transverse Properties of Unidirectional Composites,” *Proceedings of the 10th National SAMPE Symposium,* San Diego, CA.

Genta, G., 1985. *Kinetic Energy Storage*. London: Butterworth & Co. Ltd.

Gipple, K.L., and Hoyns, D., 1994. “Measurement of the Out-of-Plane Shear Response of Thick Section Composite Materials Using the V-Notched Beam Specimen,” *Journal of Composite Materials,* 28(6):543-572.

Goldsmith M.B., Sankar, B.V., Haftka, R.T., and Goldberg, R.K., 2013. “Quantifying the Effects of Voids in Woven Ceramic Matrix Composites,” AIAA 2013-1619, *Proc. 54th AIAA/ASME/ASCE/AHS/ASC Structures, Structural Dynamics and Materials Conference,* Reston, VA: American Institute of Aeronautics and Astronautics.

Grimes, G.C., Adams, D.F., and Dusablon, E.G., 1980. “The Effect of Discontinuities on Compression Fatigue Properties of Advanced Composites,” Final Technical Report, University of Wyoming, Laramie, Wyoming.

Gusev, A.A., Hine, P.J., and Ward, I.M., 2000. “Fiber Packing and Elastic Properties of a Transversely Random Unidirectional Glass/Epoxy Composite,” *Composites Science and Technology,* 60:535-541. Ha, S., Kim, S., Nasir, S., and Han, S., 2012. “Design Optimization and Fabrication of a Hybrid Composite Flywheel Rotor,” *Composite Structures,* 94:3290-3299.

Halpin, J., and Kardos, J., 1976. “The Halpin-Tsai Equations: A Review,” *Polymer Engineering and Science,* 16(5):344-352.

Hashin, Z., and Shtrikman, S., 1963. “A Variational Approach to the Theory of the Elastic Behaviour of Multiphase Materials,” *J. Mech. Phys. Solids,* 11:127-140.

Hexcel HexTow AS4D Data Sheet. 2013. Hexcel Corporation. Stamford. Connecticut.

Hollister, S.J., and Kikuchi, N., 1992. “A Comparison of Homogenization and Standard Mechanics Analysis for Periodic Porous Composites,” *Computational Mechanics,* 10:73-95.

Huson, M.G., Church, J.S., Kafi, A.A., Woodhead, A.L., Khoo, J., Kiran, M.S.R.N, Bradby, J., Fox, B.L. 2014. "Heterogeneity of Carbon Fibre," *Carbon* 68:240-249.

King, T.R., Blackketter, D.M., Walrath, D.E., and Adams, D.F., 1992. "Micromechanics Prediction of the Shear Strength of Carbon Fiber/ Epoxy Matrix Composites: The Influence of the Matrix and Shear Strengths," *Journal of Composite Materials,* 26(4):558-573.

Jalalvand, M., Czél, G., and Wisnom, M. R., 2015. "Damage Analysis of Pseudo-Ductile Thin-Ply UD Hybrid Composites—A New Analytical Method," *Composites Part A: Applied Science and Manufacturing*, 69:83-93

Kretsis, G., 1987. "A Review of the Tensile, Compressive, Flexure and Shear Properties of Hybrid Fibre-Reinforced Plastics," *Composites,* 18(1)

Lejunes, S., and Bourgeois, S., 2011. "An Abaqus Toolbox for the calculation of effective properties of heterogeneous media," *10th National Conference on Computational methods for Structures,* Giens, France.

Li, S., 200. "General unit Cells for Micromechanical Analyses of Unidirectional Composites," *Composites Part A,* (32): 815-826.

Marom, G., Fischer, S., Tuler, F., and Wagner, H., 1978. "Hybrid Effects in Composites: Conditions for Positive or Negative Effects Versus Rule-of-Mixtures Behaviour," *Journal of Materials Science,* 13:1419-1426.

Maurin, R., Davies, Baral, N., and Baley, C., 2008. "Transverse Properties of Carbon Fibres by Nano-Indentation and Micro-mechanics," *Applied Composite Materials,* 15:61-73.

Miyagawa, H., Mase, T., Sato, C., Drown, E., Drzal, L., and Ikegami, K., 2006. "Comparison of Experimental and Theoretical Transverse Elastic Modulus of Carbon Fibers," *Carbon,* 44:2002-2008.

Oliver, W.C. and Pharr, G.M., 1992. “An Improved Technique for Determining Hardness and Elastic Modulus Using Load and Displacement Sensing Indentation Experiments,” *Journal of materials research, 7*(6):1564-1583.

Ripepi, M.J., 2013. “Transverse Mechanical Properties of Unidirectionally Reinforced Hybrid Fiber Composites.” MS thesis. The Pennsylvania State University, University Park, PA.

Ross, J.W., 2013. “On the Optimization of Composite Flywheel Rotors.” PhD Dissertation. The Pennsylvania State University, University Park, PA.

Short, D., and Summerscales, J., 1980. “Hybrids – a Review.” *Composites*, 33-38

Sun, C.T., and Vaidya, R.S., 1996. “Prediction of Composite Properties from a Representative Volume Element,” *Composites Science and Technology*, 56: 171-179.

Sun, C.T., and Zhou, S.G., 1988. “Failure of Quasi-Isotropic Composite Laminates with Free Edges,” *Journal of Reinforced Plastic Composites,* 7:515-557.

Talreja, R., Huang, H., 2005. “Effects of Void Geometry on Elastic Properties of Unidirectional Fiber Reinforced Composites,” *Composites Science and Technology*, 65:1964-1981.

Tarnopol'skii, Yu. M., Zhigun, I. G., and Polyakov, V. A., 1991. *Spatially Reinforced Composites*. Technomic Publishing, Lancaster, PA, 352p.

Van Fo Fy, G.A., 1969. “Theoretical Prediction of the Properties of Multicomponent Reinforced Materials,” *Translated from Mekhanika Polimerov*, 4:646-654

Wikipedia. 2013. “Coefficient of Determination,” December 16.

http://en.wikipedia.org/wiki/Coefficient_of_determination

Wongsto, A., and Li, S., 2005. "Micromechanical FE Analysis of UD Fibre-Reinforced Composites with Fibres Distributed at Random over the Transverse Cross-Section," *Composites: Part A*, 36:1246-1266.

Appendix A
Python script for post processing the finite element results

The finite element models for the hybrid composites are analyzed in ABAQUS 6.14 (Dassault Systèmes Americas Corp., Waltham, MA) using C3D8 mesh element. The C3D8 is a three dimensional, continuum, 8-noded linear brick element as given in Figure 4. Each element has 2x2x2 integration points (Figure 5) where all the elemental stresses and strains components are outputted. The default coordinate system used by ABAQUS is given in Table A- 1.

Table A- 1. Sign convention in ABAQUS.

1 - 2 - 3 axes	*x* - *y* - *z* axes
1 - direction	*x* - direction (transverse direction)
2 - direction	*y* - direction (transverse direction)
3 - direction	*z* - direction (fiber direction)

In post processing the finite element results, if one wishes to evaluate the volume averaged stresses over the entire RUC like in equations (12) and (13); the procedure becomes very time consuming and prone to error. Therefore, these calculations are automated using Abaqus Python scripts. These scripts are provided by Barbero (2013) and can also be found at http://barbero.cadec-online.com/feacm-abaqus/

```
#Begin Post Processing

#Open the Output Data Base for the current Job
from visualization import *
#test32.obd is the output database file that is computed from the running finite element analysis
odb = openOdb(path=Jobname.odb');
myAssembly = odb.rootAssembly;

#Creating a temporary variable to hold the frame repository provides the same functionality and
speeds up the process
frameRepository = odb.steps['Step-1'].frames;
frameS=[];
frameIVOL=[];
```

```
#Get only the last frame [-1]
frameS.insert(0,frameRepository[-
1].fieldOutputs['S'].getSubset(position=INTEGRATION_POINT));
frameIVOL.insert(0,frameRepository[-
1].fieldOutputs['IVOL'].getSubset(position=INTEGRATION_POINT));
#Total Volume
#Note the total volume should also include the volume of the holes in order to be consistent with the equation 11 in “Transverse elastic properties of composites” subsection in Chapter 2
Tot_Vol=36.2*36.2*9.05;
#Stress Sum
Tot_Stress=0;
#
for II in range(0,len(frameS[-1].values)):
    Tot_Stress=Tot_Stress+frameS[0].values[II].data * frameIVOL[0].values[II].data;

#Calculate Average
Avg_Stress = Tot_Stress/(Tot_Vol);
#print 'Abaqus/Standard Stress Tensor Order:'
#From Abaqus Analysis User's Manual - 1.2.2 Conventions - Convention used for stress and strain components
#print 'Average stresses Global CSYS: 11-22-33-12-13-23';
#print Avg_Stress;
C11 = Avg_Stress[2]#z-component,1-direction
C21 = Avg_Stress[0]#x-component,2-direction
C31 = Avg_Stress[1]#y-component,3-direction in Figure 6

#Srecover macro--need to make this into a Python function
#Creating a temporary variable to hold the frame repository provides the same functionality and speeds up the process
frameRepository = odb.steps['Step-2'].frames;
frameS=[];
frameIVOL=[];
#Get only the last frame [-1]
frameS.insert(0,frameRepository[-
1].fieldOutputs['S'].getSubset(position=INTEGRATION_POINT));
frameIVOL.insert(0,frameRepository[-
1].fieldOutputs['IVOL'].getSubset(position=INTEGRATION_POINT));
#Total Volume
Tot_Vol=36.2*36.2*9.05;
#Stress Sum
Tot_Stress=0;
#
for II in range(0,len(frameS[-1].values)):
   Tot_Stress=Tot_Stress+frameS[0].values[II].data * frameIVOL[0].values[II].data;
```

```
#Calculate Average
Avg_Stress = Tot_Stress/Tot_Vol;
#print 'Abaqus/Standard Stress Tensor Order:'
#From Abaqus Analysis User's Manual - 1.2.2 Conventions - Convention used for stress and
strain components
#print 'Average stresses Global CSYS: 11-22-33-12-13-23';
#print Avg_Stress;
C12 = Avg_Stress[2]#z-component,1-direction
C22 = Avg_Stress[0]#x-component,2-direction
C32 = Avg_Stress[1]#y-component,3-direction in Figure 6

#Srecover.py
#Creating a temporary variable to hold the frame repository provides the same functionality and
speeds up the process
frameRepository = odb.steps['Step-3'].frames;
frameS=[];
frameIVOL=[];
#Get only the last frame [-1]
frameS.insert(0,frameRepository[-
1].fieldOutputs['S'].getSubset(position=INTEGRATION_POINT));
frameIVOL.insert(0,frameRepository[-
1].fieldOutputs['IVOL'].getSubset(position=INTEGRATION_POINT));
#Total Volume
Tot_Vol=36.2*36.2*9.05;
#Stress Sum
Tot_Stress=0;
#
for II in range(0,len(frameS[-1].values)):
    Tot_Stress=Tot_Stress+frameS[0].values[II].data * frameIVOL[0].values[II].data;

#Calculate Average
Avg_Stress = Tot_Stress/Tot_Vol;
#print 'Abaqus/Standard Stress Tensor Order:'
#From Abaqus Analysis User's Manual - 1.2.2 Conventions - Convention used for stress and
strain components
#print 'Average stresses in Global CSYS: 11-22-33-12-13-23';
#print Avg_Stress;
C13 = Avg_Stress[2]#z-component,1-direction
C23 = Avg_Stress[0]#x-component,2-direction
C33 = Avg_Stress[1]#y-component,3-direction in Figure 6

EL=C11-2*C12*C21/(C22+C23)            # Longitudinal E1 modulus
nuL=C12/(C22+C23)                  # 12 Poisson coefficient
ET=(C11*(C22+C23)-2*C12*C12)*(C22-C23)/(C11*C22-C12*C21)
                              # Transversal E2 modulus
```

```
nuT=(C11*C23-C12*C21)/(C11*C22-C12*C21) # 23 Poisson coefficient
GT=(C22-C23)/2 # or GT=ET/2/(1+nuT)     # 23 Shear stiffness

print "If Moduli are entered in GPa and dimensions in microns, results are in GPa"
print "E1=",EL,"GPa"
print "E2=",ET,"GPa"
print "PR12=",nuL
print "PR23=",nuT
```

Appendix B

Specimen preparation for microscopy

Three samples from the all-carbon and all-glass filament wound rings were prepared by Mr. Rudy Haluza to analyze the shape of the voids in a plane, parallel and perpendicular to the fiber direction. Once the specimens were extracted from the filament wound rings using a Felker 41-AR table saw with a water-cooled, diamond-edged cutting wheel, they were polished and observed under a modified optical microscope. The polishing procedure was done as follows.

The extracted samples were placed in a puck-shaped mold. The desired edge from the cut section was placed faced down in the mold. Next E862 epoxy resin and Jeffamine D403 hardener were mixed at a room temperature and poured into the mold. Once the resin system cured, the samples were taken to a polishing station.

The specimens were polished at Materials Research Institute at Penn State University-UP. Deionized water was used during sanding in order to produce a smooth, wet-sanded finish. The table and spindle both rotated the same way, but at different speeds listed in Table B- 1. Monocrystalline diamond suspension 3 μm and 1 μm particles were used in conjunction with a polishing cloth to produce a micro-polish finish on the surface of the puck. After the end of each cycle, the sanding disc or polishing was replaced and the next cycle was initiated.

Table B- 1. Polishing parameters including disc grits, spindle speed, pressure and cycle times

Sanding Disc Grit	Spindle Speed (rpm)	Table Speed (rpm)	Pressure (lbf)	Cycle Time (min)
320	65	120	1	2
800	65	120	1	2
1200	65	150	1	2
2400	80	150	2	2
4000	80	150	2	2
Polishing Cloth	Spindle Speed (rpm)	Table Speed (rpm)	Pressure (lbf)	Cycle Time (min)
3 μm	80	300	2	3
1 μm	80	300	2	3

Once polishing was finished the pucks were analyzed with a modified optical microscope. The optical microscope was equipped with a 3.1 Megapixel digital camera for imaging. The photo-micrographs in Figure 7, Figure 8 and Figure B- 1 confirmed that the voids in the filament wound rings are circular cylindrical in shape.

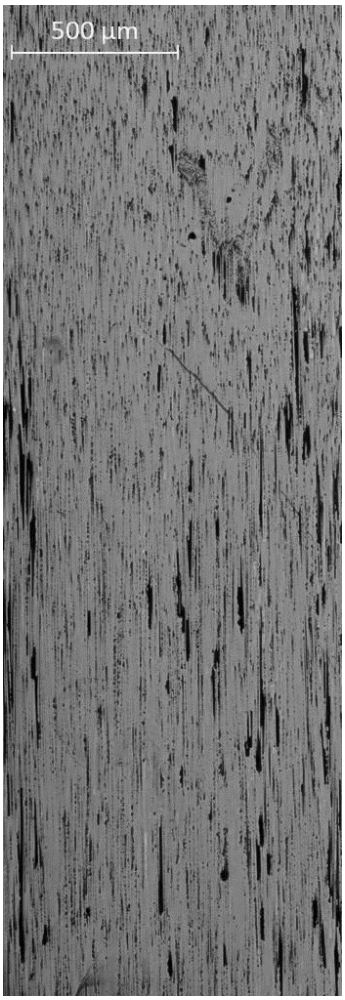

Figure B- 1. Photomicrograph of a polished 1-2 plane of unidirectional G100 composite nearly parallel to the fibers at 50x magnification. The dark regions are voids.

Appendix C

Beam test data obtained in present investigation

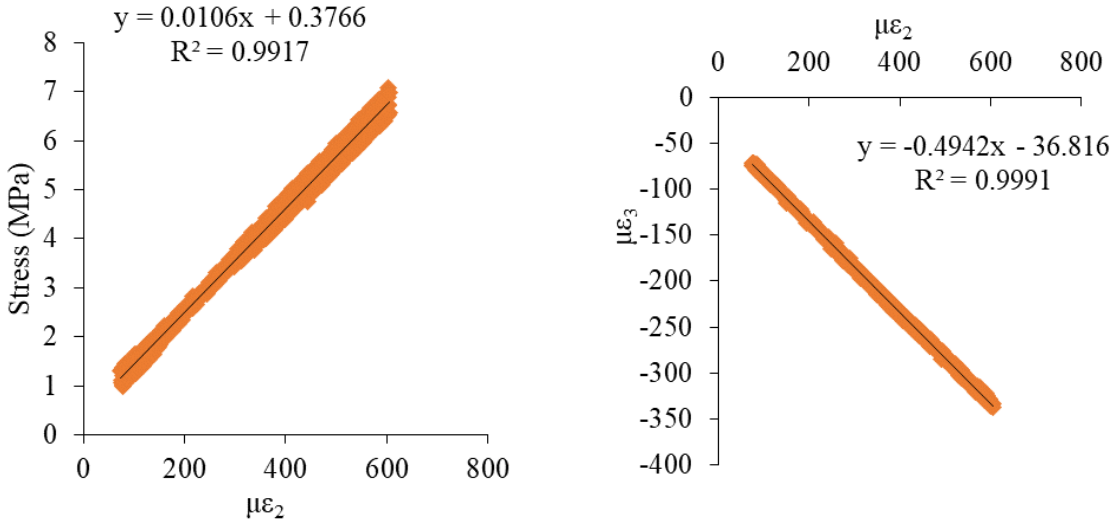

(a) (b)

Figure C- 1. C100 tensile side Test 1 (a) transverse stress vs. strain (in-plane) (b) out-plane strain vs in-plane strain

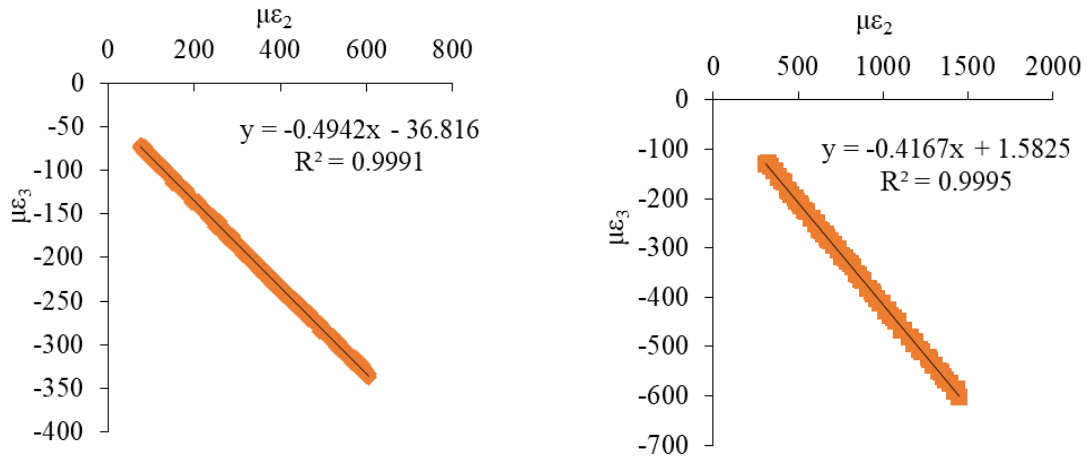

(a) (b)

Figure C- 2. C75G25 tensile side Test 1 (a) transverse stress vs. strain (in-plane) (b) out-planestrain vs in-plane strain

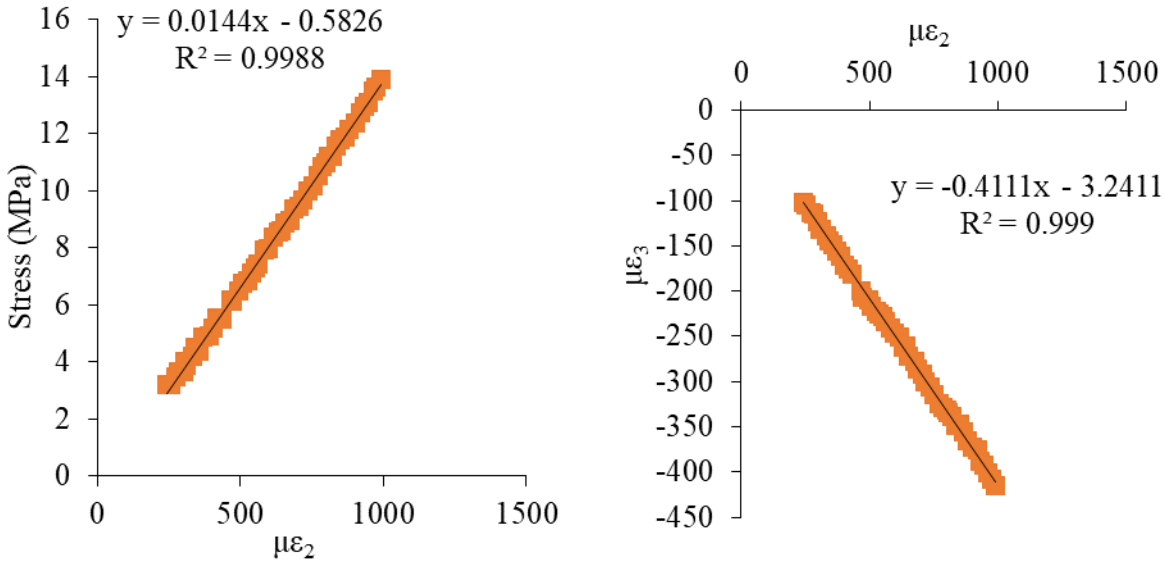

(a) (b)

Figure C- 3. C75G25 tensile side Test 2 (a) transverse stress vs. strain (in-plane) (b) out-plane strain vs in-plane strain

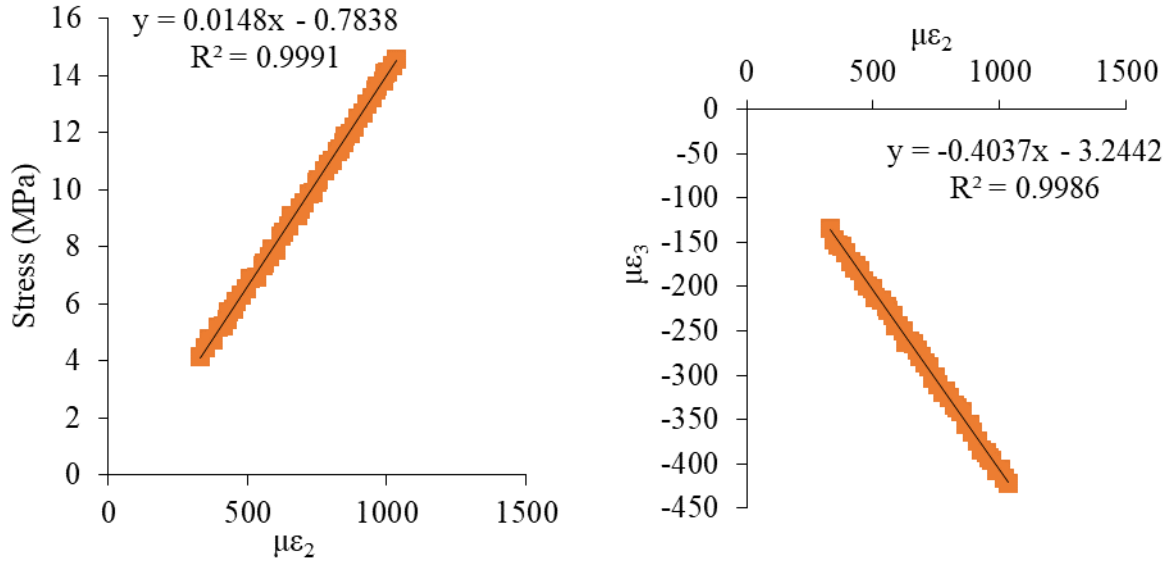

(a) (b)

Figure C- 4. C75G25 tensile side Test 2 (a) transverse stress vs. strain (in-plane) (b) out-plane strain vs in-plane strain

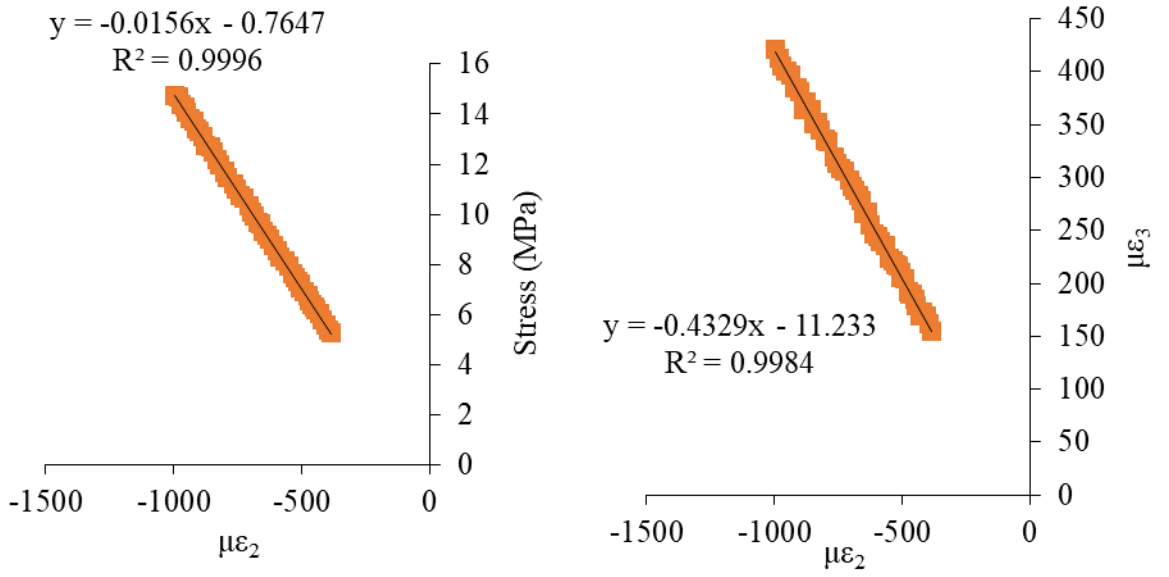

Figure C- 5. C75G25 compressive side Test 1 (a) transverse stress vs. strain (in-plane) (b) out-plane strain vs in-plane strain

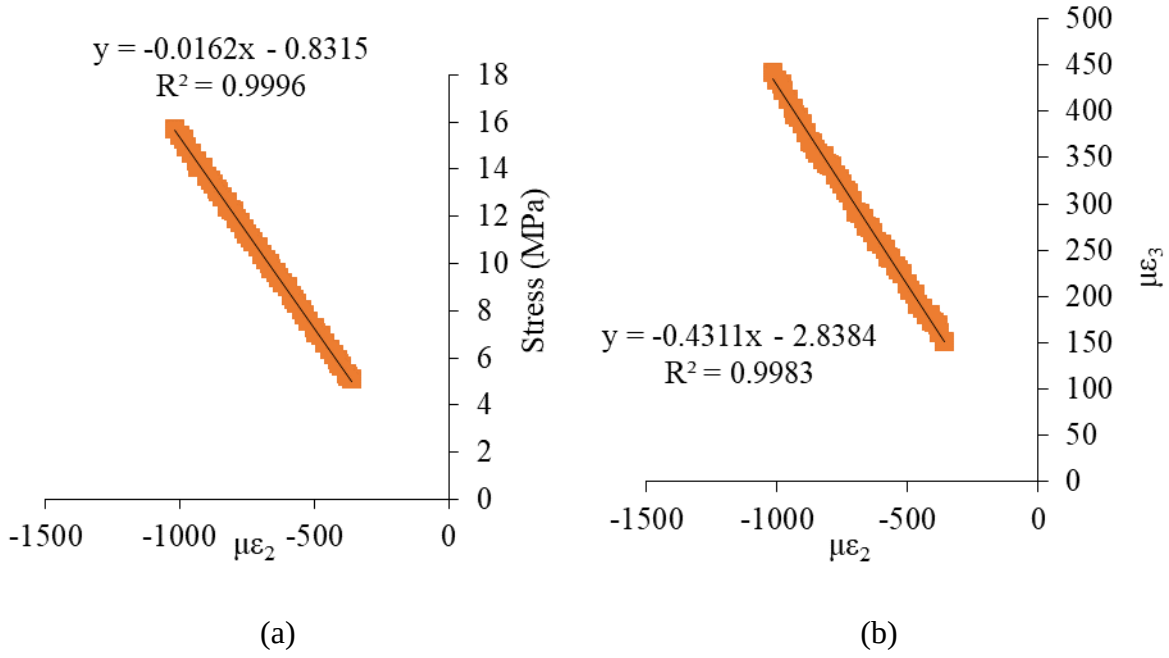

Figure C- 6. C75G25 compressive side Test 2 (a) transverse stress vs. strain (in-plane) (b) out-plane strain vs in-plane strain

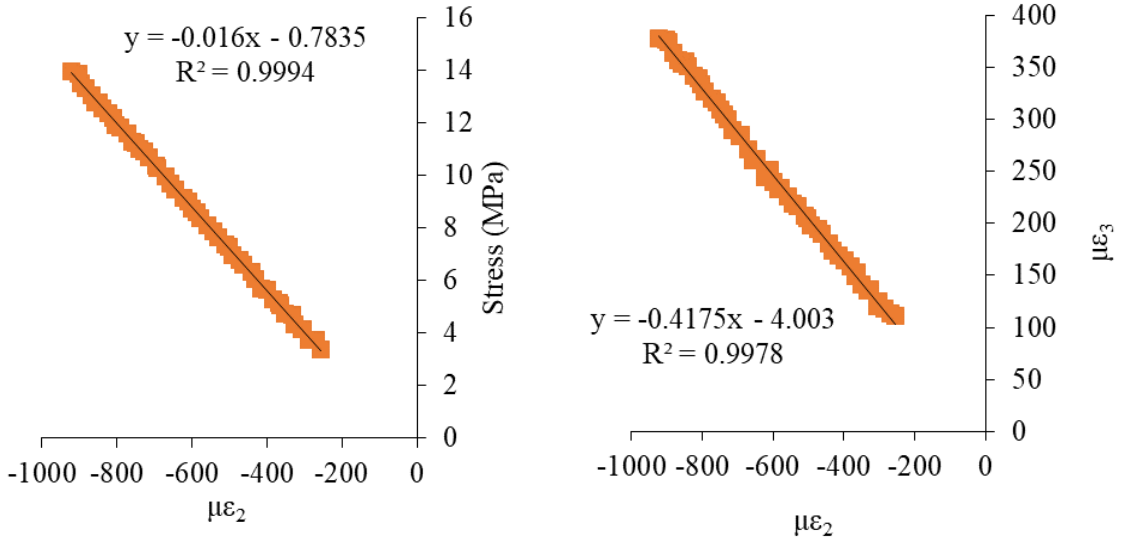

(a) (b)

Figure C- 7. C75G25 compression Test 3 (a) transverse stress vs. strain (in-plane) (b) out-plane strain vs in-plane strain

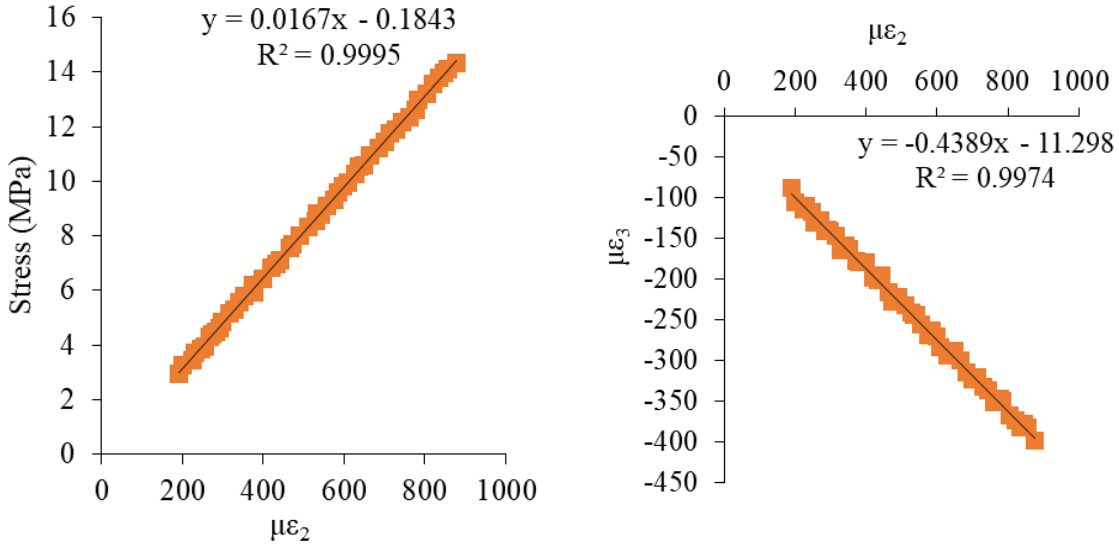

(a) (b)

Figure C- 8. C50G50 tensile side Test 1 (a) transverse stress vs. strain (in-plane) (b) out-plane strain vs in-plane strain

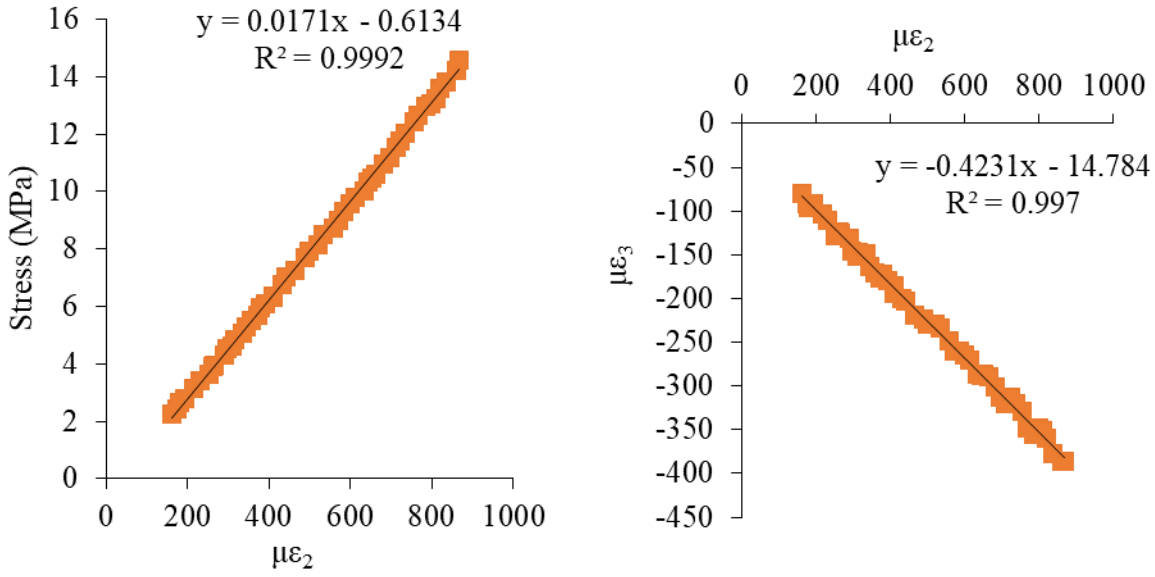

(a) (b)

Figure C- 9. C50G50 tensile side Test 2 (a) transverse stress vs. strain (in-plane) (b) out-plane strain vs in-plane strain

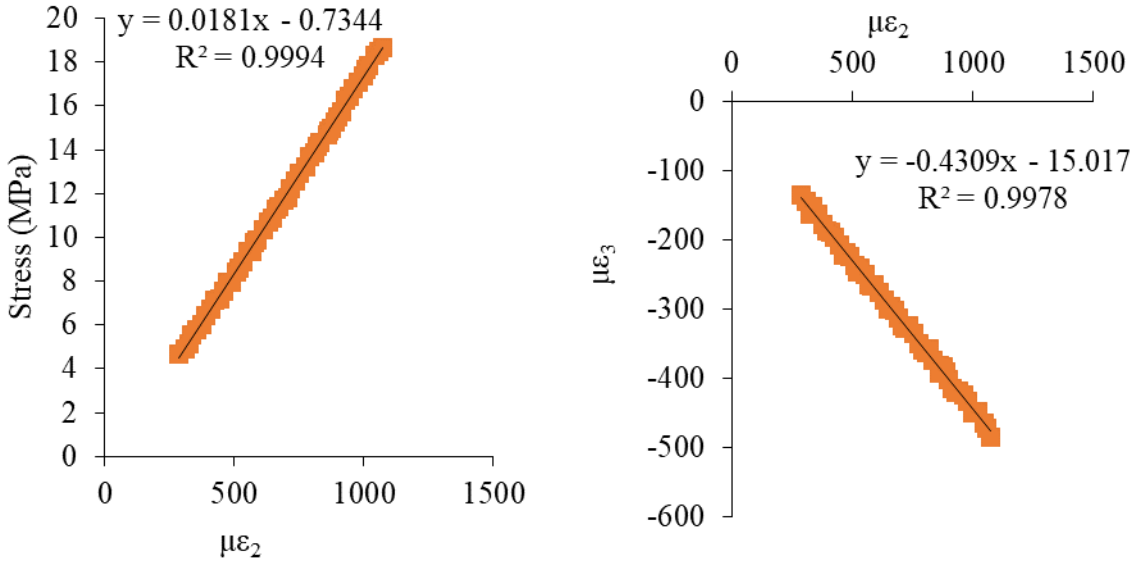

(a) (b)

Figure C- 10. C50G50 tensile side Test 3 (a) transverse stress vs. strain (in-plane) (b) out-plane strain vs in-plane strain

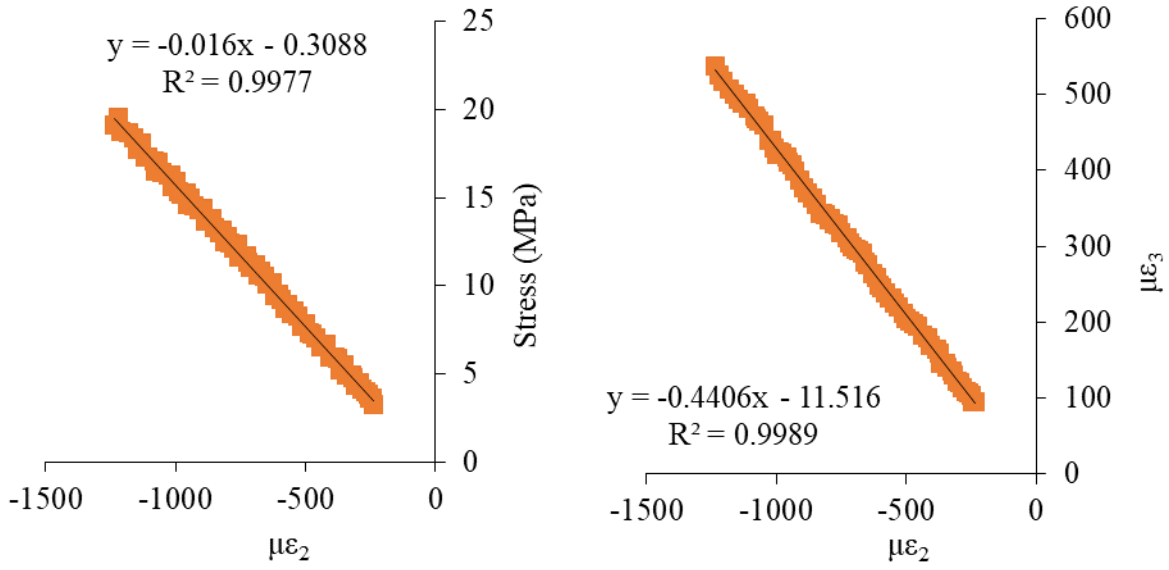

(a) (b)

Figure C- 11. C50G50 compressive side Test 1 (a) transverse stress vs. strain (in-plane) (b) out-plane strain vs. in-plane strain

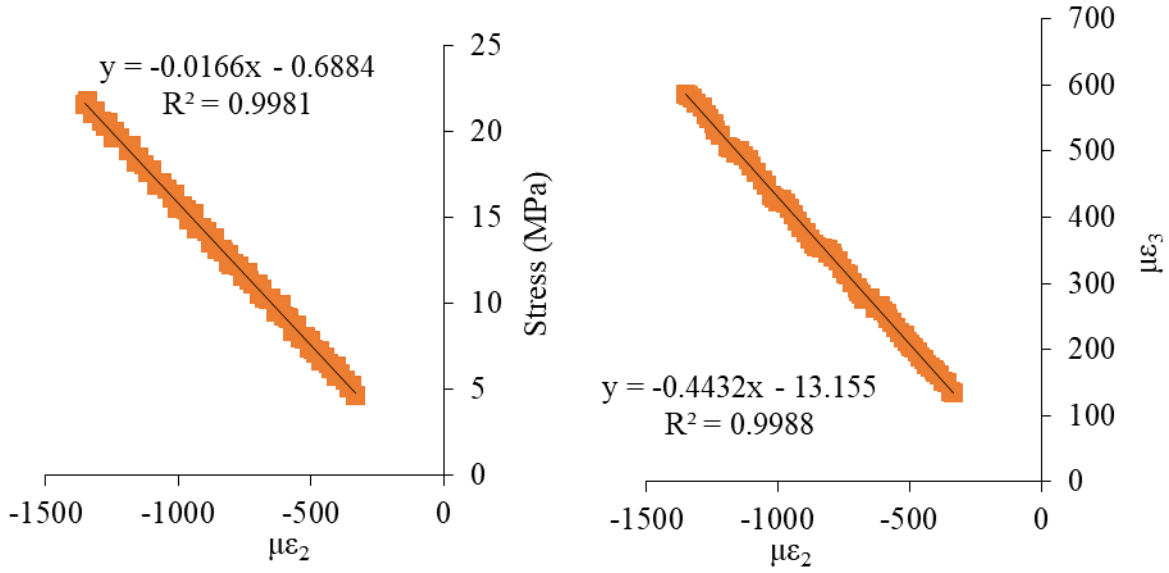

(a) (b)

Figure C- 12. C50G50 compressive side Test 2 (a) transverse stress vs. strain (in-plane) (b) out-plane strain vs. in-plane strain

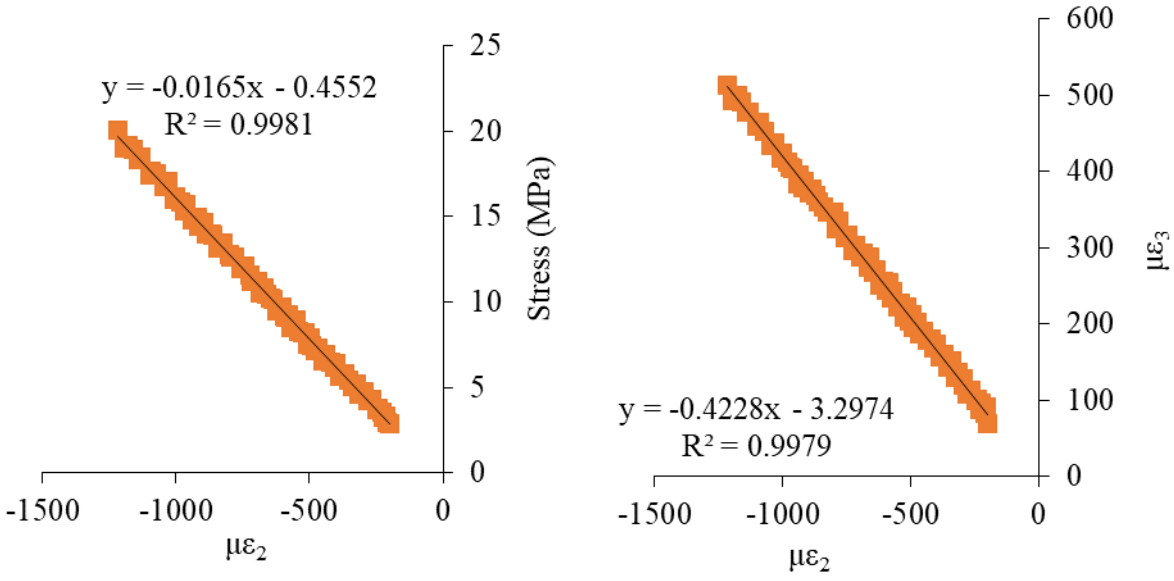

(a) (b)

Figure C- 13. C50G50 compressive side Test 3 (a) transverse stress vs. strain (in-plane) (b) out-plane strain vs. in-plane strain

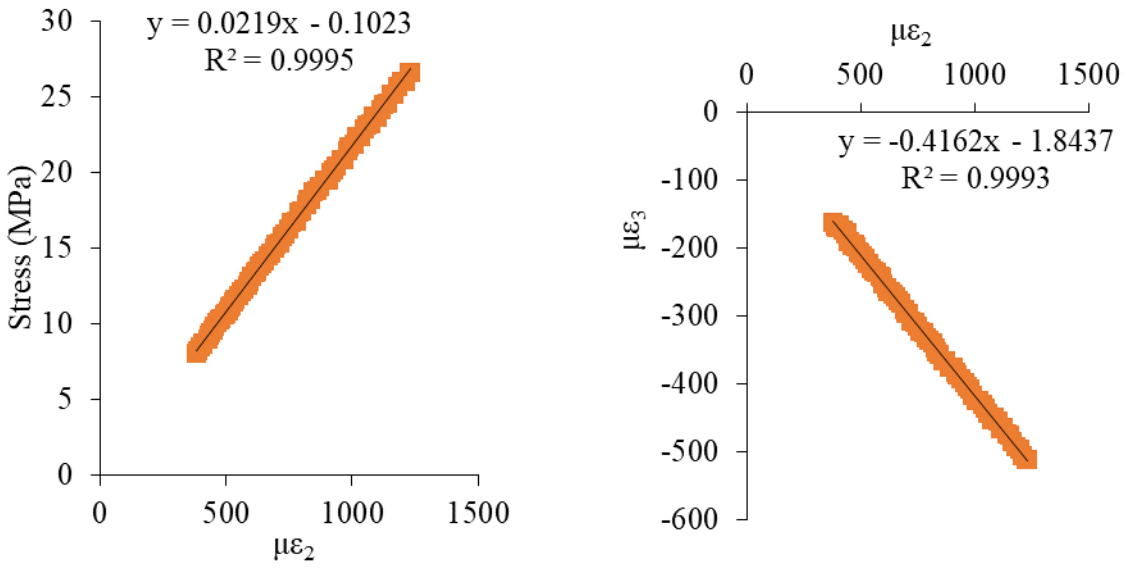

(a) (b)

Figure C- 14. C75G25 tensile side Test 1 (a) transverse stress vs. strain (in-plane) (b) out-plane strain vs in-plane strain

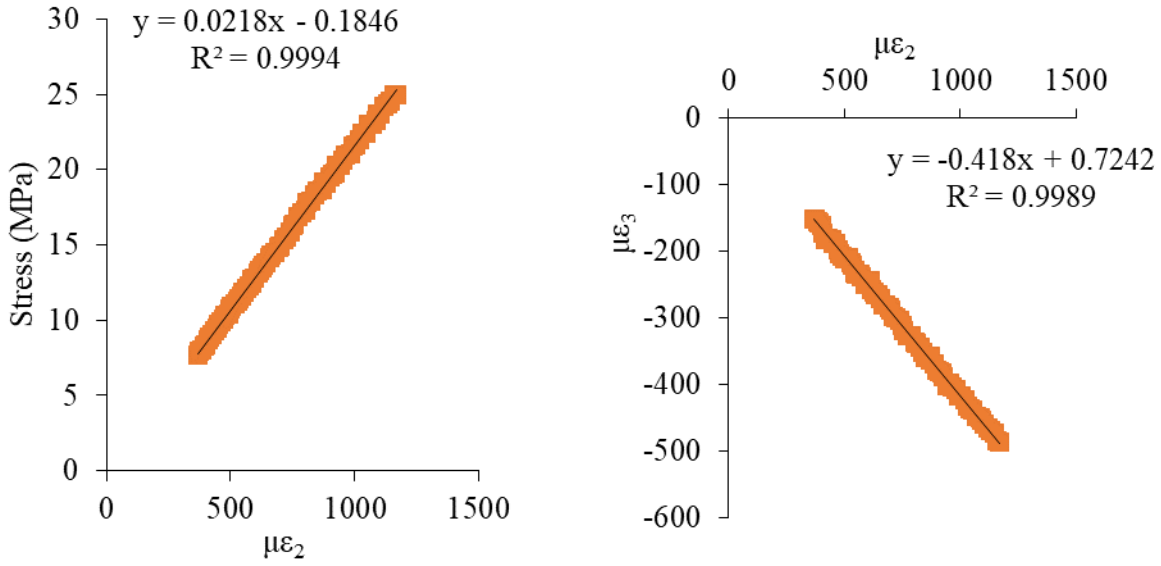

(a) (b)

Figure C- 15. C75G25 tensile side Test 2 (a) transverse stress vs. strain (in-plane) (b) out-plane strain vs in-plane strain

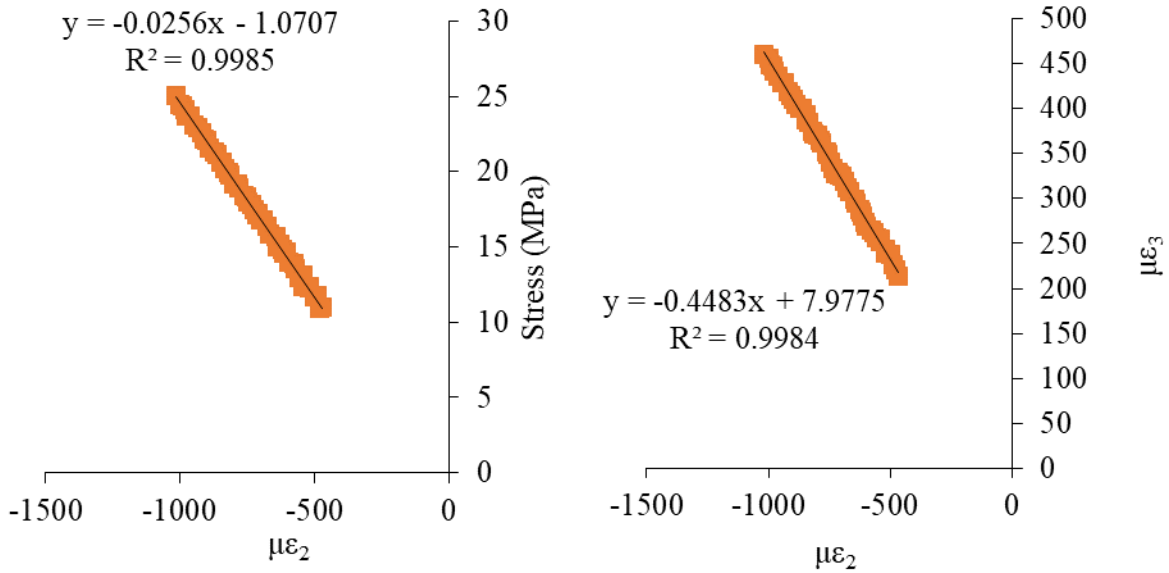

(a) (b)

Figure C- 16. C75G25 compressive side Test 1 (a) transverse stress vs. strain (in-plane) (b) out-plane strain vs in-plane strain

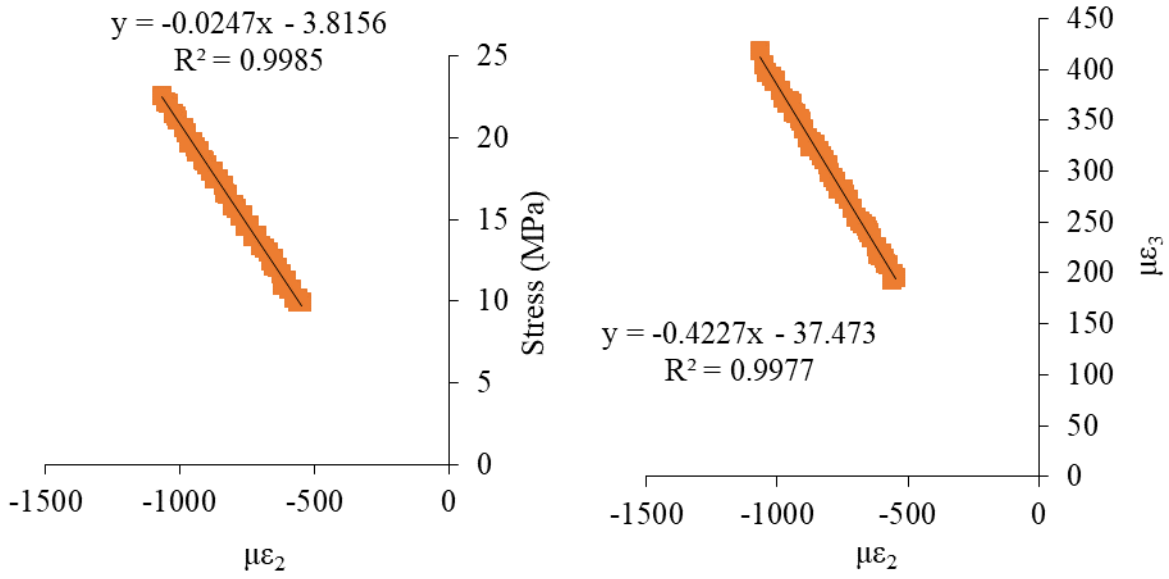

Figure C- 17. C75G25 compressive side Test 2 (a) transverse stress vs. strain (in-plane) (b) out-plane strain vs in-plane strain

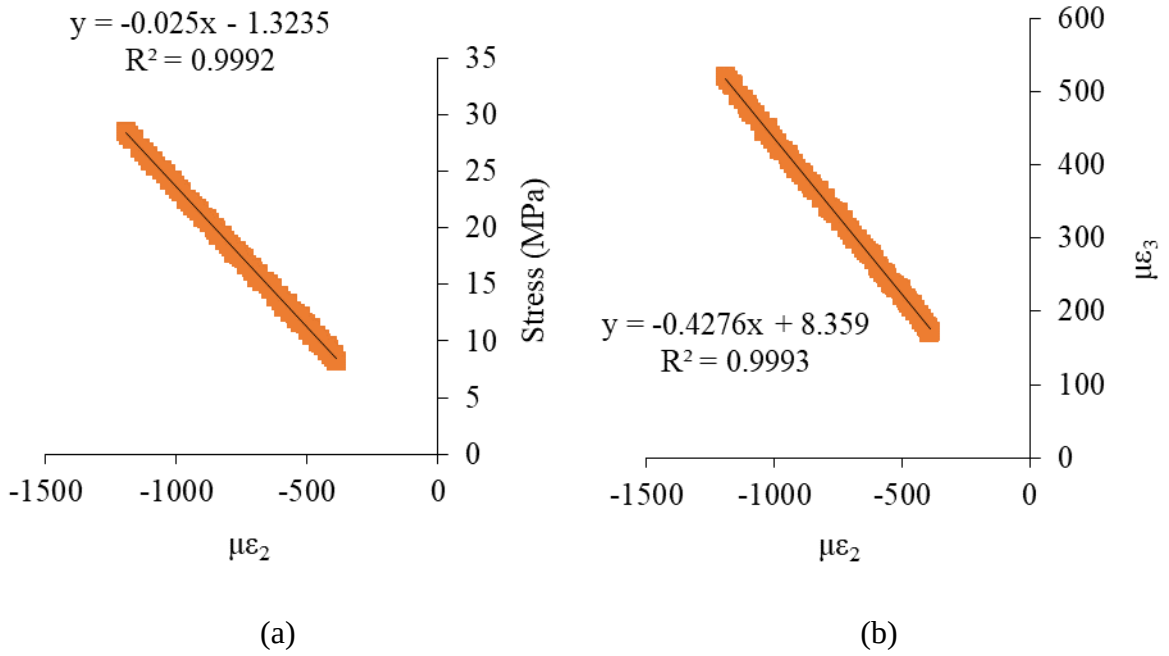

Figure C- 18. C75G25 compressive side Test 3 (a) transverse stress vs. strain (in-plane) (b) out-plane strain vs in-plane strain

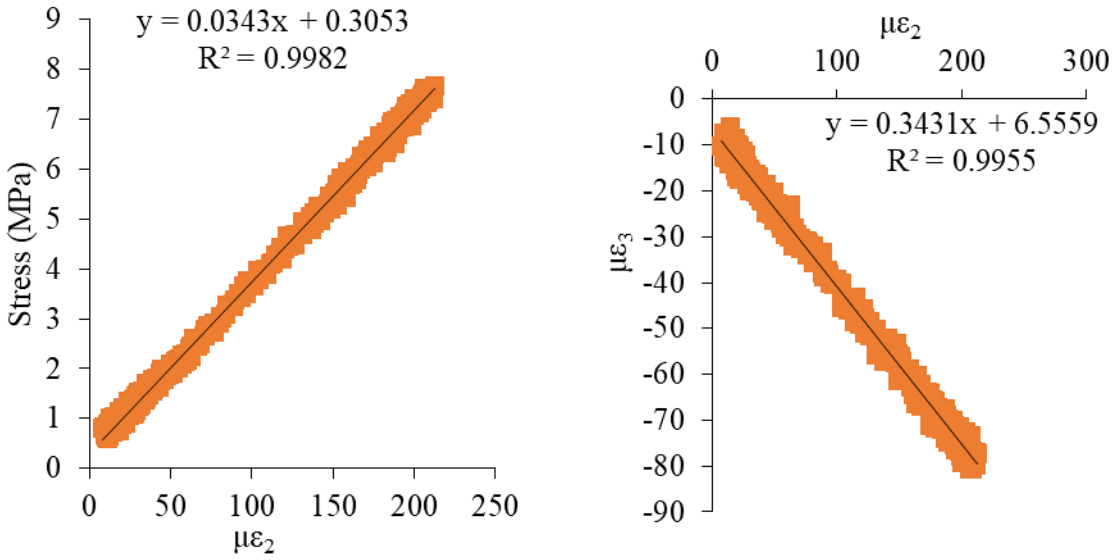

(a) (b)

Figure C- 19. G100 tensile side Test 1 (a) transverse stress vs. strain (in-plane) (b) out-plane strain vs in-plane strain

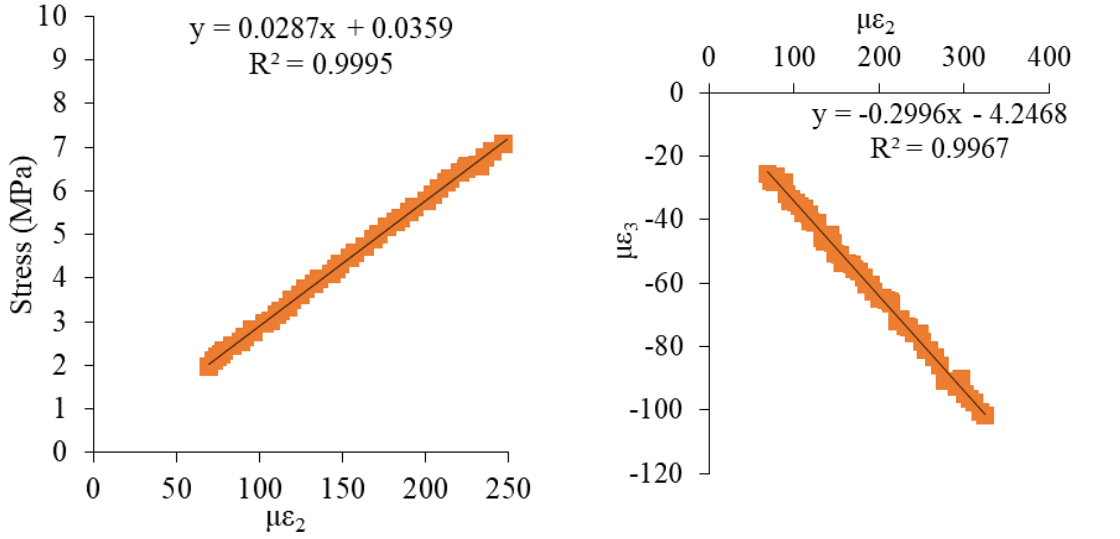

(a) (b)

Figure C- 20. G100 tensile side Test 2 (a) transverse stress vs. strain (in-plane) (b) out-plane strain vs in-plane strain

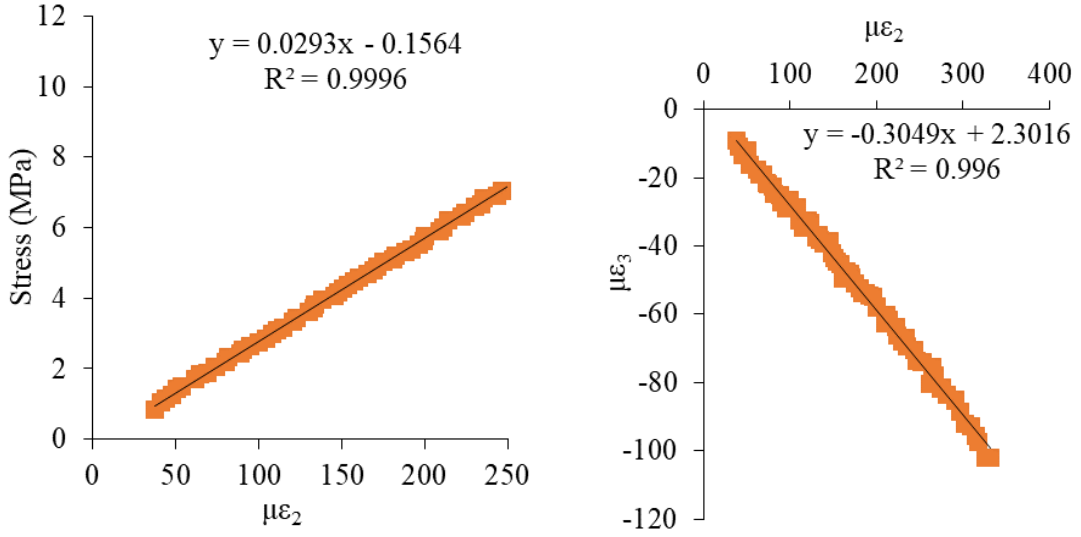

(a) (b)

Figure C- 21. G100 tensile side Test 3 (a) transverse stress vs. strain (in-plane) (b) out-plane strain vs in-plane strain

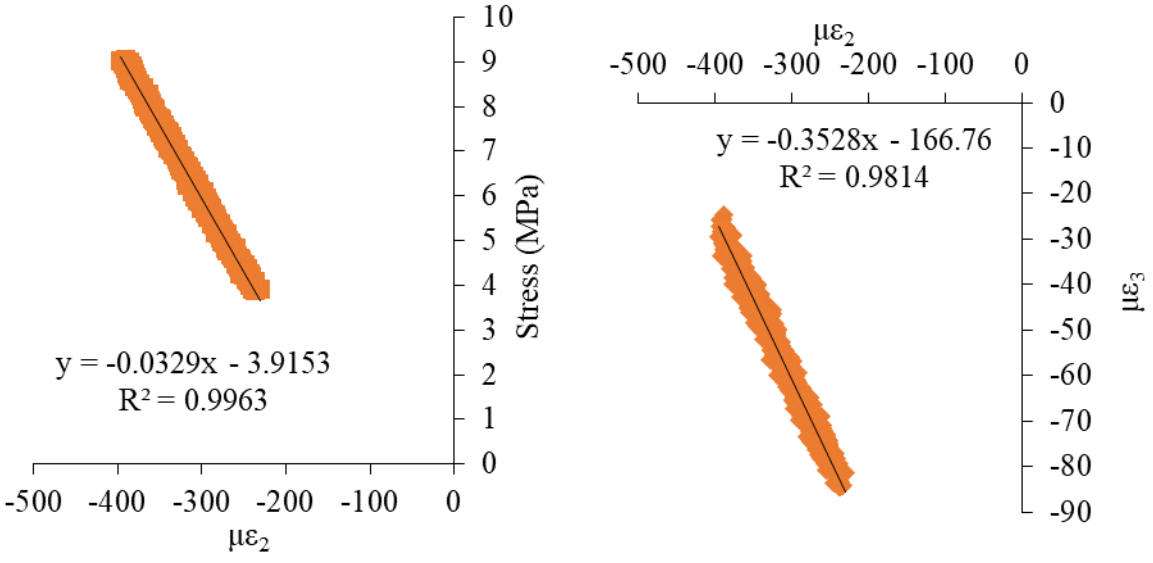

(a) (b)

Figure C- 22. G100 compressive side Test 1 (a) transverse stress vs. strain (in-plane) (b) out-plane strain vs in-plane strain

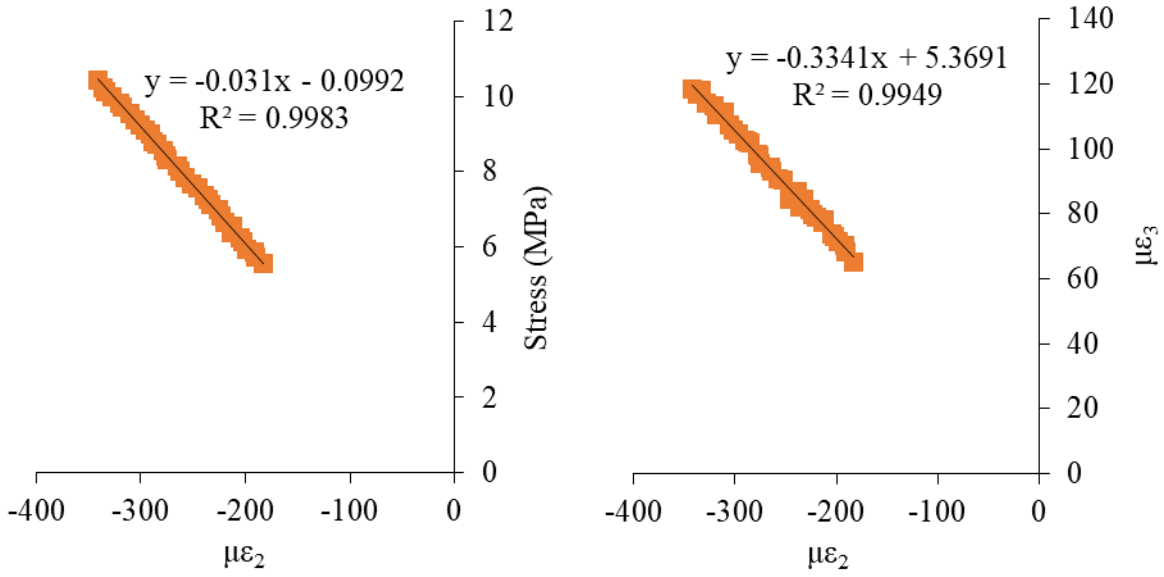

(a) (b)

Figure C- 23. G100 compressive side Test 2 (a) transverse stress vs. strain (in-plane) (b) out-plane strain vs in-plane strain

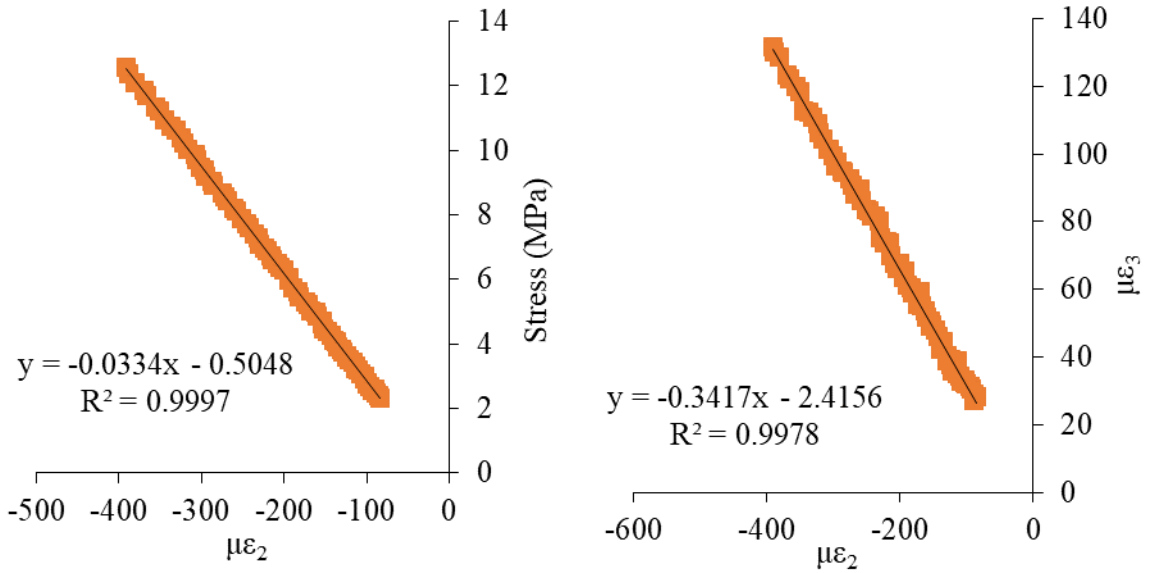

(a) (b)

Figure C- 24.G100 compressive side Test 3 (a) transverse stress vs. strain (in-plane) (b) out-plane strain vs in-plane strain

Table C- 1. Transverse Young's modulus and Poisson's ratio of C100 from biaxial measurement.

Test	E_2 (GPa)	ν_{23}
[1]Tensile side Test1	10.6	0.49

[1] FCA-2-11-3L biaxial strain gage

Table C- 2. Transverse Young's modulus and Poisson's ratio of C75G25 from strain gages.

Test	E_2 (GPa)	ν_{23}
[1]Tensile side Test1	14.5	0.42
[2]Tensile side Test2	14.4	0.41
[2]Tensile side Test3	14.8	0.41
Tensile side average	**14.6**	**0.41**
[1]Compressive side Test1	15.6	0.43
[2]Compressive side Test2	16.2	0.43
[2]Compressive side Test3	16.0	0.42
Compressive side average	**15.9**	**0.43**

[1]FCA-1-11-1LT biaxial strain gage; [2]FCA-2-11-3L biaxial strain gage

Table C- 3. Transverse Young's modulus and Poisson's ratio of C50G50 from strain gages.

Test	E_2 (GPa)	ν_{23}
Tensile side Test1	16.7	0.44
Tensile side Test1	17.1	0.42
Tensile side Test3	18.1	0.43
Tensile side average	**17.3**	**0.42**
Compressive side Test1	16.0	0.44
Compressive side Test2	16.6	0.44
Compressive side Test3	16.5	0.42
Compressive side average	**16.4**	**0.43**

Table C- 4. Transverse Young's modulus and Poisson's ratio of C25G75 from strain gages.

Test	E_2 (GPa)	ν_{23}
Tensile side Test1	21.9	0.42
Tension side Test 2	21.3	0.42
Tensile side average	**21.8**	**0.42**
Compressive side Test1	25.6	0.45
Compressive side Test2	24.7	0.42
Compressive side Test3	25.0	0.43
Compressive side average	**25.1**	**0.43**

Table C- 5. Transverse Young's modulus and Poisson's ratio of G100 from strain gages.

Test	E_2 (GPa)	ν_{23}
Tensile side Test1	34.3	0.34
Tensile side Test2	28.7	0.31
Tensile side Test3	29.3	0.30
Tensile side average	**30.8**	**0.32**
Compressive side Test1	32.9	0.35
Compressive side Test2	31.0	0.33
Compressive side Test3	33.4	0.34
Compressive side average	**32.4**	**0.34**

Appendix D

FEA of flexure-test of G100 beam in ABAQUS

In order to check if the dimensions of the beam influences the strains on the tensile and compressive surface of a beam in 4 point bending, a three dimensional finite element model of glass/epoxy composite was set up in ABAQUS 6.14 with the dimensions presented in Table 4 and load span , L = 55. The beam was modeled with C3D8I mesh elements. The C3D8I elements are three-dimensional, 8-node linear brick, incompatible model elements suitable for simulating bending. Fully integrated elements like C3D8 experience overly stiff behavior in bending dominated problems. This causes 'shear locking'. On the other hand reduced integration elements like C3D8H cannot detect strains at the integration point due to bending. C3D8I are fully integrated elements with incompatible deformation modes that eliminate the 'parasitic shear stresses' thereby eliminating the shear locking phenomenon. Therefore, these elements are used.

The elastic properties of glass/epoxy composite were obtained from Daniel and Ishai (2006) and was used as the input properties of the beam shown in Figure D- 1. The longitudinal and transverse direction of the beam was oriented along 1- and 2- direction of the rectangular Cartesian coordinates shown in Figure D- 1, respectively.

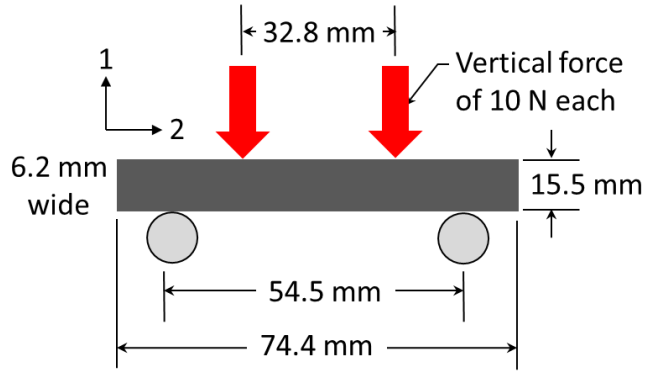

Figure D- 1. FEA of bend test of unidirectional G100 composite beam. 3-direction is oriented orthogonal to the 1-2 plane.

Boundary conditions were prescribed on the top surface of the beam as concentrated vertical total force of 20 N as shown in Figure D- 1. The translational degrees of freedom of the bottom edges were constrained to simulate a roller support. Once the model was run in ABAQUS, the 2-direction stress and the 2-direction (in-plane) strain were outputted from a node on the top and bottom surface of the beam located at the half-span, in order to compute the transverse Young's modulus, E_2. Also the 3-direction (out-plane) strain was outputted from the same nodes in order to compute the transverse Poisson's ratio, ν_{23}. The computed transverse elastic properties of the beam matched with the elastic properties inputted at the beginning of the analysis. This confirmed that the beam is well-designed.

Appendix E

Validation of finite element approach for modeling transverse Young's modulus and transverse Poisson's ratio

In order to validate the periodicity conditions presented in Table 2, these boundary conditions were prescribed to the square RUC developed by Sun and Vaidya (1995). Sun and Vaidya modeled unidirectional AS4/3501-6 carbon/epoxy composite with fiber volume fraction of 0.6. The elastic modulus of the 3501-6 epoxy is E_m = 4.8 GPa and the Poisson's ratio is ν_{23} = 0.34. The properties of the fiber are given in Table E-1. RUC with the same fiber volume fraction and material properties were constructed in ABAQUS. In order to determine the transverse elastic properties of the RUC, Sun and Vaidya (1995) applied a distributed 2-direction force to the opposite faces, $y = 0, a$, (Figure E-1) such that the 2-direction elongation between the faces is constant for all x and z. In order to enforce compatibility and periodicity, the displacements of all six sides of the RUC were constrained so that the RUC remains a right rectangular cuboid after deformation.

The transverse elastic properties of the composite computed by Sun and Vaidya (1995) and in the current investigation are compared in Table E- 2. The periodicity conditions utilized in this study simulated a value for E_2 and ν_{23} of the composite that was only slightly different from the transverse elastic properties obtained by Sun and Vaidya (1995). Therefore, the finite element approach to model RUCs using the periodicity conditions presented in Table 2 is valid.

Table E-1. AS4 carbon fiber properties used by Sun and Vaidya (1995) to model AS4/3501-6 carbon/epoxy composite.

	E_{1c} (GPa)	E_{2c} (GPa)	ν_{12c}	ν_{23c}
Elastic constants	245	14	0.2	0.25

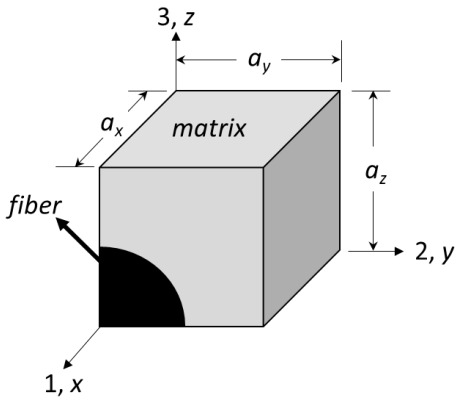

Figure E- 1. RUC quadrant for square array of AS4/3501-6 carbon/epoxy composite used by Sun and Vaidya (1995).

Table E- 2. Comparison of transverse elastic properties of AS4/3501-6 carbon epoxy composite between Sun and Vaidya (1995), and periodicity boundary conditions in the current approach.

	Sun and Vaidya (1995)	FEA using periodicity conditions
E_2 (GPa)	9.60	9.61
ν_{23}	0.35	0.35

Appendix F

FEA analysis of G100 model with four holes in each corner

In order to check the effect of the number of voids in the matrix on the transverse elastic properties of the composite, four circular cylinder holes were placed at each corner of a G100 RUC as shown in Figure F- 1. The volume fractions of the constituents are in Table 7, and the matrix properties are listed in Table 5 and Table 6. The isotropic E-glass fiber is assumed to have an elastic modulus (E_g) of 80.0 GPa and a Poisson's ratio (ν_g) of 0.26. The periodicity conditions from Table 2 were applied to the RUC with converged mesh size of 173,043 elements. The results are compared with Approach 2, i.e an RUC with one void in each corner, in Table F- 1. Based on this study we can conclude that there is no effect on the number of voids on the transverse elastic properties of the composite.

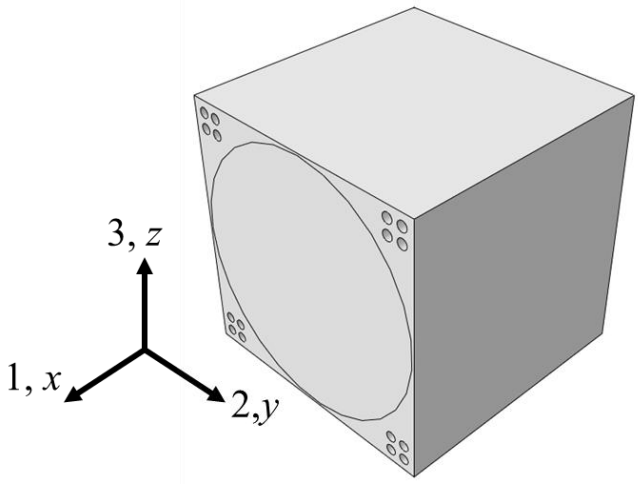

Figure F- 1. RUC of G100 model with four holes as voids at each corner.

Table F- 1. Results of FEA on effect of number of voids on transverse elastic properties of the composite.

	E_2 (GPa) (Difference[1])	ν_{23} (Difference[1])
Experimental	29.0	0.32
RUC with four holes at each corner	30.5 (5.2)	0.20 (-37.5)
RUC with one hole at each corner	30.5 (5.2)	0.20 (-37.5)

[1] $Difference(\%) = \frac{FEA-Exp}{Exp} \cdot 100\ \%$

Appendix G

Data set for parametric study for backing out carbon fiber properties

Table G- 1. Transverse Young's modulus (E_2) and Poisson's ratio (ν_{23}) of the all-carbon composite as a function of transverse Young's modulus (E_{2c}) and Poisson's ratio (ν_{23c}) of carbon fiber.

Poisson's ratio of fiber, ν_{23c}	Young's modulus of fiber, E_{2c} (GPa)													
	24.3		24.5		24.7		24.9		25.1		25.3		25.4	
	E_2 (GPa)	ν_{23}	E_2 (GPa)	ν_{23}	E_2 (GPa)	ν_{23}	E_2 (GPa)	ν_{23}	E_2 (GPa)	ν_{23}	E_2 (GPa)	ν_{23}	E_2 (GPa)	ν_{23}
0.5	11.46	0.35	11.51	0.35	11.57	0.35	11.61	0.35	11.67	0.35	11.72	0.35	11.76	0.34
0.6	11.40	0.39	11.45	0.39	11.50	0.39	11.54	0.39	11.60	0.39	11.65	0.39	11.70	0.39
0.7	11.34	0.43	11.39	0.43	11.43	0.43	11.48	0.43	11.54	0.43	11.59	0.43	11.64	0.43
0.8	11.28	0.48	11.32	0.47	11.38	0.47	11.42	0.47	11.48	0.47	11.52	0.47	11.58	0.47
0.9	11.22	0.52	11.28	0.52	11.33	0.52	11.37	0.51	11.42	0.51	11.47	0.51	11.53	0.51

Appendix H

Checks on thermodynamic constraints for positive definiteness of stress-strain relationships

The thermodynamic constraints for positive-definite stress-strain relationships provided by Jones (1975) are given in equations H-1 through H-6,

$$|S_{23}| < (S_{22}S_{33})^{1/2} \tag{H-1}$$

$$|S_{13}| < (S_{11}S_{33})^{1/2} \tag{H-2}$$

$$|S_{12}| < (S_{22}S_{11})^{1/2} \tag{H-3}$$

$$C_{11}, C_{22}, C_{33} > 0 \tag{H-4}$$

$$S_{11}, S_{22}, S_{33} > 0 \tag{H-5}$$

$$\bar{\Delta} = 1 - \nu_{12c}\nu_{21c} - \nu_{23c}\nu_{32c} - \nu_{31c}\nu_{13c} - 2\nu_{21c}\nu_{32c}\nu_{13c} > 0 \tag{H-6}$$

where,

$S_{11}, S_{22}, S_{33}, S_{12}, S_{13}, S_{23}$: Components of compliance matrix
C_{11}, C_{22}, C_{33}: Components of stiffness matrix

The stiffness matrix and compliance matrix were constructed by substituting the carbon fiber properties (Table 12) in equations (H-1) through (H-6). The components (Table H- 1) of these matrices satisfied all the thermodynamic constraints (Table H-2). Therefore, the backed out elastic properties of carbon fibers are feasible.

Table H- 1. Parameters used to check thermodynamic constraints.

	Values
C_{11} (Pa)	2.59E+11
C_{22} (Pa)	9.61E+10
C_{33} (Pa)	9.61E+10
S_{11} (m/N)	4.08E-12
S_{22} (m/N)	3.95E-11
S_{33} (m/N)	3.95E-11
S_{12} (m/N)	-8.16E-13
S_{13} (m/N)	-8.16E-13
S_{33} (m/N)	-3.36E-11
$\bar{\Delta}$	1.67E-33

Table H-2. Evaluation of compliance and stiffness terms presented in equations (H-1) to (H-6).

Equation	Inequality	Evaluation
(H-1)	$3.36\text{x}10^{-11} < 3.95\text{x}10^{-11}$	Satisfied
(H-2)	$8.16\text{x}10^{-13} < 1.27\text{x}10^{-11}$	Satisfied
(H-3)	$8.16\text{x}10^{-11} < 1.27\text{x}10^{-11}$	Satisfied
(H-4)	$2.6\text{x}10^{-11}, 9.61\text{x}10^{-10}, 9.61\text{x}10^{-10} > 0$	Satisfied
(H-5)	$4.08\text{x}10^{-12}, 3.95\text{x}10^{-11}, 3.95\text{x}10^{-11} > 0$	Satisfied
(H-6)	$1.67\text{x}10^{-33} > 0$	Satisfied

Appendix I

Contour plots of stresses and displacements of C75G25 RUC based on periodicity conditions

The dimensions of the C75G25 RUC can be found in Table 16. The volume fractions of the constituents are in Table 7, and the matrix properties are listed in Table 5 and Table 6. The isotropic E-glass fiber is assumed to have an elastic modulus (E_g) of 80.0 GPa and a Poisson's ratio (ν_g) of 0.26, and the carbon fiber properties are presented in Table 12. The boundary conditions presented in Table 2 are enforced on the RUC in FEA.

Figure I-1, Figure I-7 and Figure I-9 represent the elemental stresses in 1-, 2- and 3-directions, respectively, when unit normal strains are applied sequentially in 1-, 2- and 3-directions. Figure I-2, Figure I-8 and Figure I-10 represent the displacement field in these conditions. Figure I-3 and Figure I-5 represent the elemental stresses in 2 and 3-direction when unit normal strain is applied in 1-direction. Under the same loading condition, Figure I-4 and Figure I-6 represent the elemental displacements in 2- and 3-direction. Although unit strains were applied to the RUC, they were enforced in an average sense. Therefore, the $y = 0$ and $y = a_y$ and $z = 0$ and $z = a_z$ boundaries will not deform planar. This is because the geometric symmetries no longer exist because the unit cell includes fibers with different material properties and diameters. The stiffness and compliance matrix obtained by enforcing the periodicity conditions in Table 2, given by (I-1) and (I-2),

$$\bar{C}_{ij} = \begin{bmatrix} 147.28 & 6.72 & 6.72 \\ 6.72 & 18.22 & 8.52 \\ 6.72 & 8.52 & 18.22 \end{bmatrix} \text{x}10^9 \text{ Pa} \quad \text{(I-1)}$$

$$\bar{S}_{ij} = \begin{bmatrix} 6.95 & -1.74 & -1.74 \\ -1.74 & 0.071 & -0.032 \\ -1.74 & -0.032 & 0.071 \end{bmatrix} \text{x}10^{-12}\ (\text{Pa})^{-1} \quad \text{(I-2)}$$

show that the matrices are diagonally symmetric and the material exhibits transverse isotropy, as expected.

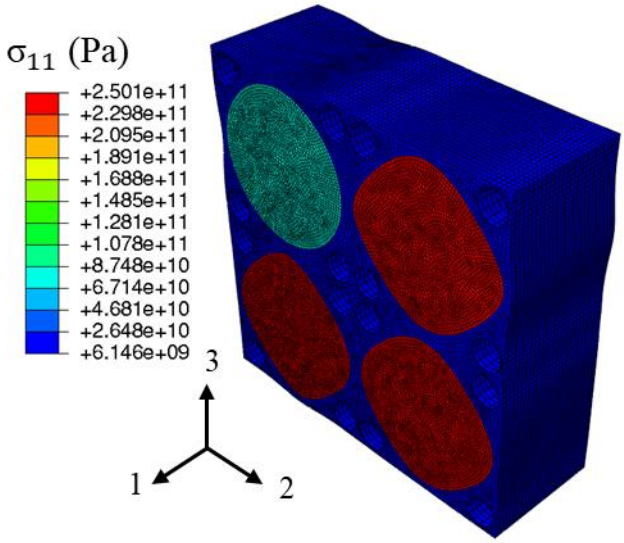

Figure I-1. Contour plot of 1-direction elemental stresses in C75G25 RUC when $\bar{\varepsilon}_1 = 1$

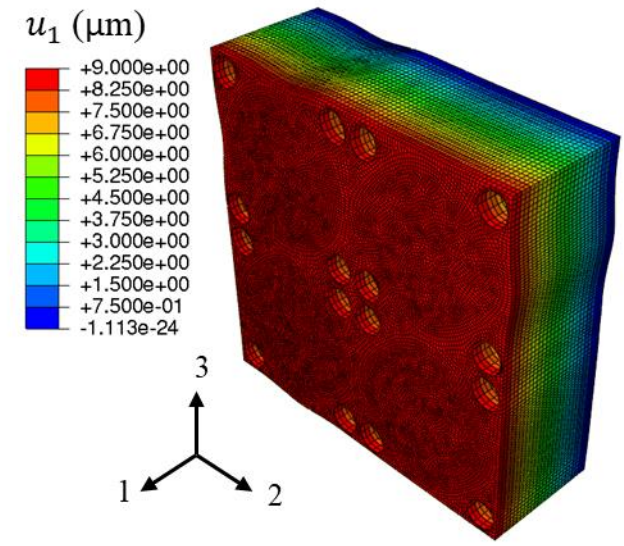

Figure I-2. Contour plot of 1-direction elemental displacements in C75G25 RUC when $\bar{\varepsilon}_1 = 1$

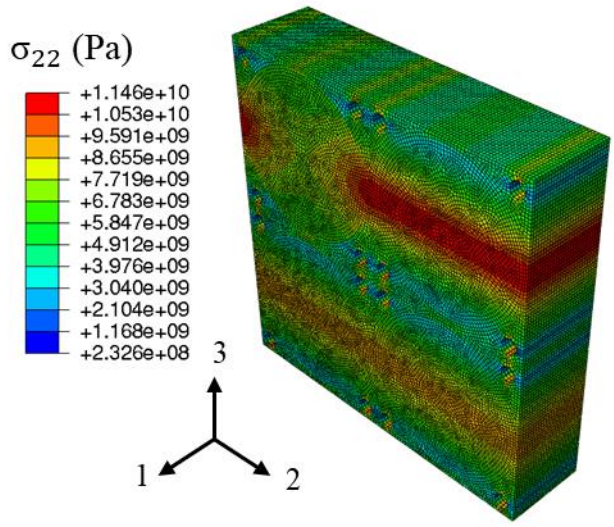

Figure I-3. Contour plot of 2-direction elemental stresses in C75G25 RUC when $\bar{\varepsilon}_1$ = 1

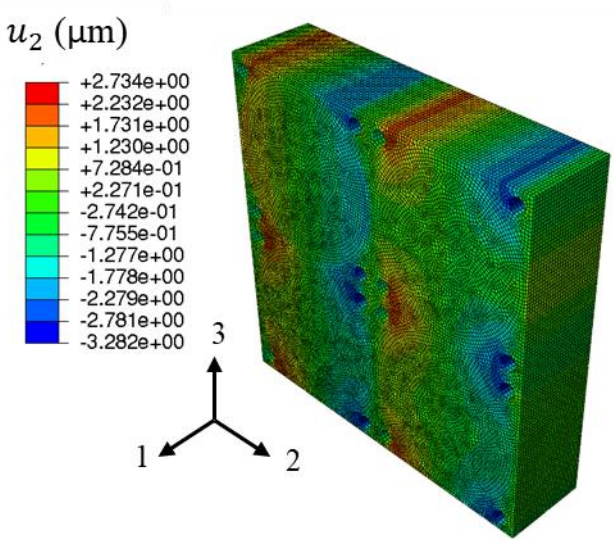

Figure I-4. Contour plot of 2-direction elemental displacements in C75G25 RUC when $\bar{\varepsilon}_1$ = 1

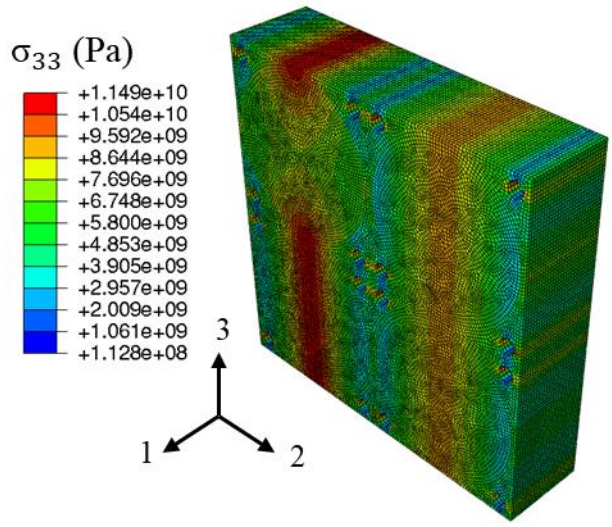

Figure I-5. Contour plot of 3-direction elemental stresses in C75G25 RUC when $\bar{\varepsilon}_1$ = 1

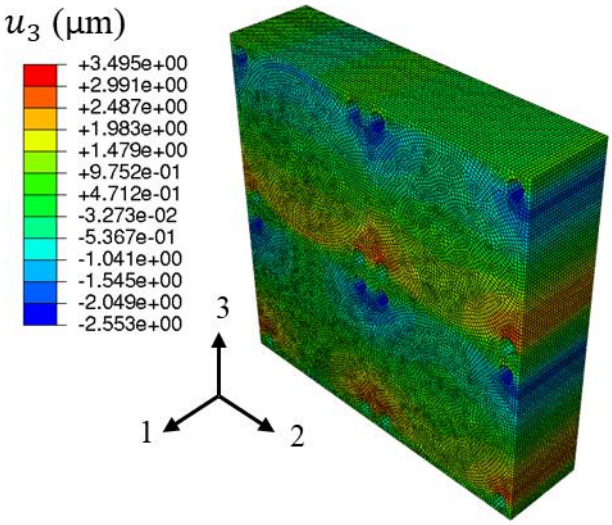

Figure I-6. Contour plot of 3-direction elemental displacements in C75G25 RUC when $\bar{\varepsilon}_1$ = 1

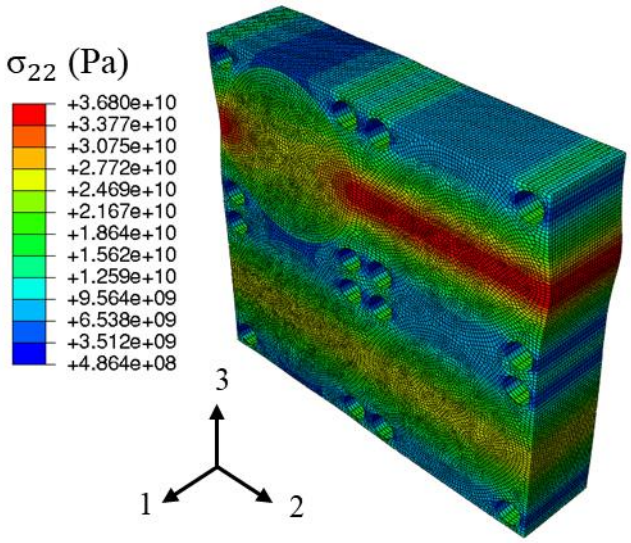

Figure I-7. Contour plot of 2-direction elemental stresses in C75G25 RUC when $\bar{\varepsilon}_2$ = 1

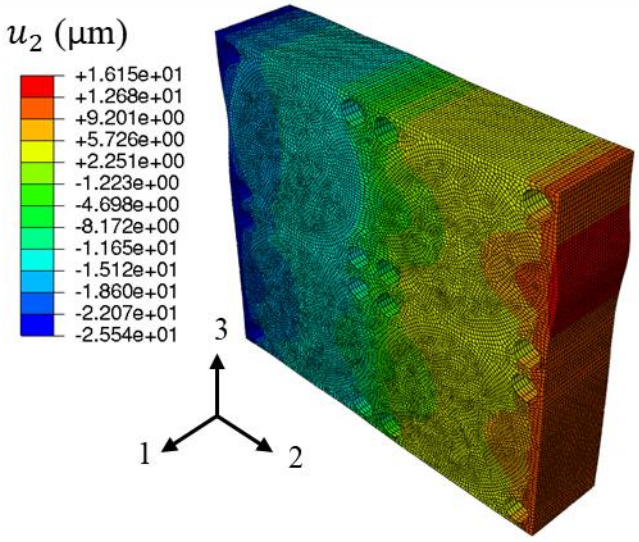

Figure I-8. Contour plot of 2-direction elemental displacements in C75G25 RUC when $\bar{\varepsilon}_2$ = 1

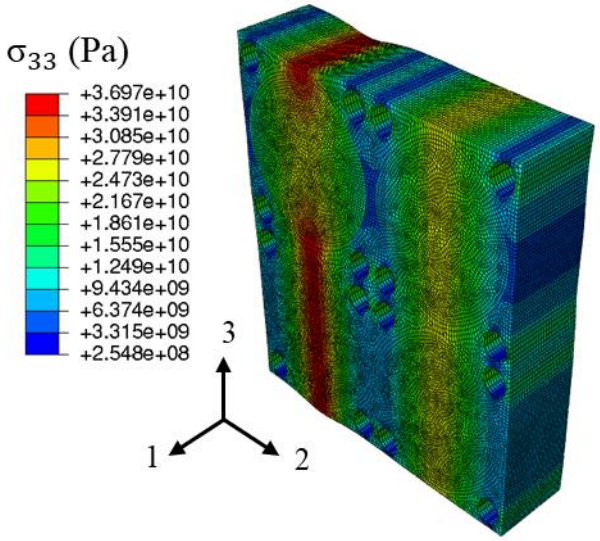

Figure I-9. Contour plot of 3-direction elemental stresses in C75G25 RUC when $\bar{\varepsilon}_3 = 1$

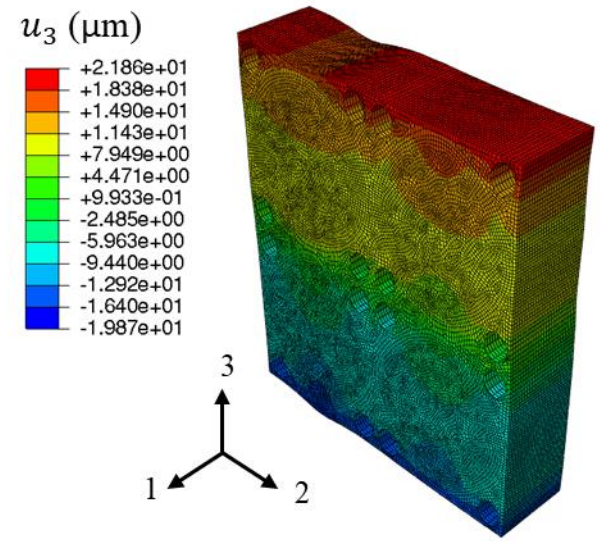

Figure I-10. Contour plot of 3-direction elemental displacements in C75G25 RUC when $\bar{\varepsilon}_3 = 1$

Appendix J

FEA of C50G50 model based on fiber positioning about diagonal plane

Stress partitioning parameter parameters ($\eta_{\sigma c}$ and $\eta_{\sigma g}$) are defined as the ratio of the volume averaged 2-direction stress in fibers to the volume averaged 2-direction stress matrix. This analysis is performed on C50G50 model to check if (a) the material is rectangularly transversely isotropic (b) the SPPs vary with the positioning of carbon and glass fiber in the RUC.

In order to compute the transverse Young's moduli (E_2 and E_3), and the SPPs in 2-direction, the periodic boundary conditions presented in equations (J-1) were applied, respectively, onto the RUC shown in Figure 21 (b) and (c). To get the SPPs in 3-direction, $\bar{\varepsilon}_{33}$ was taken as 1 to simulate uniaxial tension in 3-direction, equation (J-2). The geometry of the model is presented in Table 16 and, the matrix properties are obtained from Table 5 and Table 6. The SPPs were computed as the ratio of volume average of 2-direction stress in fiber to the volume average of 2-direction stress in matrix, given in equations (J-1) and (J-2). Similarly the SPPs were computed for 3-direction uniaxial tension based on the equations in (J-3) and (J-4).

$$\begin{gathered} u_1(a_x, y, z) - u_1(0, y, z) = -a_x \nu_{21} \bar{\varepsilon}_{22} \text{ for } 0 \le y \le a_y,\ 0 \le z \le a_z \\ u_2(x, a_y, z) - u_2(x, 0, z) = a_y \bar{\varepsilon}_{22} \text{ for } 0 \le x \le a_x,\ 0 \le z \le a_z \\ u_3(x, y, a_z) - u_3(x, y, 0) = -a_z \nu_{23} \bar{\varepsilon}_{22} \text{ for } 0 \le x \le a_x,\ 0 \le y \le a_y \end{gathered} \tag{J-1}$$

$$\begin{gathered} u_1(a_x, y, z) - u_1(0, y, z) = -a_x \nu_{31} \bar{\varepsilon}_{33} \text{ for } 0 \le y \le a_y,\ 0 \le z \le a_z \\ u_2(x, a_y, z) - u_2(x, 0, z) = -a_y \nu_{32} \bar{\varepsilon}_{33} \text{ for } 0 \le x \le a_x,\ 0 \le z \le a_z \\ u_3(x, y, a_z) - u_3(x, y, 0) = a_z \bar{\varepsilon}_{33} \text{ for } 0 \le x \le a_x,\ 0 \le y \le a_y \end{gathered} \tag{J-2}$$

$$\eta_{2\sigma c} = \frac{\frac{1}{V_c}\int \sigma_{22c}(x,y,z)dV_c}{\frac{1}{V_m+V_v}\int \sigma_{22m}(x,y,z)dV_{m+v}} \quad \text{(J-1)}$$

$$\eta_{2\sigma g} = \frac{\frac{1}{V_g}\int \sigma_{22g}(x,y,z)dV_g}{\frac{1}{V_m+V_v}\int \sigma_{22m}(x,y,z)dV_{m+v}} \quad \text{(J-2)}$$

$$\eta_{3\sigma c} = \frac{\frac{1}{V_c}\int \sigma_{33c}(x,y,z)dV_c}{\frac{1}{V_m+V_v}\int \sigma_{33m}(x,y,z)dV_{m+v}} \quad \text{(J-3)}$$

$$\eta_{3\sigma g} = \frac{\frac{1}{V_g}\int \sigma_{33g}(x,y,z)dV_g}{\frac{1}{V_m+V_v}\int \sigma_{33m}(x,y,z)dV_{m+v}} \quad \text{(J-4)}$$

where,

$\eta_{2\sigma c}, \eta_{2\sigma g}$: carbon and glass stress partitioning when uniaxial load is applied in 2-direction

$\eta_{3\sigma c}, \eta_{3\sigma g}$: carbon and glass stress partitioning when uniaxial load is applied in 3-direction

The results of the finite element analysis for the anti-symmetric and symmetric RUC of C50G50 composite are shown in Table I- 1 and Table I- 2.

Table I- 1. Stress partition parameters of C50G50 model for fibers positioning about the transverse plane.

Direction from which the SPP is computed	2-direction		3-direction	
SPP from FEA	$\eta_{2\sigma c}$	$\eta_{2\sigma g}$	$\eta_{3\sigma c}$	$\eta_{3\sigma g}$
Symmetric C50G50 RUC	1.70	1.67	1.70	1.67
Anti-symmetric C50G50 RUC	1.49	2.92	1.96	1.99

Table I- 2.Transverse elastic modulus obtained from FEA and experiment for C50G50 model

	FEA		Experimental
	E_2 (GPa)	E_3 (GPa)	E_2 (GPa)
Symmetric C50G50 RUC	15.8	15.8	17.8
Anti-symmetric C50G50 RUC	17.8	16.9	

In the anti-symmetric C50G50 RUC the SPPs do not retain the same value when the loads are applied in 2- or 3- direction. Also E_2 of the model is not equal to E_3. This is due to the antisymmetric arrangement of fibers about the transverse plane. Therefore, the symmetric C50G50 RUC was taken as the right micro-structure to model the C50G50 hybrid composite.

Appendix K

Validation of finite element approach for stress partitioning parameters

This exercise is performed to validate the boundary conditions presented for uniaxial stress $\bar{\sigma}_{22}$ such that $\bar{\varepsilon}_{22}$ in equation (14) is equal to unity. The boundary conditions are applied to the C50G50 RUC and the volume averaged stresses and displacements in 1-, 2- and 3- directions are analyzed. Since the boundary conditions in equation (14) simulate uniaxial tension of the RUC in the 2-direction, the volume averaged stresses in the 1- and 3-directions are approximately zero, within numerical error, and the volume averaged stress in the 2-direction is equal to the transverse Young's modulus of the composite (Table K- 1). The contours of 1-, 2- and 3-direction stresses are plotted in Figure K-3, Figure K-4 and Figure K-4, respectively. Although unit strain is applied to the RUC, it is enforced in an average sense. Therefore, the boundaries of the RUC are wavy (Figure K-6, Figure K-7 and Figure K-7), but overall, the RUC is periodic in nature.

The transverse elastic properties of the composite can also be obtained by averaging the field variables on the boundaries, as follows. The averaged 2-direction stress on the y = 0 and y = 36 μm surfaces of the RUC is 15.3 GPa. This value differs slightly from that obtained by volume averaging the 2-direction stress (15.6 GPa) due to numerical error. Table K- 2 lists the averaged 2-direction nodal displacements on y = 0 and y = 36 μm surfaces, the difference of these displacements (i.e., the elongation in the 2-direction), and the averaged strain in the 2-direction (i.e., the elongation divided by the 2-direction length of the RUC). Similarly, the averaged 3-direction nodal displacements, elongation, and strain are given in Table K- 3 and the averaged 1-direction nodal displacement, elongation, and strain are given in Table K- 4. Based on these boundary stresses and strains, E_2, ν_{23}, and ν_{21} are calculated and compared to the same parameters

calculated using periodicity boundary conditions (Table 2) in Table K- 5. E_2, ν_{23}, and ν_{21} values obtained from these two methods match closely.

Table K- 1. Volume averaged 2-direction normal stresses in C50G50 RUC when $\bar{\varepsilon}_{22}$ = 1.

	$\bar{\sigma}_{11}$(GPa)	$\bar{\sigma}_{22}$ (GPa)	$\bar{\sigma}_{33}$ (GPa)
C50G50	0.2	15.6	0.1

Table K- 2. Averaged 2-direction nodal displacements, elongation, and strain in the C50G50 RUC when $\bar{\varepsilon}_{22}$ = 1.

$\bar{u}_2$			
at y = 0 μm	at y = 36 μm	Elongation	$\bar{\varepsilon}_{22}$
-25.4 μm	10.0 μm	35.4 μm	0.983

Table K- 3. Averaged 3-direction nodal displacements, elongation, and strain in the C50G50 RUC when $\bar{\varepsilon}_{22}$ = 1.

$\bar{u}_3$			
at z = 0 μm	at z = 36 μm	Elongation	$\bar{\varepsilon}_{33}$
10.4 μ	-5.4 μm	-15.8 μm	-0.44

Table K- 4. Averaged 1-direction nodal displacements, elongation, and strain in the C50G50 RUC when $\bar{\varepsilon}_{22}$ = 1.

$\bar{u}_1$			
at x = 0 μm	at x = 9 μm	Elongation	$\bar{\varepsilon}_{11}$
0 μm	-0.32 μm	-0.32 μm	-0.036

Table K- 5. Comparison of transverse modulus and Poisson's ratios obtained from boundary averaging method in SPP analysis when $\bar{\varepsilon}_{22}$ = 1 and periodic boundary conditions from Table 2.

Boundary Averages			From Table 2		
E_2 (GPa)	ν_{23}	ν_{21}	E_2 (GPa)	ν_{23}	ν_{21}
15.6	0.44	0.036	15.8	0.44	0.036

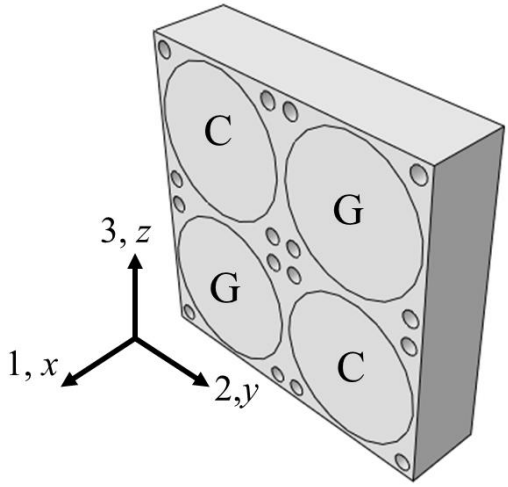

Figure K-1. RUC of C50G50 composite (C = carbon; G = Glass)

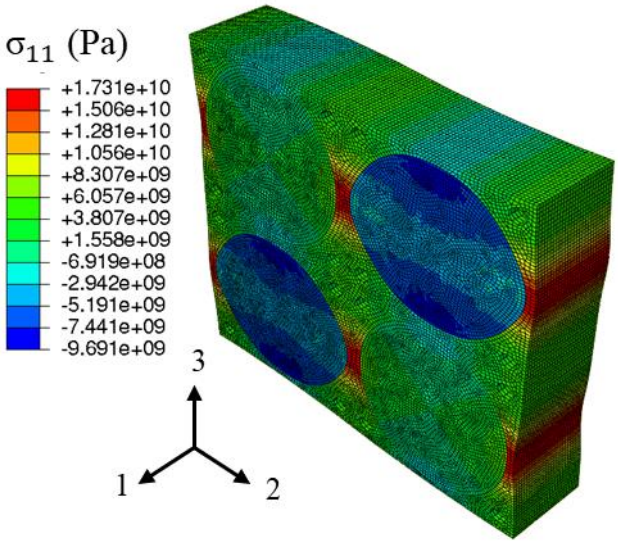

Figure K-2. Contour plot of 1-direction elemental stresses of C50G50 RUC in SPP analysis

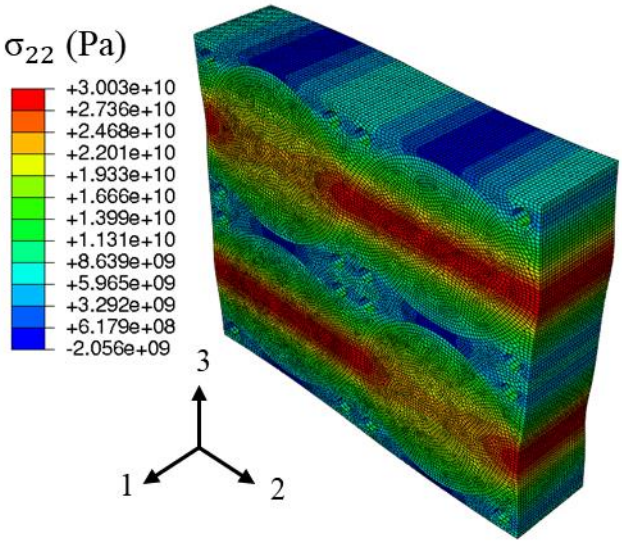

Figure K-3. Contour plot of 2-direction elemental stresses of C50G50 RUC in SPP analysis

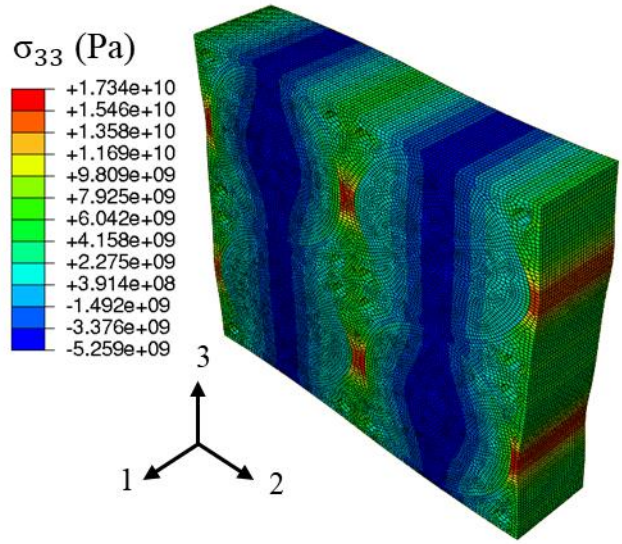

Figure K-4. Contour plot of 3-direction elemental stresses of C50G50 RUC in SPP analysis

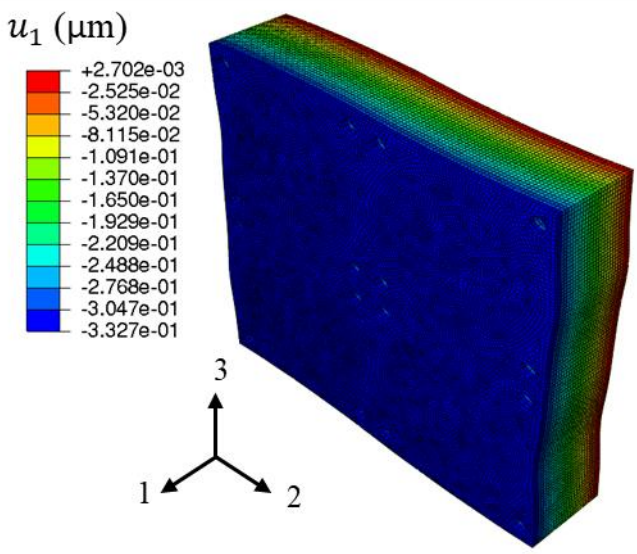

Figure K-5. Contour plot of 1-direction elemental displacements of C50G50 RUC in SPP analysis

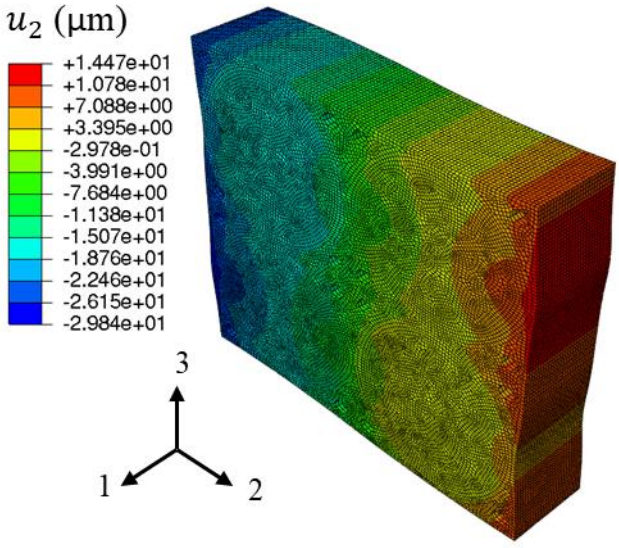

Figure K-6. Contour plot of 2-direction elemental displacements of C50G50 RUC in SPP analysis

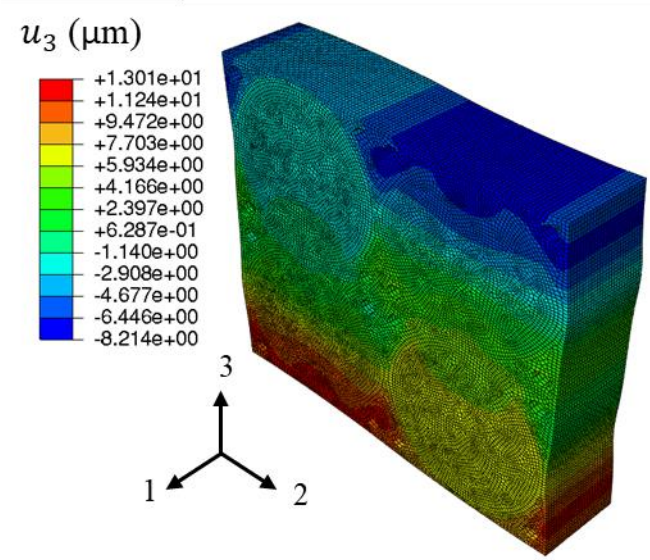

Figure K-7. Contour plot of 3-direction elemental displacements of C50G50 RUC in SPP analysis

Non-Technical Abstract

Unidirectional hybrid composites are material systems consisting of two or more fiber types, when combined have superior mechanical performance and properties than the constituents. As a consequence, hybrid composites provide cost effective design solutions. For utilizing hybrid composites in various applications, it is important to know the Young's modulus of elasticity transverse to the fibers.

Little experimental data is available on the available in literature and very few micromechanical models haven been developed and validated for the transverse Young's modulus of hybrid composites. In the current investigation finite element and closed-form models with and without empirically determined fitting parameters have been developed to simulate the transverse Young's modulus of all-carbon, all-glass and hybrid composites. Unlike other investigations, the effect of voids are included in the analysis. Also, using the finite element approach, the load sharing mechanisms among the carbon fibers, glass fibers and the matrix are evaluated. It was observed that the finite element analysis predicts the transverse Young's modulus of the hybrid composites very well. The semi-empirical models have good predictions of the transverse Young's modulus but they could not give deeper insights on the load sharing mechanisms between the fibers and matrix. Finite element models revealed that when equal proportions of glass and carbon fibers are mixed, the carbon fibers undergo larger deformation that the glass fibers due to the presence of relatively stiff glass gibers placed next to it. The stress and strain level in the matrix could be modeled as springs in parallel and series, respectively, when the glass-to-carbon ratio was increased.